Integrated Seismic and Rock Physics Modelling of Oil-Producing Volcanic Sills in the Neuquén Basin, Argentina

An approach combining data from fieldwork, wells, and seismic surveys.

Ole Rabbel

Thesis submitted for the degree of
Master of science in Geosciences: Geophysics
60 credits

Department of Geosciences
Faculty of mathematics and natural sciences

UNIVERSITY OF OSLO

Autumn 2016

Integrated Seismic and Rock Physics Modelling of Oil-Producing Volcanic Sills in the Neuquén Basin, Argentina

An approach combining data from fieldwork, wells, and seismic surveys.

Ole Rabbel

Integrated Seismic and Rock Physics Modelling of Oil-Producing Volcanic Sills in the Neuquén Basin, Argentina

http://www.duo.uio.no/

Printed: Reprosentralen, University of Oslo

Acknowledgements

I would like to seize the opportunity to thank a number of people who helped both scientifically and personally in order to build this thesis. First off, I would like to thank my supervisors Karen Mair, Olivier Galland, and Isabelle Lecomte for giving me the opportunity to be part of this fantastic project, for letting me join on an amazing field trip to Argentina in Spring 2016, and for supporting throughout my master's degree. For great company and fun times in the field, Juán and Fedé also deserve a big *gracias*. I would like to thank Kim Senger who not only provided valuable comments and practical advice, but who also invited me for a workshop and discussions on Svalbard. *Yacimientos Petrolíferos Fiscales (YPF)* are thanked for their courtesy of providing the subsurface data. The Centre for Integrated Petroleum Research (Uni CIPR) in Bergen are acknowledged for providing the LIME software. Special thanks go to my family for their support, especially to my father for being my personal rock physics advisor and Matlab-crisis manager. Apart from all the others I have not forgotten but cannot all name explicitly (for instance, the staff at the department for Physics of Geological Processes, PGP), I would like to thank Karoline who bore with me whenever I claimed that I "just need five minutes to fix this one thing" and usually ended up being at least an hour late for lunch, tea, or dinner...

Abstract

Igneous sills are commonly observed in sedimentary basins around the world and may have significant influence on the related petroleum systems. Seismic reflection data play a key role for the characterisation of sill complexes. It is often difficult to validate seismic interpretations, because few wells are drilled into intrusions. Furthermore, the comparison of outcrops to kilometre scale seismic images is challenging due to resolution issues. Most of the seismic interpretation work is focussed on mapping intrusion geometries, while quantitative seismic analysis is challenging and rarely performed. In this study, observations from geological fieldwork, 3D virtual outcrop models, core samples and well logs are integrated and linked to qualitative and quantitative seismic analysis of an oil-producing volcanic sill complex in the Neuquén Basin, Argentina. The link is established by performing integrated seismic forward modelling and rock physics modelling. The seismic modelling is based on a realistic, metre-scale geological model obtained from a virtual 3D model of a large-scale analogue outcrop. The rock physics modelling uses fracture properties obtained from fieldwork and core samples to investigate the effect of fractures on elastic properties. Results from seismic modelling show characteristic waveforms with remarkable similarity to observations from seismic field data. These waveforms arise from interference and include branching and steps of reflections. This can be used to interpret corresponding intrusion geometries. Additionally, the seismic amplitudes related to sills can be much more variable than usually assumed. Rock physics modelling suggests that this variability may be partly explained by the effect of fractures on the seismic velocities of the sills. Fracture analysis from outcrop data indicates the presence of several fracture sets of preferred orientations. The corresponding rock physics modelling predicts a marked drop in P-wave velocity as well as P-wave anisotropy of up to 14%. However, with rising complexity of the fracture pattern, the incident angles that are required to recover this anisotropy from azimuthal seismic field data increase from $> 30°$ to $> 60°$. In fact, such azimuthal anomalies in sills have been observed in real seismic data from the oil fields. The approach presented in this study illustrates how various geoscientific datasets can be linked and thereby used to increase the reliability of qualitative and quantitative seismic interpretations of volcanic sill complexes.

Contents

List of Figures

List of Tables

1 Introduction

1.1 General Introduction

In recent years, research has provided evidence for the presence of large volumes of igneous intrusions in numerous sedimentary basins around the world. In particular, three-dimensional (3D) seismic reflection data have been playing a key role in the imaging, mapping and analysis of these intrusions in the subsurface (Magee et al., 2015). The interest in the characterisation of subvolcanic igneous plumbing systems is mainly twofold. Research on volcanology and geodynamics is directed towards the characterisation of plumbing systems and the mapping of the extent, structure and geometry of intrusions in order to relate them to emplacement processes (Polteau et al., 2008; Schofield et al., 2012; Schofield et al., 2015; Eide et al., 2016). On the commercial side, intrusions such as volcanic sills and laccoliths may have a strong impact on basin dynamics and the related petroleum systems, as well as on hydrocarbon exploration (Planke et al., 2005). Four main effects of intrusives on petroleum systems have been identified. (1) Source rocks can be locally matured due to heat provided by magma intruding into organic rich sediments (Rodriguez Monreal et al., 2009). (2) The host rock can be deformed or uplifted, causing e.g. overlying strata to form "forced folds" or domes which may represent hydrocarbon traps (Polteau et al., 2008; Magee et al., 2014). (3) Migration conduits as well as reservoirs for hydrocarbons may form as a result of intensive fracturing caused by cooling effects and/or tectonic stresses (Polteau et al., 2008; Farooqui et al., 2009; Rodriguez Monreal et al., 2009; Witte et al., 2012). (4) Intrusions may form barriers for fluid flow due to low permeability and thereby they potentially inhibit fluid migration and extraction (Schofield et al., 2015).

Seismic data are often the primary source for the mapping and characterisation of large-scale intrusive complexes. A variety of problems is related to seismic imaging of the intrusions. With respect to a typical seismic wavelength, sills often represent thin geological layers of high seismic velocity (Planke et al., 2014). If they are thick enough to be resolved in seismic data, they represent prominent high amplitude reflectors which

are easy to map (Planke et al., 2014). Importantly, recent studies indicate that many sills are too thin to be recognised in seismic images and that up to 88% of sills could be missing in the interpretation (Schofield et al., 2015). Intrusives are usually considered to create high risk for hydrocarbon exploration and, therefore, they are rarely drilled (Planke et al., 2005; Magee et al., 2015). The lack of wells makes the validation of observations from seismics difficult, such that field analogues are commonly used to argue for seismic interpretation. On the other hand, direct field analogues are not always available, especially when interpreters are dealing with offshore data. Seismic modelling can be helpful to develop a better understanding of the expected seismic response of intrusions. However, only few seismic modelling studies of volcanic sill complexes have been published, mostly focussing on one-dimensional simulations of idealised intrusion shapes (e.g. Rohrman, 2007; Magee et al., 2015). Additionally, volcanic sills comprise generally high, but nevertheless quite variable seismic velocities (Skogly, 1998). The controlling mechanisms are rarely investigated and therefore poorly understood (Farooqui et al., 2009). In the rare cases where volcanic sills act as commercial hydrocarbon reservoirs, the understanding of the petroleum system is very limited, and more systematic studies are required (Farooqui et al., 2009; Witte et al., 2012).

Objectives and Thesis Outline

This study investigates the potential of seismic characterisation of fractured hydrocarbon producing sills in the northern Neuquén Basin, Argentina. Companies exploiting these atypical reservoirs report that seismic imaging of those sills is challenging. Many of the sills have thicknesses below the limit of seismic resolution and rock properties within the intrusions vary significantly (*Yacimientos Petrolíferos Fiscales (YPF)*, pers. comm.). Fractures are assumed to be critical for the generation of permeability and porosity in the reservoirs, but large uncertainties are connected to the identification of the controlling mechanisms and the detection of productive zones (Witte et al., 2012). However, opposed to most studies of other volcanic sill complexes, the available dataset for these intrusions includes numerous wells, cores, high quality analogue outcrops, as well as 3D seismic data. The access to such a comprehensive pool of data is extremely rare and provides a unique opportunity for integrated studies of volcanic sill complexes in general, and volcanic reservoirs in particular. Following this motivation, the aim of this study is to improve the seismic characterisation of the oil-producing volcanic sill complex by creating a link to geological observations. High-resolution 3D models of an outcropping volcanic sill complex play a key role to establish this link. Three main objectives are defined below alongside the respective scientific approach.

1. *Assessment of the expression of realistic intrusion geometries in seismic data to reduce interpretation risk.*
   An advanced 2D/3D convolution technique is employed to perform seismic forward modelling. Realistic geometries are used, which are obtained from 3D mapping of a large-scale outcrop of a volcanic sill complex. The objective is to assess the influence of signal frequency, illumination, and elastic properties on the imaging result. In addition, the modelled seismic sections are used to link detailed, but large-scale outcrop observations to a 3D seismic survey in a nearby oil field. The model properties are well constrained by a set of well logs.

2. *Investigation of the effects of fractures on elastic properties and their quantitative assessment using seismic methods.*
   The second objective includes the conduction of rock physics modelling in order to improve reservoir characterisation on the subseismic scale. The focus of this part of the study is the influence of fractures and other potential elements of the pore space on the elastic properties of the rocks. Particular attention is given to elastic anisotropy effects. The fracture network is constrained by combining fieldwork, high resolution virtual outcrops, core and well data.

3. *Integration of seismic and rock physics modelling.*
   An integrated analysis of the seismic modelling and rock physics modelling studies is performed. The modelling results are compared to datasets from the oil field, including well logs, 3D seismic sections and seismic attribute analysis for fracture detection. By integrating the various sets of data, the study seeks to improve the seismic characterisation of the volcanic sill reservoirs. The work also includes an outline of the potential and pitfalls that may be connected to this type of integrated approach.

A wide variety of techniques from different geoscientific fields is applied in this study, and their relation may not always be obvious on first sight. In order to avoid confusion, a brief thesis outline will be given here, and further guidance is provided throughout the thesis. The work starts with an outline of the geological setting in order to locate the study and create awareness of the most important geological features. Chapter 2 introduces the necessary theoretical background for the different measurement and modelling techniques that are used in this work. After presenting the fieldwork and subsurface datasets that were used for this work (chapter 3), the implementation of the previously introduced methods is explained in chapter 4. The implementation of the methods is divided into two workflows (termed A and B) which correspond to the

work that was done to accomplish the seismic modelling and rock physics modelling, respectively. Thereafter, the presentation of the results of these workflows follows in the same order, i.e. the results from seismic modelling and rock physics modelling are shown separately. Finally, the discussion addresses the research goals and related approaches, including (1) seismic modelling, (2) rock physics modelling, (3) integration of modelling and other datasets.

1.2 Geological Setting

The study area is located in the Rio Grande Valley, approximately 70 km south of the city Malargüe. The Rio Grande Valley lies in the northern part of the Neuquén Basin in western Argentina (figure 1.1). A large number of geoscientific studies has been conducted in the Neuquén Basin, because it comprises the most important hydrocarbon province in Argentina (Sruoga and Rubinstein, 2007).

The geodynamic evolution of the Neuquén Basin comprises three main phases. It initially formed as an elongated rift system in the Permian-Triassic period as a consequence of the collapse of the Gondwana orogen (Howell et al., 2005). After the onset of Andean subduction, the Neuquén Basin transformed into a backarc-basin and experienced a phase of regional thermal subsidence (Howell et al., 2005). From the Cretaceous and onwards, the tectonic regime shifted to compression, causing inversion of the Mesozoic rifts and the formation of several N-S oriented fold-thrust belts (Manceda and Figueroa, 1995; Howell et al., 2005). This stage of the evolution of the Neuquén Basin is referred to as its foreland basin stage (Howell et al., 2005).

The sedimentary succession is nearly continuous from upper Triassic to lower Cenozoic rocks (figure 1.2). This has made the area a famous field site, for instance for basin evolution and reservoir analogue studies (e.g. Leanza, 2009; Balgord and Carrapa, 2016). While the triassic rifts initially represented isolated depositional centres, an up to 4000 m thick succession was deposited in a marine environment in Jurassic to Cretaceous times (Howell et al., 2005). This including the organic rich shales of the Vaca Muerta and Agrio formations, which represent the main source rock of the hydrocarbon discoveries which have been made in the Neuquén Basin (Badessich et al., 2016). The overlying Cenozoic sediments are dominated by continental deposits (Balgord and Carrapa, 2016). The compressional tectonics during the Cenozoic were accompanied by repeated periods of extensive volcanism and widespread intrusion of magma into the sedimentary rocks

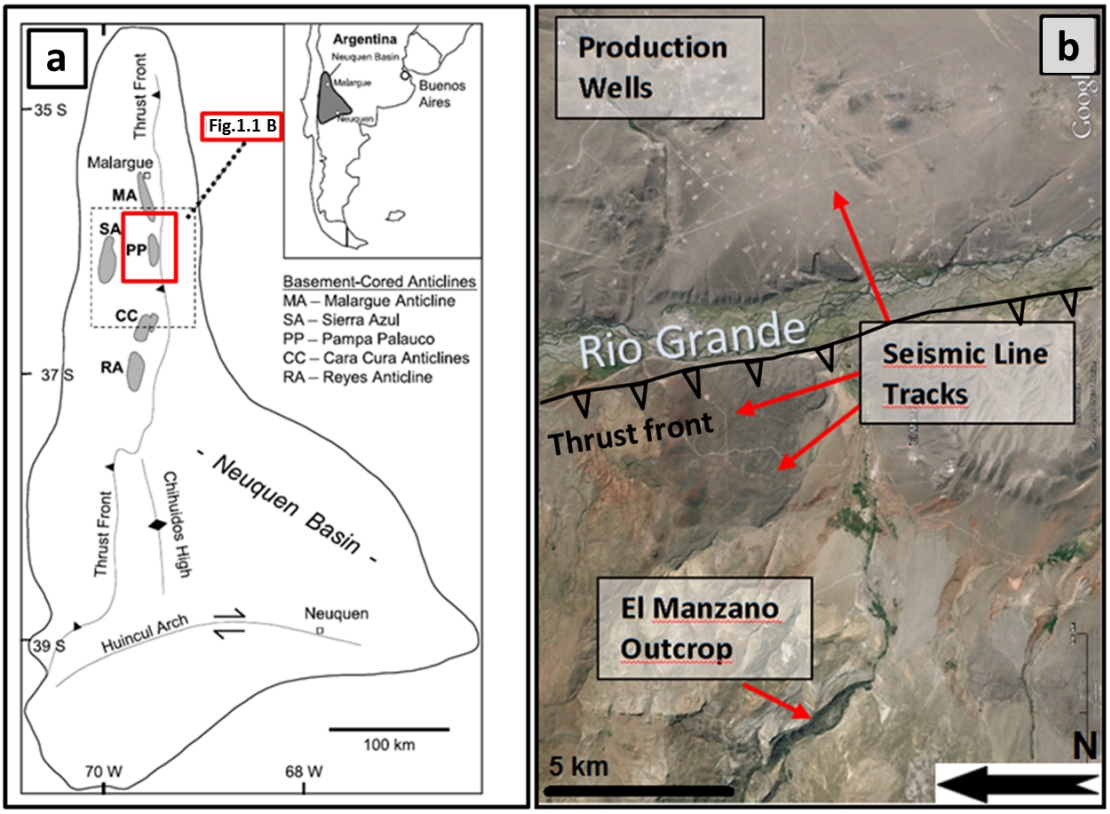

Figure 1.1: (a) Map of Neuquén Basin and the location of the study area (red box). Edited from Witte et al. (2012) (b) Close-up Google Earth satellite image showing El Manzano and the adjacent oil field, including wells (bright spots) and seismic line tracks (thin white lines).

throughout the basin(Kay et al., 2006). These intrusions are commonly intensly fractured and comprise a number of atypical hydrocarbon reservoirs Sruoga and Rubinstein, 2007; Rodriguez Monreal et al., 2009; Witte et al., 2012. Although such volcanic reservoirs are not uncommon and have attracted increased scientific interest in recent years, systematic studies are still lacking (Rohrman, 2007; Farooqui et al., 2009; Witte et al., 2012). In the Rio Grande Valley, the Los Cavaos oil field produces from andesitic sills of Miocene age that have intruded the Vaca Muerta and Agrio formations Witte et al. (2012). The field site called El Manzano is located 10 km west of Los Cavaos. It is situated almost directly at the thrust front of the Malargüe fold-thrust belt (figures 1.1, 1.2b). Here, an extensive volcanic sill complex within the Vaca Muerta shale has been uplifted by a major thrust. The sills are well exposed and easily accessible. The outcrop may serve as a reservoir analogue for hydrocarbon-bearing sills of the Rio Grande Valley.

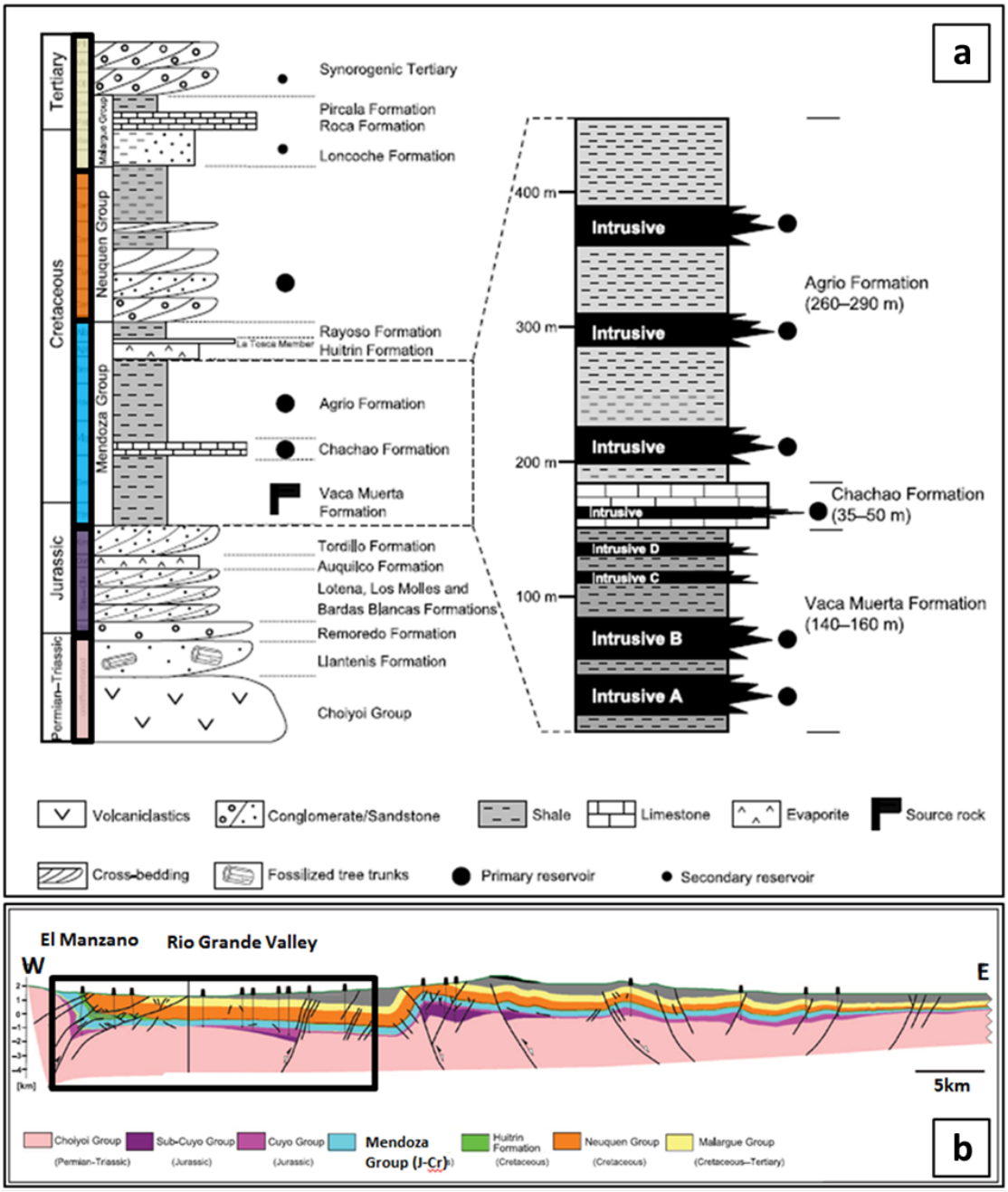

Figure 1.2: (a) Stratigraphic column of the Neuquén Basin, indicating the regional source rocks, reservoir levels and intrusion positions. (b) E-W oriented schematic section through the northern Neuquén Basin and the study area, with the Malargüe fold-thrust-belt in the west. Edited from Witte et al. (2012)

2 Theoretical Background

In this chapter, the theoretical background of the techniques that were applied in this work is provided. This includes a 3D mapping technique termed Structure from Motion (section 2.1) which was used to acquire data for the creation of photo-realistic virtual outcrop models. These models provide an important part of the information needed for seismic forward modelling (section 2.2) and fracture network characterisation (section 2.3). Finally, some of the theory behind the rock physics modelling performed in this study is introduced in section 2.4, with a special focus directed towards the effects of fractures on elastic rock properties. Note that this chapter is providing the *theoretical background*, while the *implementation* of the methods and the related workflows are described in chapter 4.

2.1 Structure from Motion

In the following section, the Structure from Motion (SfM) technique will be introduced which was used to create high resolution 3D models of an outcropping volcanic sill complex. SfM belongs to the methods of photogrammetry that are used to map 3D surfaces based on a series of overlapping images. Traditional photogrammetric methods require knowledge of the exact location and orientation of the camera or accurately measured ground control points in order to reconstruct the target surface. In contrast, SfM only requires multiple (>2) images with sufficient overlap and offset which are acquired while moving along or around the target (Westoby et al., 2012). Fig. 2.1 illustrates the acquisition principle. Further images displaying the data acquisition for SfM are shown in the description workflows (section 4). SfM algorithms automatically calculate the camera positions during acquisition by identifying corresponding features (keypoints) between individual images (Westoby et al., 2012). The initially computed camera positions are used to extract a low-density point cloud of the target which are iteratively optimised to create the final high resolution point cloud model (Saunders, 2014). The main factors determining the quality of the output model are image sharpness, resolution, survey density and surface texture, as they control the number of identifiable

keypoints in each scene (Westoby et al., 2012). The resulting point cloud will neither be scaled nor oriented correctly. However, scaling and georeferencing can be achieved through the implementation a set of ground control points with known GPS coordinates. Because the SfM process itself does not depend on control points, the user may decide on the level of georeferencing accuracy according to their own demands. After this step, the point cloud can be used to create surface models such as digital elevation models (DEM) or triangular meshes which serve as the foundation of geological analysis and interpretation (Westoby et al., 2012). Both open source and commercial software are available for SfM processing, the package used in this work was Agisoft Photoscan. A description of the input dataset and processing parameters chosen for different parts of this work will be given in sections 4.1 and 4.2.

Outcrop models using meshes in combination with a photo-realistic texture draped over the surface are often referred to as Virtual Outcrop Model (VOM, e.g. Enge et al., 2007). Models obtained from SfM can vary immensely in scale and resolution, depending on purpose and survey setup. This makes the technique well suited to produce DEMs and VOMs for a variety of purposes. Such models have recently been used to provide detailed outcrop-based geometries of geological surfaces or bodies to produce geocellular models (Enge et al., 2007) that are suitable for simulations such as fluid flow or seismic modelling. If sufficiently high surface resolution can be achieved, SfM based models may also be utilised to measure fracture planes to characterise fracture networks (Casini et al., 2016). Both applications are used in this work and will be introduced in the next sections.

2.2 Seismic Modelling

With the help of seismic modelling it is possible to predict or approximate the subsurface propagation of elastic waves. It is essential to understand the seismic response of an Earth model, for instance comprising a volcanic sill complex, and produce synthetic seismograms to be used in seismic processing or to aid geological interpretation of real seismic data (Lecomte et al., 2015). The main elements needed to perform seismic modelling are a knowledge of (1) the seismic input signal, (2) the velocity model, (3) the survey parameters, and (4) seismic reflection coefficients based on elastic property variations in the model (including P-wave velocity, S-wave velocity and density). With these four elements, wave propagation through the subsurface as well as the behaviour at surfaces with seismic property contrasts can be predicted.

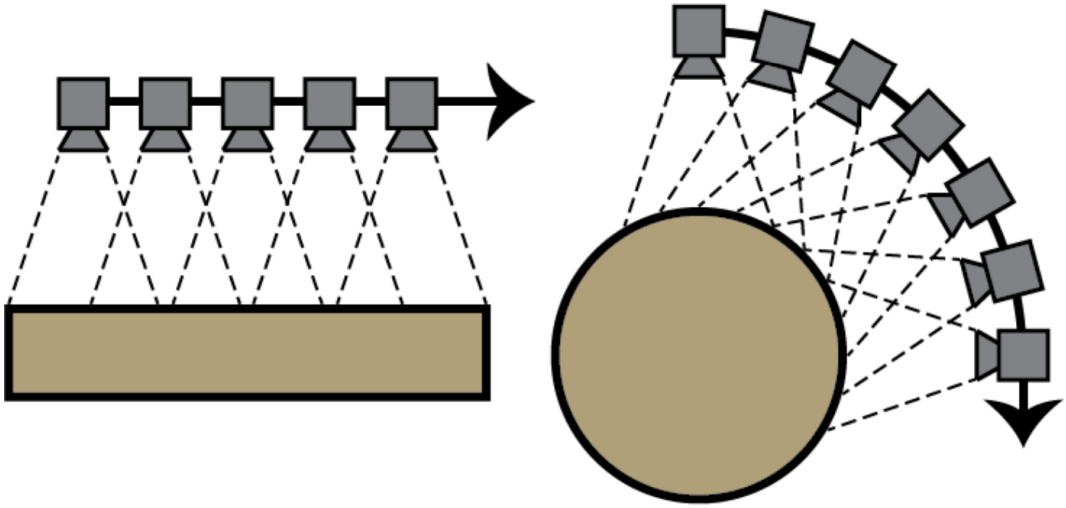

Figure 2.1: Acquisition principle of the Structure from Motion method. As the method's name indicates, the camera is moved along or around a target, and a dense set of overlapping images is acquired. This set of images is then used to reconstruct the 3D surface of the target. From Saunders (2014).

There are several approaches to seismic modelling, each having their individual strengths and weaknesses, as summarised by Lecomte et al. (2015): Full wavefield (FW) methods provide seismograms containing all wave types and are thus the ideal solution, but have high cost in both time and resources. Methods based on ray-theory may serve as an appropriate alternative, but require smooth changes in the velocity field between reflectors to be valid, posing problems when significant small-scale variations are present in the Earth model. 1D convolution therefore constitutes a time and resource efficient solution for many interpreters by simply convolving an input wavelet with a 1D model of the Earth's reflectivity. However, the validity of this approach is very restricted, requiring, for instance, horizontal layers, zero-offset sections and no lateral velocity variations.

Therefore, Lecomte et al. (2003) proposed a 2D/3D convolution method to simulate pre-stack depth migrated (PSDM) sections. PSDM images are a desirable end result of seismic processing and they can be understood as a filtered version of the true Earth reflectivity model (Lecomte, 2008). The method is independent from seismogram data (observed or synthetic) and uses a filter function in the wavenumber domain to perform the convolution and generate the synthetic migrated seismic sections. Thereby, one

avoids going through a costly forward-modelling and processing sequence (Lecomte et al., 2003). This "PSDM filter" is called point-spread function (PSF) in the space domain, and represents the impulse response of a point scatterer under given conditions. The PSF varies spatially and takes into account input wavelet and angle-dependent resolution illumination due to the overburden and survey parameters (Lecomte, 2008). It is of major importance to recognise the 2D/3D nature of the PSF, because this provides a tool for a comprehensive understanding of spatial resolution, superior to the classic 1/4 and 1/2-wavelength rules of thumb for vertical and lateral resolution, respectively. Additionally, in the case of a complex overburden, the terms "vertical" and "lateral" may not be ideal to describe the imaging conditions. In other words, the size and shape of the PSDM filter and the corresponding PSF tells us what will or will not be resolved and illuminated. Figure 2.2 illustrates the elements of the filter process which is only briefly reviewed here (see Lecomte (2008) for more details). First (figure 2.2a), the so-called illumination vector $\mathbf{I}_{SR}$ is determined by employing ray-tracing to calculate the incident and scattered wavefield in the overburden model for a single point scatterer and a single source-receiver pair:

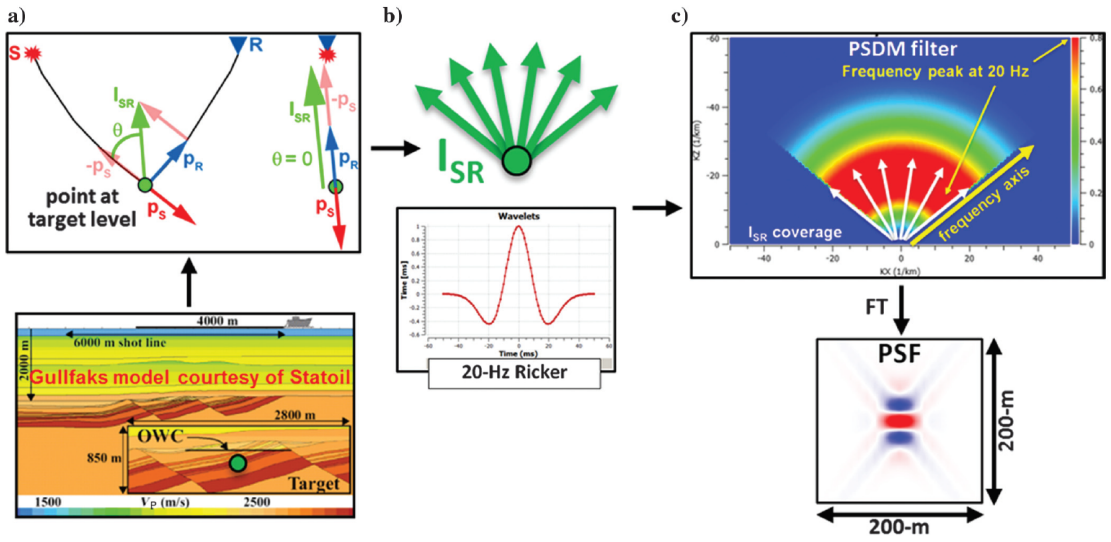

Figure 2.2: Principle of the 2D/3D convolution technique used for seismic modelling in this work. The background (overburden) model and survey parameters are used to calculate illumination vector I_{SR} for the taget model (a). This is combined with other paramters, such as the wavelet (b), to obtain the PSDM filter (c), which is finally convolved with the given Earth model to simulate a seismogram. Figure from Lecomte et al. (2015).

$$\mathbf{I}_{SR} = \mathbf{p}_R - \mathbf{p}_S \tag{2.1}$$

In equation 2.1 $\mathbf{p}_R$ and $\mathbf{p}_S$ represent the slowness vectors of the incident and scattered wavefield, respectively. The next step is to obtain the scattering wavenumber k_{SR} by multiplying the illumination vector by the frequency f of the input wavelet:

$$\mathbf{k}_{SR} = \mathbf{I}_{SR} f \tag{2.2}$$

$\mathbf{k}_{SR}$ yields information on the resolution, because it gives a local plane wavefront which is tangential to the scattering isochrone. This, in turn, defines all possible positions of a point scatterer for a seismic event recorded with a single source-receiver pair (the reader is referred to figures 6 and 8 in Lecomte et al. (2015) for an in-depth explanation). Superimposing all scattering isochrones for all source-receiver pairs in the case of a single scatterer will then lead to constructive interference at the scatterer's location and destructive interference elsewhere. Thereby, the best possible image of the point for the given survey geometry is obtained. This yields the PSDM filter function (Fourier Transform of the PSF) composed by scattering wavenumbers, and it also resembles what happens in optimal PSDM processing. By imagining continuous reflectors as a dense set of point scatterers, the method can be applied to a geological model, and synthesise a PSDM image. Note that for cases where an overburden model is not available, it is also possible to synthesise PSFs to investigate parameter sensitivity (Lecomte et al., 2016).

Several authors have successfully demonstrated applications of this method. Previous work includes seismic modelling based on numerical fault modelling (Botter, 2016) and virtual outcrop analogue studies for comparison of seismic sections in the Barents Sea (Anell et al., 2016). In fact, the work presented here follows a similar approach to the study of Anell et al. (2016) in a different geological setting. These studies also show the technique's usefulness for sensitivity studies to assess illumination and resolution issues. In addition, they demonstrate its superiority to 1D modelling, as illustrated by figure 2.3. Especially in complex Earth models like the one shown in figure 2.3a, 1D convolution ignores limited reflector dip illumination and lateral resolution (figure 2.3b). 2D/3D convolution implements such factors and produces a seismic image which resembles a seismic section that could be obtained from surveying the underlying Earth model with perfect dip illumination (figure 2.3c) or with more realistic, limited dip illumination (figure 2.3d).

Based on geometries obtained from SfM-based outcrop models, the PSDM-based filter is used in this study to investigate the expected appearance of PSDM seismic images

of a volcanic sill complex. Exact, but time efficient seismic modelling was desired due to potentially strong interference of thin volcanic sills as well as a complex overburden within a fold-thrust belt. However, the challenge in this investigation was not only to obtain realistic seismic images, but also to link seismic wave propagation to sub-seismic scale properties such as fractures. This will be addressed in the following sections.

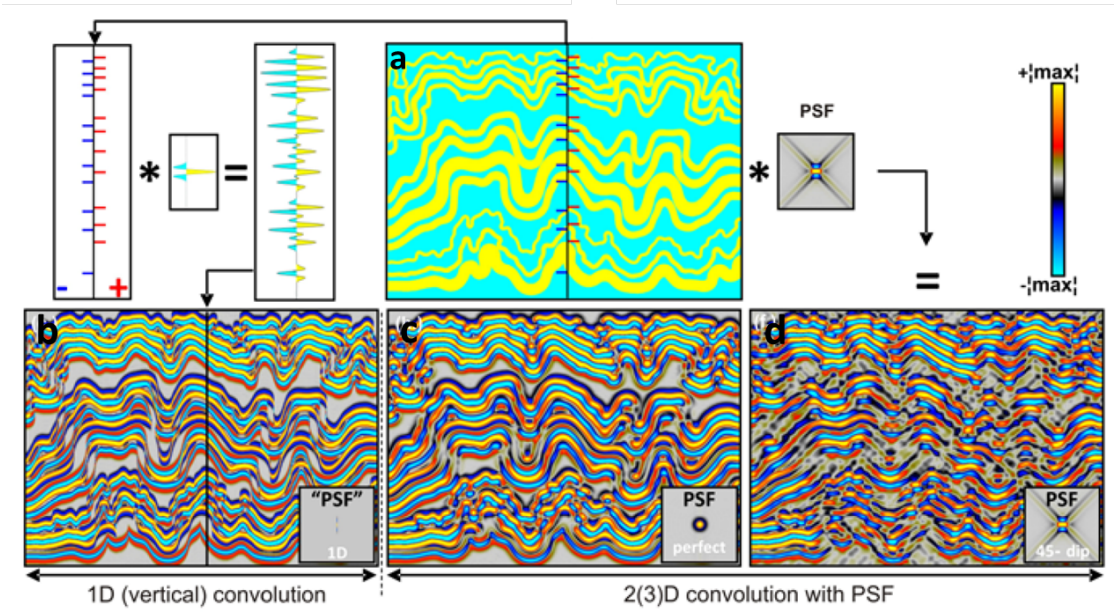

Figure 2.3: (a)Illustration of synthetic seismic sections for a complex, heavily folded Earth model. (b) is obtained by simplistic 1D-time convolution of the source pulse with the vertical Earth reflectivity series (red and blue bars). (c) Image obtained from the approach based on the point-spread function, assuming perfect illumination of reflectors at all dip angles. (d) Image obtained from a more realistic point-spread function with maximum reflector dip illumination of 45°. Figure edited from Anell et al. (2016).

2.3 Fracture Network Characterisation

Fractures are assumed to provide highly effective pathways for hydrocarbons in the sill reservoirs in Rio Grande Valley, as well as significant porosity. Therefore, a good understanding and description of the fracture network within the intrusives is a crucial part of reservoir characterisation and exploration. Fracture modelling is a popular way of characterising the fracture network that is commonly used to assess permability and porosity associated with the fratures. However, its main purpose in the context of in this study is to obtain parameters needed for elastic rock physics modelling.

For the purpose of fracture modelling, one number of parameters are required that characterise the fracture network with respect to fracture abundance, shape and orientation. Important parameters to define a set of cracks include (1) fracture orientation, e.g. in form of azimuth/dip average or distribution, (2) fracture dimensions, including length and aperture, and (3) a measure of fracture abundance (see e.g. Senger et al., 2013). While orientation, aperture and length are easily obtained, or at least constrained, from field, core or well image-log measurements, measuring fracture abundance is a more complicated matter. In part, this is because it is expressed in many different ways throughout scientific literature and consequently, fracture abundance is by no means an unambiguous quantity regarding its unit, terminology or method of acquisition (Zeeb et al., 2013). However, the discussion will be limited here to a brief introduction to one-dimensional fracture frequency (termed P10, fractures per length) and fracture density (termed P32, fracture area per volume), as these are used in common fracture modelling modules of commercial geomodelling software packages. For a deeper look into different ways of quantifying fracture abundance, the reader is referred to the excellent review of Zeeb et al. (2013). The first step to derive P32 is a measurement of the one-dimensional fracture spacing S_f along a so-called scanline. S_f is then inverted to give the corresponding P10. A correction factor C_{P3} is then applied to the P10 value based on (1) the angle between scanline and fracture plane pole and (2) the Fisher K-factor of the orientation distribution within each set. The result is the P32 value for fracture density. Figure 2.4 illustrates the relationship between scanline field measurements and resulting P32 which is calculated using equation 2.3 (Senger et al., 2013). Keep in mind that none of the geological measures for fracture abundance must be confused with the seismic crack density introduced in section 2.4 below.

$$P_{32} = \frac{C_{P3}}{S_f} \tag{2.3}$$

Fracture set orientation and sizes are subsequently combined with P32 values to establish a Discrete Fracture Network (DFN). The input parameters are used to stochastically create fractures in a geomodel which are commonly represented by planes. Not all of these planes are necessarily modelled as discrete objects. Depending on the fracture size distribution, there may be tens of millions of individual fractures incorporated to create the area defined by P32. To facilitate calculation, fractures below a certain size limit can be implemented implicitly. In this case, however, there is no defined number of total fractures in the DFN other than those modelled explicitly. This should be kept in mind, since the total number of fractures appears as an important parameter in equation 2.4.

In the context of this study, the principles introduced in this section were used to characterise the fracture network of volcanic sill reservoirs in the Rio Grande Valley. Manual and VOM-based scanline measurements are obtained during fieldwork and based on VOMs and provide the input parameters for subsequent DFN fracture modelling. The DFN results, in turn, serve as input to rock physics models (see section 2.5) which are utilised to estimate fracture effects on elastic rock properties.

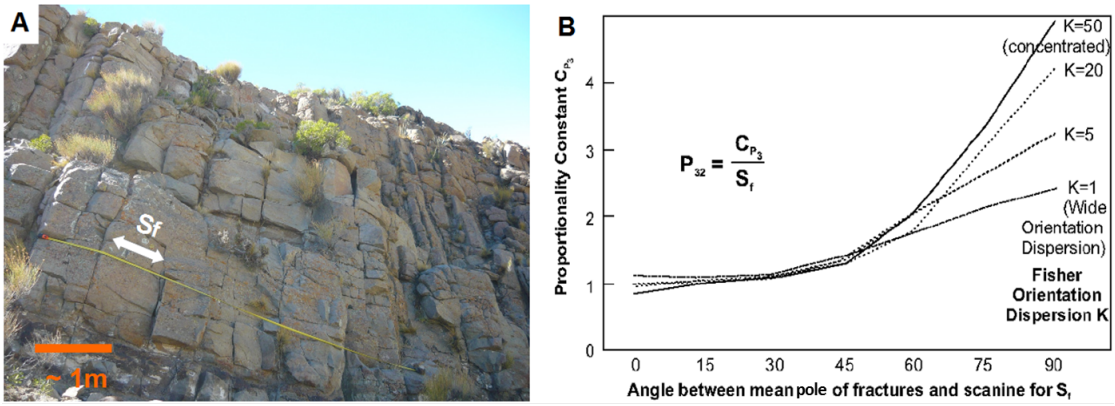

Figure 2.4: (a) Field example of a scanline (highlighted by yellow measuring tape) with fracture spacing S_f indicated. (b) Values of the correction factor C_{P3} for different angles between scanline and pole of fracture plane and Fisher K values. Figure 1b taken from Senger et al. (2013).

2.4 Rock Physics Modelling

One of the goals of seismic exploration is to relate the measured seismic response to the petrophysical properties of the subsurface geology. This link is established by rock physics models, which address the relationship between measurements of elastic parameters made from surface, well, and lab equipment; and intrinsic properties of rocks, such as mineralogy, porosity, and pore shapes, pore fluids, pore pressures, permeability, viscosity, stresses, and overall architecture such as laminations and fractures (Sayers and Chopra, 2009). Rock physics principles can not only provide tools for quantitative rock characterisation based on existing seismic data, but also estimate the effective elastic parameters for rocks with known petrophysical parameters.

Common rock physics schemes have been developed and applied for clastic rocks (Mavko et al. (2009) and references therein; Landrø (2010)) that have a fundamentally different internal structure compared to the volcanic rocks studied here. Igneous rocks are a vari-

able and challenging rock type, and to the author's knowledge, there exists no established rock physics model for volcanic sill reservoirs. Volcanics not only tend to have a variable mineralogy, but often also possess very complex pore structures originating from primary and secondary processes, including vesicles, vugs and fractures (Sruoga and Rubinstein, 2007; Farooqui et al., 2009). In order to take such features into account, the rock physics approach presented below draws an analogy to an existing rock physics model developed for carbonate rocks (Xu and Payne, 2009). The reason is that carbonate rocks often comprise a similar degree of complexity, especially with respect to pore space geometry (Farooqui et al., 2009). Figure 2.5 illustrates the modelling process and shows examples of various pore types observed in volcanic reservoirs in the Neuquén Basin at different scales.

Special attention was given to the influence of fractures on the overall elastic properties, since fractures are believed to be the main source of porosity and permeability in the volcanic reservoirs in the Rio Grande Valley (Witte et al., 2012). The effect of fracturing on the elastic properties of rocks has been a hot topic of theoretical rock physics considerations. Important contributions were made by Eshelby (1957) who approached the problem by investigating the effect of individual ellipsoidal (often "penny shaped") inclusions, and Budiansky and O'connell (1976) who introduced the seismic crack density parameter:

$$e = \frac{N\langle a\rangle^3}{V} = \frac{3\phi_f}{4\pi\alpha}, \tag{2.4}$$

In equation 2.4 N is the number of crack of average radius a in a reference volume V, and ϕ_f is the associated fracture porosity of the same fracture population if the fracture is penny-shaped with the aspect ratio $\alpha \ll 1$. Although the seismic crack density has become an important parameter in the characterisation of fractured reservoirs, it is a rather ambiguous parameter. An eximanation of equation 2.4 reveals that few, large joints and a large number of small (micro-)fractures can lead to the same crack density. Barton (2007) gives an interesting critique and provides useful thought experiments to get a better idea of how to interpret this parameter.

One can, for simplicity, assume random orientation and model the effect of fractures as isotropic. However, fractures often show preferred orientations, for instance due to the direction of tectonic stresses. As a consequence they cause anisotropy in many of their petrophysical properties, including elastic moduli. This effect is detectable using seismic reflection surveying and has been found to be critical to characterise fractured hydrocarbon reservoirs (e.g. Lynn, 2004; Far et al., 2013). The two commonly used

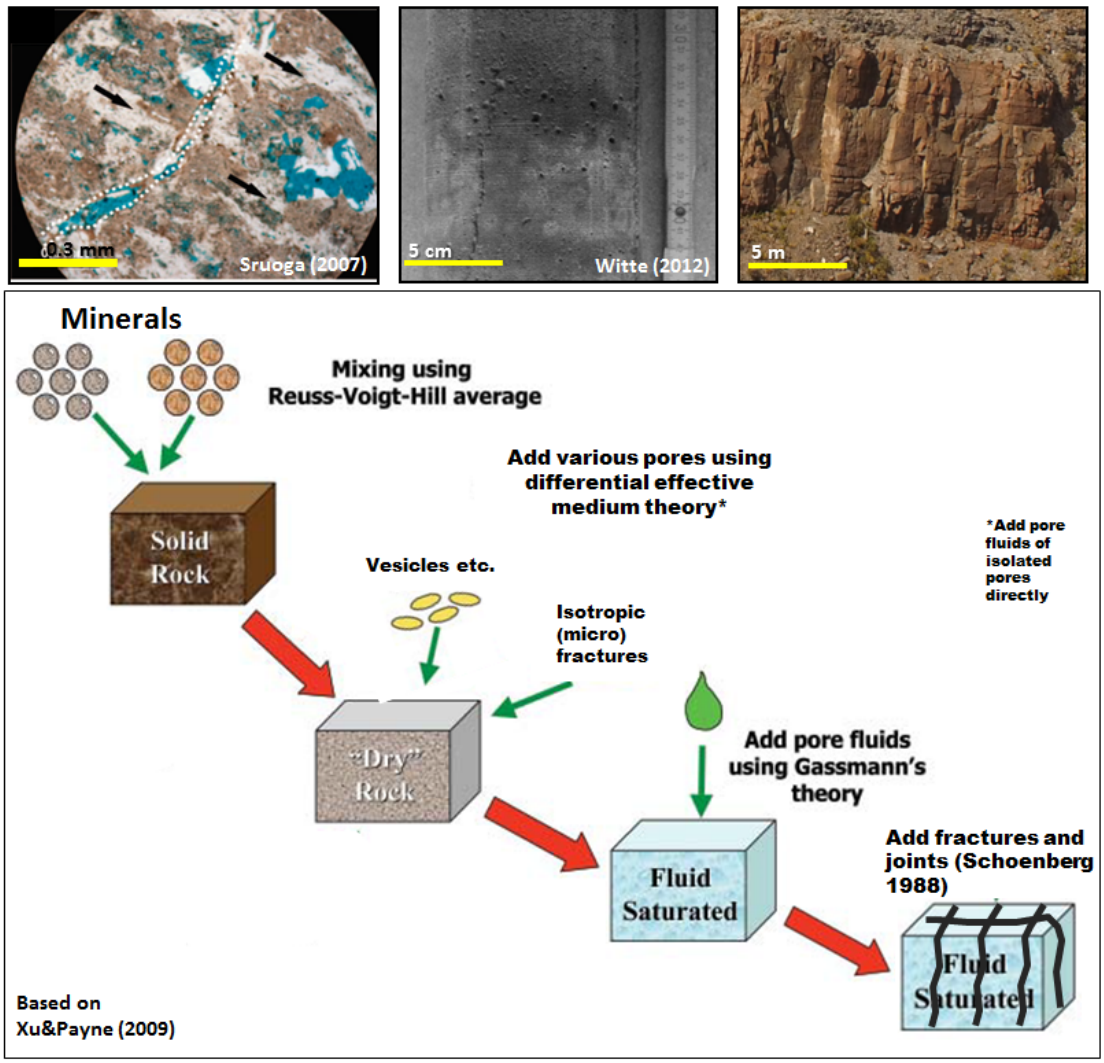

Figure 2.5: Diagram of the multi-stage rock physics model for volcanic sill reservoirs applied in this work. Photographs above the sketch show examples of pore space features which may be found in volcanic reservoirs such as microcracks, vugs, and large joints. Edited from Xu and Payne (2009).

models to explain crack-induced elastic anisotropy are described by Hudson (1980) and Schoenberg and Douma (1988) who both predict transverse anisotropy with a horizontal symmetry axis (HTI) for a single set of aligned fractures. Hudson (1980) follows the approach of ellipsoidal inclusions and based his model on perfectly aligned circular cracks in a solid. Schoenberg and Douma (1988) presents a calculation method termed termed linear slip theory, where fractures are represented as long, very thin joints that represent displacement discontinuities. Although a comprehensive review of these methods is be-

yond the scope of this work, it a brief description is necessary to note that the approaches as such are fundamentally different. Elastic moduli are defined via Hooke's law (indices dropped)

$$\sigma = \mathbf{C}\varepsilon = \mathbf{S}^{-1}\varepsilon, \tag{2.5}$$

where $\mathbf{C}$ and $\mathbf{S}$ represent the 4th order elastic stiffness and compliance tensors, respectively. σ and ε are the 2nd order stress and strain tensors, repsectively. Schoenberg and Douma (1988) accommodate the effect of fractures in so-called tangential and normal fracture compliances E_t and E_n, which result in excess compliances which are *added to the original compliance tensor* $\mathbf{S}$ in eq. 2.5. In contrast, Hudson (1980) relates the effective elastic stiffness to seismic crack density and the crack geometry, and calculates correction terms that are *substracted from original stiffness tensor*. However, Schoenberg and Douma (1988) showed that within the limits of a dilute concentration of cracks (typically $e \leq 0.05$), the theories are equivalent and E_t and E_n can be calculated given Hudson's crack specifications. In contrast, note that it is not possible to obtain unambiguous fracture geometries from fracture compliances - highlighting the necessity of other ways of fracture characterisation. By means of numerical modelling, Grechka and Kachanov (2006) pointed out that Schoenberg's linear slip theory is superior in predicting elastic stiffness of fractured media which contain high crack densities and intersecting cracks.

It is important to point out the consequences of the characteristics of the two theories on the approach that was chosen for this study. It is possible to obtain estimates of the seismic crack density, but *not* unambiguous fracture shapes from seismic data. However, given seismic crack density and fracture shape, one can calculate the effect on elastic rock properties. This makes the theory of Hudson (1980) better suited to create a link to geological observations. On the other hand, linear slip theory (Schoenberg and Douma, 1988) yields superior results, but does originally not include any information of fracture geometry. However, it is possible to obtain the parameters to apply linear slip theory from Hudson's crack specifications (but not vice versa). Because of this, the modelling approach in this work first converts geological fracture density into a corresponding set of penny-shaped cracks according to Hudson (1980), but then makes use of the relation between the two theories' parameters and calculates the effective elastic parameters based on linear slip theory (Schoenberg and Douma, 1988).

Elements of the Rock Physics Modelling Scheme

The following subsection includes a description of the rock physics modelling approach, and how the different elements of the rock (minerals, pores, fractures) are incorporated. The scheme presented here is then used to perform the rock physics modelling described in the end of section 4.2. A specifically tailored programming script was created as a part of this study.

Estimating the effective elastic property of a rock requires the definition of volume fraction, elastic moduli as well as the geometrical arrangement of all existing phases (Mavko et al., 2009). For the volcanic sill model, this is achieved by the execution of the following steps in analogy to Xu and Payne (2009), as figure 2.5 illustrates.

1. Bulk and shear moduli of the solid, non-porous mineral matrix is calculated using the Reuss-Voigt-Hill average of the present minerals (Mavko et al., 2009).

2. Pore space (excluding fractures at this point) is implemented using the differential effective medium model (DEM). Berge et al. (1992) demostrated that DEM theory produces good results for basalts of varying microstructure, which provides a good argument for the use of DEM in volcanc sills. The method is based on a thought experiment where small inclusions of a phase are iteratively added to a host phase (the matrix) using single scatter theory. After each step, the calculated effective modulus is chosen as the new host phase modulus for the next step, until the whole volume fraction of the second phase has been added. Mathematically, this expressed by a system of differential equations (Mavko et al., 2009):

$$\begin{aligned}(1-y)\frac{d}{dy}K^*(y) &= (K_2 - K^*)P^{(*,2)}(y) \\ (1-y)\frac{d}{dy}\mu^*(y) &= (\mu_2 - \mu^*)Q^{(*,2)}(y)\end{aligned} \tag{2.6}$$

   Initially, the effective bulk and shear moduli of the initial solid phase are $K^*(0), \mu^*(0) = K_1, \mu_1$, respectively. K_2, μ_2 are the inclusion bulk and shear moduli, and y is the overall volume fraction of the pores. The shape factors $P^{(*,2)} and Q^{(*,2)}$ are given in equation 2.7 below. Pore geometry is assumed to be ellipsoidal with large aspect ratios ($\alpha > 0.1$) and randomly oriented. Pore fluid moduli are either added directly to simulate high-frequency behaviour (isolated pores, no fluid pressure

equilibration), or pores are left empty and fluids are added at a later stage using Gassmann fluid substitution to account for pore pressure equilibration (Mavko et al., 2009; Xu and Payne, 2009). For penny-shaped inclusions in a background medium (indices i and m, respectively), the formulae for the shape factors are:

$$\begin{aligned} P^{(m,i)} &= \frac{K_m + \frac{4}{3}\mu_i}{K_i + \frac{4}{3}\mu_i + \pi\alpha\beta_m} \\ Q^{(m,i)} &= \frac{1}{5}\left(1 + \frac{8\mu_m}{4\mu_i + \pi\alpha(\mu_m + 2\beta_m)}) + 2\frac{K_i + \frac{2}{3}(\mu_i + \mu_m)}{K_i + \frac{4}{3}\mu_i + \pi\alpha\beta_m}\right) \\ \beta_m &= \mu_m \frac{3K_m + \mu_m}{3K_m + 7\mu_m} \end{aligned} \tag{2.7}$$

K and μ again represent the bulk and shear moduli of the respective medium indicated by the index.

3. Fractures can be added assuming either randomly oriented cracks (isotropic case) or aligned fracture sets with preferred orientation (anisotropic case).
Isotropic case: Cracks are again added using DEM modelling, just with a much smaller aspect ratio for ellipsoids. The general effect of aspect ratio is that thinner fractures produce stronger effects (Xu and Payne, 2009).
Anisotropic case: Excess compliances for each set of fractures may be calculated for mainly two cases. Schoenberg and Douma (1988) give equations for fluid filled penny-cracks:

$$\begin{aligned} E_t &= \frac{16}{3\,(3 - 2\gamma_b)}e \\ E_n &= \frac{4}{3\gamma_b\left(1 - \gamma_b + \frac{K_f}{\pi\alpha\mu_b}\right)}e, \end{aligned} \tag{2.8}$$

which can also be used for dry cracks by setting the fluid bulk modulus K_f to zero. In equation 2.8 K_b, μ_b and γ_b represent the bulk modulus, shear modulus and ratio of P-wave to S-wave velocity of the background medium, respectively. e is the seismic crack density introduced in equation 2.4. When fluid filled fractures are embedded in a porous host rock and are allowed to communicate in terms of fluid flow for pore pressure equilibration, E_t is the same as in eq. 2.8, but normal fracture compliance becomes (Schoenberg and Douma, 1988)

$$E_n = \frac{4}{3\gamma_b(1 - \gamma_b)} \frac{1 - \frac{K_f}{K_b(1-\phi_f/\phi_p)}}{1 + \frac{K_f/K_b}{1-K_f/K_b}[\frac{3}{4\gamma_b}\frac{3-4\gamma_b}{3\pi\alpha\gamma_b(1-\gamma_b)}\frac{1}{1+\phi_p/\phi_f}]} e. \tag{2.9}$$

The latter case assumes that background porosity ϕ_p consists of approximately spherical pores, but Thomsen (1995) notes that pressure equilibration effects should also occur with interconnected fracture sets. Because explicit expressions for communicating fractures were not available, the workflow violates this assumption and uses the entire remaining porosity outside the modelled fracture set as ϕ_p, while fracture porosity of each set is represented by ϕ_f.

To compute the overall effective moduli of the rock containing multiple fracture sets, excess compliances are first calculated in a local coordinate system, then transformed into global coordinates, and finally summed up and added to the background compliance. Inverting the resulting compliance matrix then yields the effective stiffness tensor in global coordinates. This can subsequently be rotated such that its symmetry is closest to orthotropy (or higher symmetry if applicable) to be suitable for quantification of anisotropy parameters for up to orthorhombic symmetry (Tsvankin, 1997). These parameters represent an extension of the famous results of Thomsen (1986) and Rüger and Tsvankin (1997) for horizontal and transverse isotropy, respectively. A more extensive discussion of the parameters and related theoretical considerations is beyond the scope of this work. However, a brief description of the parameter's meaning is given in table 2.1. Calculation of P-wave velocities for all propagation directions in up to orthorhombic symmetry can then be done using the approximate formulas (not shown here) derived by Tsvankin (1997).

Knowledge of fracture effects leading to anisotropic elastic parameters and seismic velocities can significantly benefit the integratation of hydrocarbon exploration data on different scales, such as seismic imaging and sonic well logs (Grechka and Kachanov, 2006; Xu and Payne, 2009). Since log velocities are measured in the direction of the well trace, sonic logs can be used for comparison with the corresponding directional velocity obtained from rock physics modelling. In this way, proposed rock models may be tested and constrained. In addition, crack-induced azimuthal variations of seismic velocities on the seismic scale lead to detectable, direction-dependent variations in of reflection amplitudes. Investigations of such amplitude variations with azimuth and angle are termed AVAz surveys. In fact, an important motivation of this work is reports of initial successes in seismic detection of fractured zones in volcanic reservoirs in the Rio Grande Valley, which needs to be linked to geological observations (*YPF*, pers.comm.).

Table 2.1: Summary of anisotropy parameters introduced by Tsvankin (1997) for up to orthorhombic symmetry.

Parameter	Description
$\varepsilon^{(1)}$	the VTI parameter ε in the symmetry plane [$x2$; $x3$] normal to the $x1$-axis; close to the fractional difference between the P-wave velocities in the $x2$- and $x3$- directions
$\delta^{(1)}$	the VTI parameter δ in the [$x2$; $x3$] plane; responsible for near-vertical P-wave velocity variations, also influences SV-wave velocity anisotropy
$\gamma^{(1)}$	the VTI parameter γ in the [$x2$; $x3$] plane; close to the fractional difference between the SH-wave velocities in the $x2$- and $x3$-directions
$\varepsilon^{(2)}$	the VTI parameter ε in the symmetry plane [$x1$; $x3$] normal to the $x2$-axis; close to the fractional difference between the P-wave velocities in the $x1$- and $x3$- directions
$\delta^{(2)}$	the VTI parameter δ in the [$x1$; $x3$] plane; responsible for near-vertical P-wave velocity variations, also influences SV-wave velocity anisotropy;
$\gamma^{(2)}$	the VTI parameter γ in the [$x1$; $x3$] plane (close to the fractional difference between the SH-wave velocities in the $x1$- and $x3$-directions)
$\delta^{(3)}$	the VTI parameter δ in the [$x1$; $x2$] plane ($x1$ is used as the symmetry axis); responsible for near-vertical P-wave velocity variations, also influences SV-wave velocity anisotropy

3 Fieldwork and Subsurface Data

The following section will summarise the data available datasets, including data obtained from field work and subsurface data comprising well and seismic sections. These datasets are provide the input data for the workflows presented in sections 4. Section 3.2 also includes a brief summary of the analysis techniques that were applied to the subsurface data.

3.1 Field work

A four week fieldwork campaign was conducted at several outcrops in the northern Neuquén Basin in March 2016. Approximately two weeks were dedicated to the El Manzano field site to execute the following tasks. First, several drone-based surveys were carried out along a roughly 4 km long and up to 250 m high outcrop to collect the photographs for Structure from Motion (SfM). Highly accurate differential GPS measurements of 63 ground control points were taken along the entire outcrop to ensure correct global orientation and positioning of the resulting models. The surveys for SfM comprise a total of 254 photographs and were conducted at different distances from the outcrop to produce input for models of different levels of detail. While the large scale survey was taken at lower resolution by flying several 100 m from the outcrop, a small area at the southern tip of the outcrop was recorded at higher resolution by flying less than 100 m from the outcrop. In this smaller area, dedicated structural measurements of host rock bedding and major fracture planes were also taken for later comparison to the SfM-based data. Six scanlines of 1.5-6 m length were collected in two, approximately 10-15 m thick sills. Furthermore, considerable exploratory effort was taken throughout the campaign to develop a better understanding of present structures and constrain small scale geometries in the sill complex. This provided important additional information for later interpretation of the virtual outcrop models. Figure 3.1 illustrates some of the activities. More fieldwork photographs will be integrated in the workflow descriptions, and a summary of the datasets and field activities is given in appendices A.1 and A.2.

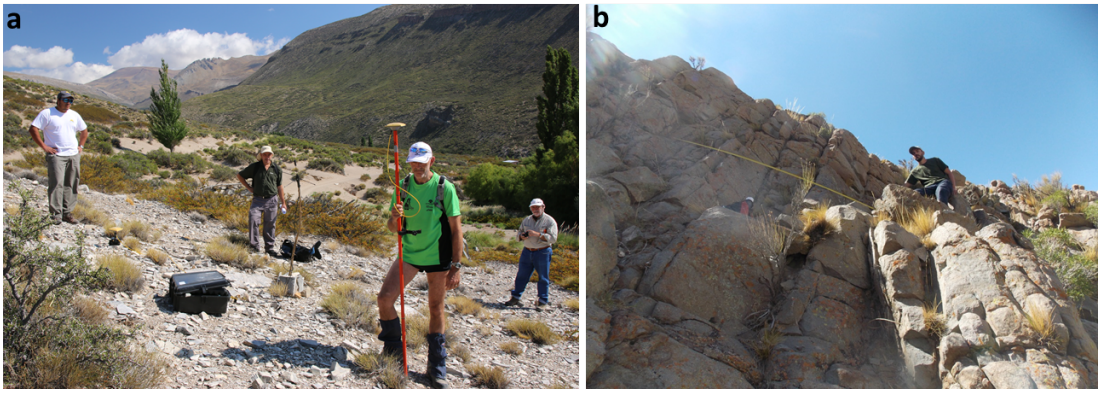

Figure 3.1: Photographs illustrating fieldwork activities such as (a) differential GPS measurements and (b) manual scanline measurements. Photos by Olivier Galland and Juán Spacapan.

3.2 Subsurface Data

Three wells from Rio Grande Valley (referred to here as wells A, B and C) were used for lithology characterisation. The wells intersect numerous intrusions at different depth levels and provide logs for gamma ray (GR), caliper, sonic velocity, resistivity. Well B includes an additional density log. Based on a combination of well tops from geological well reports and manual interpretation, a discrete lithology log was established to sort all logs by lithology. Sills are commonly assumed to exhibit a typical log signature including very high sonic and resistivity values and very low GR (Planke et al., 2014). The lithology log was then used to obtain log statistics and property crossplots in order to examine property variations and potential correlations between different physical properties. A crossplots consists of two quantities measured at the same depth that are plotted on the x and y axes. Here, Sonic and density logs were given particular attention, because they provide important constraints for seismic impedance which is the key parameter in seismic modelling.

For comparison to seismic modelling results, a 3D prestack time migrated (PSTM) seismic cube was available. However, since detailed seismic interpretation is beyong the scope of the study, the seismic data were used to perform and discuss a qualitative comparison of modelled and real seismic data.

4 Implementation of Methods

4.1 Workflow A - From Virtual Outcrop Interpretation to Seismic Modelling

Workflow A Overview

An important component of this work was the creation of a workflow for geomodel building from virtual outcrop models (VOM) that is suitable for geological data integration. The resulting geomodels serve as the foundation of subsequent seismic modelling. To maintain maximum flexibility and facilitate integration of virtual outcrop data with other data types, for instance well or seismic data, as many steps as possible were performed using widely used commercial software packages. The procedures described in this section include the entire path from generating a virtual outcrop model using SfM, the generation of a 3D property grid, and the use of this grid for seismic modelling. The specific parameters used for the SfM case study at El Manzano will be provided in this section and may serve as an example of a typical use of the workflow.

Generation of the Virtual Outcrop Model

The photographs collected during the drone survey at the field sites around El Manzano were processed according to the steps described in section 2.1. Keypoint detection, point cloud calculation and generation of a textured triangulated mesh are almost completely automated. Ground control points with known GPS coordinates were placed interactively on the pointcloud for georeferencing. Figure 4.2 illustrates the main steps in the SfM workflow for this study, including acquisition of photographs and ground control points as well the resulting point cloud with indicated ground control points and camera positions. In the case of El Manzano, both interpretation of the sill complex on the kilometre-scale and fracture interpretation on the metre-scale were key goals to be conducted. In order to adjust the models to the specific demands while keeping maximum efficiency, two models were calculated. For the large scale model, the point cloud was calculated at the medium quality preset of Agisoft Photoscan, yielding approximately 100 million points for an

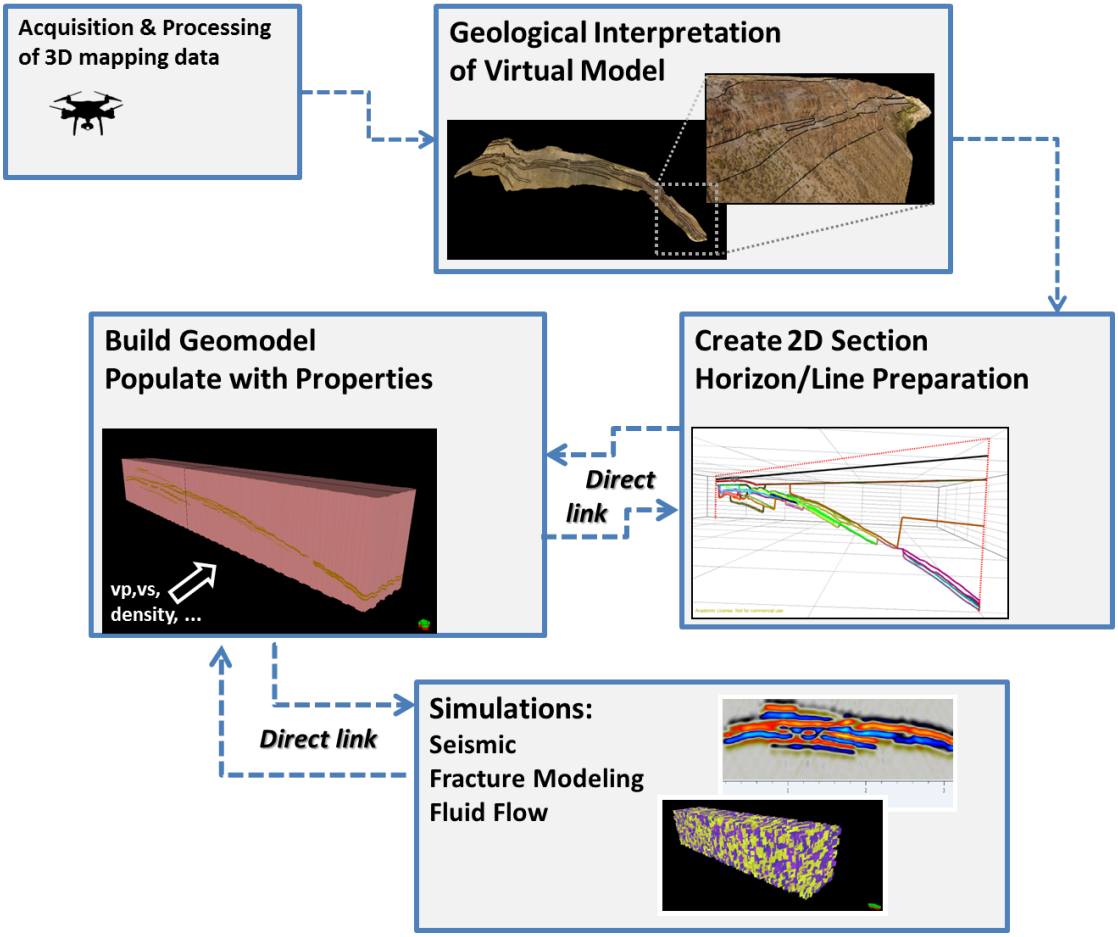

Figure 4.1: Main steps of the workflow A from interpretation of the virtual outcrop model to seismic modelling, indicating main tasks that were performed at each stage.

outcrop of roughly 4 km x 50-250 m. The mesh was calculated in 10 subsets of roughly 1-6 million triangular faces to limit the individual file size and allow for good performance during the interpretation stage. In contrast, the part of the outcrop designated to fracture network characterisation (see section 4.2) was calculated at high point cloud density, leading to 31 million points on some 350 m x 70 m of outcrop. The corresponding mesh included 1.4 million triangles on the same area, yielding an average area of around 1.7 dm^2 per triangle. Each mesh was textured using the drone photographs to generate a photo-realistic VOM. However, it should be kept in mind that the resolution of the surface representation is much smaller than photo texture resolution. In other words, fractures and other small scale features which might be visible on the photo texture are often not resolved as surfaces.

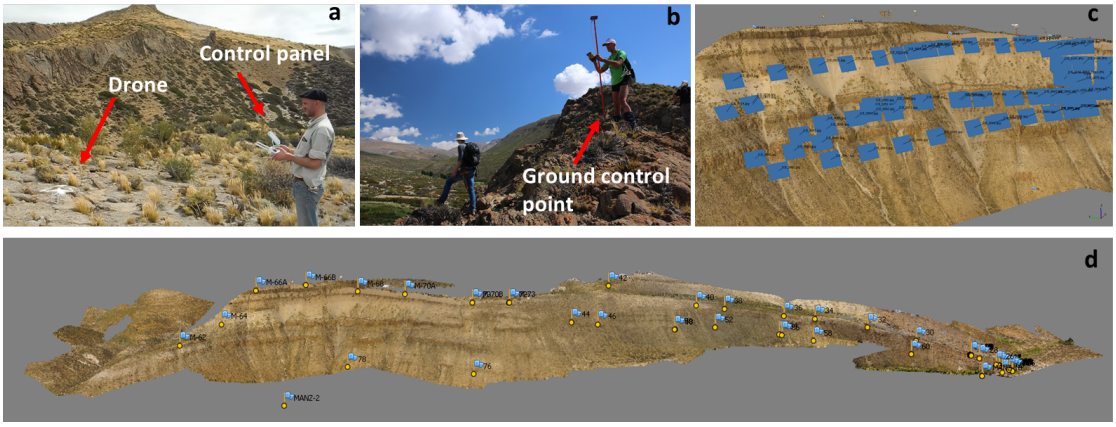

Figure 4.2: Main steps of the Structure from Motion survey caried out for this study. (a) Drone flights for data acquisition and (b) differential GPS measurements of ground control points was done during fieldwork. (c) Camera positions relative to the main outcrop wall are indicated by the blue squares, and (d) shows the full scale resulting point cloud comprising around 100 million points, and indicates ground control points positions along the outcrop (flags).

Interpretation of the Virtual Outcrop Model

The VOM was subsequently imported to a dedicated interpretation software (*LIME* 2016). This can be used to interpret, for instance, layer and intrusion geometries on the VOM and create polygons which then serve as input data for the later stages of the model building process. In addition, planes can be defined by choosing 3 points on the VOM which is a useful tool to define fault or fracture planes as input for fracture modelling as described in section 4.2. Where VOM quality did not suffice to make confident decisions, outcrop photographs and field notes or measurements were used to support the interpretation.

Data Preconditioning for Geomodel Building

The polylines were subsequently edited using a geomodelling software environment to prepare the line horizons that build the foundation of the final geomodel. Although the outcrop exhibits 3D geometries, the geological layers and especially sills could not be defined in the third dimension with high confidence. This was mainly due to the significant degree of lateral variations within the igneous bodies which were difficult to follow in the third dimension. Therefore, it was decided to focus on preserving as much details as possible in the vertical direction and aim for a 2D model with constant horizon depth in the third dimension. For this purpose, the original interpretations were

projected on a section aligned with the outcrop face. This caused small artefacts like sudden jumps or loops in the projected lines that were manually corrected. Additionally, no lines were allowed to cross and all lines had to cover the entire length of the section, because the geomodel building at a later stage was based on consecutive allocation of properties below each horizon (or above, but this must be consistent). Wherever an interpreted sill terminated, top and bottom contact were merged and followed the nearest contact above. This procedure ensures that the model does not change outside of the sills. All other software used in the next steps communicate in real-time, making file exchange between project simple, quick and well organised.

Geomodel Building

During the next stage of the workflow, the projected lines were used to create horizons whose extent also determined the extent of the final grid in the third dimension. The gridded geomodel was initiated as a rectangular grid of 4000 m x 2 m x 600 m (thus essentially 2D). The x,y,z-increments were chosen to define the size of the individual cells. Depending on the modelling task, these values may range from 1 m to several 10 m or 100 m. For the seismic modelling case described below, all increments were set to 1 m to preserve the high level of detail from the VOM interpretation. In order to create the internal model geometries that represent the lithology, the software defines hierarchy for subdividing a grid. First, the grid is divided it into "zones" following input horizons (quotes indicate intra-software terminology to avoid confusion with geological definitions). These "zones" are then subdivided by "layers" which define "facies". The first process may change the cell shape by splitting cells along a horizon to generate a "zone", while this is not the case with the "layering/facies" subdivision which maintains the cell shape and decides the cell value by volume fraction. Because the desired input for the seismic modelling software was a property cube in seg-y format which has to be cube shaped, the subdivision was made using the "layer/facies" option, although this leads to small steps along the geological boundaries. However, it is generally also possible to use the "zone" option and only import the layer boundaries, but the decision will depend on the task. Subsequently, P-wave velocity, S-wave-velocity and density values were allocated to the facies. Following a simple binary approach, the "facies" of the models were (1) sill and (2) host rock. The model was then converted into a seg-y cube.

At this stage, the geomodel is ready to be used for simulations. Although the specifics described here produce a suitable model for seismic modelling using the 2D/3D filter method described in section 2.2, it is easily adapted for other modelling purposes, for

instance fracture modelling (compare section 4.3) or fluid flow modelling.

Seismic Modelling

The direct link between software was used to transfer the property cube that contained the seismic properties to the seismic modelling software. The internal target model for the seismic modelling was directly generated from the property cube. This made it straightforward to set up a number of endmember cases to test the sensitivity of the modelling results to the signal frequency, angle-dependent illumination, and seismic properties. The seismic properties were based on the results of statistical analysis of well data which are presented in chapter 5.2. Two endmember cases for acoustic impedance were defined by considering a high P-wave velocity for sills and a low P-wave velocities for host rock, and vice versa. Here, 'high' and 'low' values correspond to the center of the first and last bin from a histogram of the sonic logs that comprises at least 5% of the total count. Density values were defined as the mean well log value for each lithology. S-wave velocities were derived from P-wave velocities using v_P/v_S ratios of 1.7 and 1.9 for host rock and intrusions, respectively (Klarner and Klarner, 2012; Fernandez-Concheso, 2015). For each endmember case of seismic properties, constant angle sections were calculated for incident angles of 0°, 15° and 30°. This is a typical approach to examine smearing effects for increasing angles of incidence. The seismic signal was assumed to be a zero-phase Ricker wavelet. Center frequencies of 20 Hz, 30 Hz and 40 Hz were used to assess the effect of frequency on the seismic image resolution.

Because no overburden or survey parameters were available, the PSF was generated according to user-defined parameters. The average velocity, which should resemble migration velocity, was estimated by the arithmetic average of the lithologies' P-wave velocities. As a typical estimate for a simple overburden model, the maximum illuminated dip was set to 45°. The target cube was sampled at 1 m in all directions to avoid artefacts due to undersampling. Despite the high grid resolution of 1 m, each simulation took less than 15 minutes. This allows quick adjustments and quality control to be made. At this stage, the synthetic 2D seismic sections were ready to be evaluated and compared to actual seismic data from Rio Grande Valley.

4.2 Workflow B - From Fracture Network Characterisation to Rock Physics Modelling

Workflow B Overview

The second workflow that was created during this study aims at an integration of outcrop, core, and well data in order to characterise the fracture network of rocks and use the results rock physics modelling of elastic rock properties and seismic velocities. This represents an attempt to bridge the gap to fracture detection in seismic exploration, where studies of azimuthal variations of seismic amplitude vs incident angle (azimuthal AVA, or AVAz) are performed (see e.g. Tsvankin et al., 2010; Far et al., 2013). Note that the term AVA is used instead of instead of the more commonly used AVO, since offset only provides information on the angle of incidence in the specific case of flat horizontal layers. Typical parameters obtained by AVAz studies are dominant fracture orientation and density (parameter e introduced in section 2.4) which are valuable, but cannot provide detailed information on important fracture network characteristics like fracture size or hydraulic properties. This highlights the necessity of complementary studies to quantify these characteristics. A special issue of the Geophysics journal devoted to this topic is currently (2016) in preparation, underlining that detailed fracture network characterisation is an ultimate frontier in geophysical exploration. Since fracture networks of rocks depend on a number of parameters including rock mechanical properties and the tectonic stress regime (both current and paleostresses), they are highly site specific and attempts to characterise subsurface fractures should aim at data integration from multiple sources (e.g. Senger et al., 2013). The workflow presented here builds on fracture measurements obtained from existing VOMs and field data. Based on these measurements, modelling of fracture networks is employed. Finally, a rock physics modelling uses the modelled fracture properties to predict seismic velocities and fracture induced anisotropy. Note that except for the rock physics module, the workflow presented here is in principle the same as the one recently published by Casini et al. (2016) - although the workflows were established independently. Figure 4.3 gives a visual impression of the workflow elements.

Fracture measurements the from Virtual Outcrop Model

Before explaining the first step of the workflow, note that that VOMs of sufficiently high detail to resolve fractures are required. For this work, a mesh covering rougly 370 m x 70 m and containing 1.4 million triangles, was produced for two sills in the southern part of the El Manzano outcrop. In the same area, field measurements of

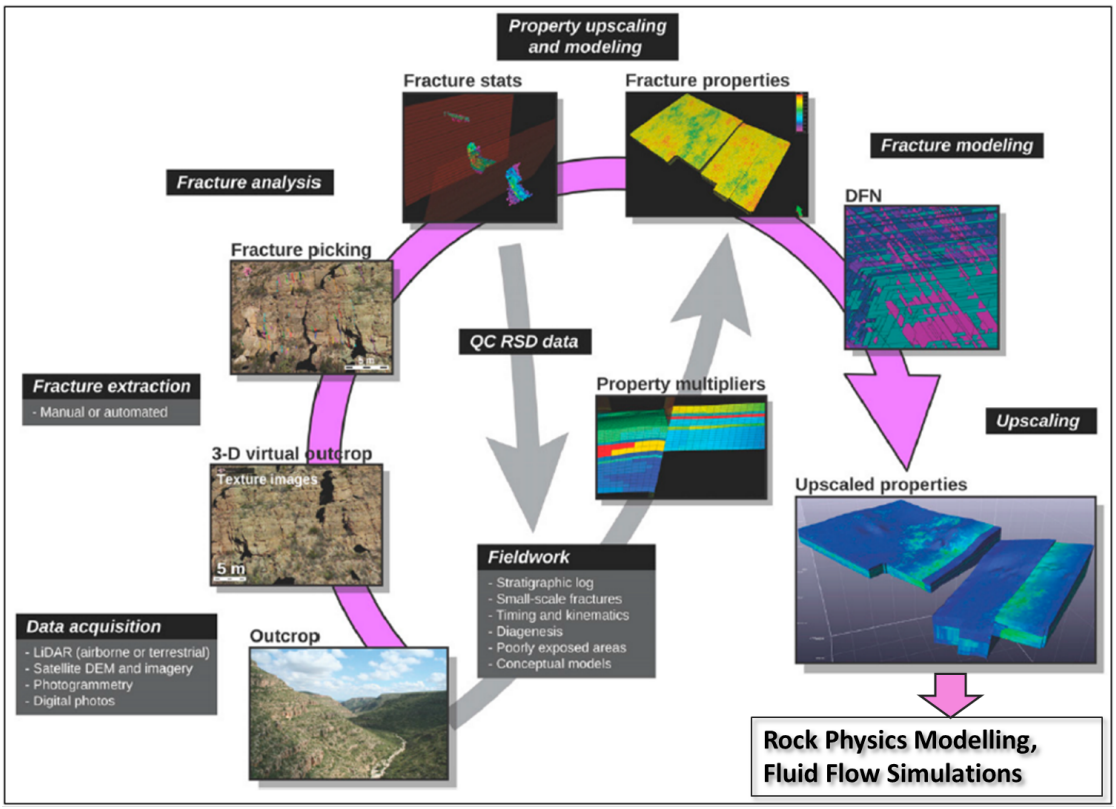

Figure 4.3: Main steps of the workflow B from outcrop data acquisition to fracture and rockphysics modelling, indicating main tasks and potential additional means of quality control. Edited from Casini et al. (2016).

fractures were collected (figure 4.4a). Analogous to scanline measurements obtained directly from fieldwork, VOMs can be used to produce virtual scanlines as a way to quantify 1D fracture frequency (P10). This can be achieved with automated picking techniques or manual picking of fracture planes which the give both size and orientation of the planes (Casini et al., 2016). In this study, fractures were manually picked along 75 virtual scanlines which are summarised in appenix A.3. To ensure good lateral coverage and minimise outcrop orientation bias, a total of 61 scanlines were placed parallel to the sill-host contacts in two sills visible in figure 4.4. The sills were referred to as upper and lower sill, respectively, and each sill was subdivided into three zones: Zone 1 at the bottom contact between sill and host rock, zone 2 in the center of each sill, as well as zone 3 the top contact (see figure 4.4b). In order to improve the representation of subhorizontal fractures in the data, 14 scanlines were taken across both lower and upper sill, i.e. normal to the sill-host contact. The detailed VOM from El Manzano and close-up

views of virtual scanlines and fracture measurements are presented in figure 4.4, along with a stereoplot of the scanline orientation.

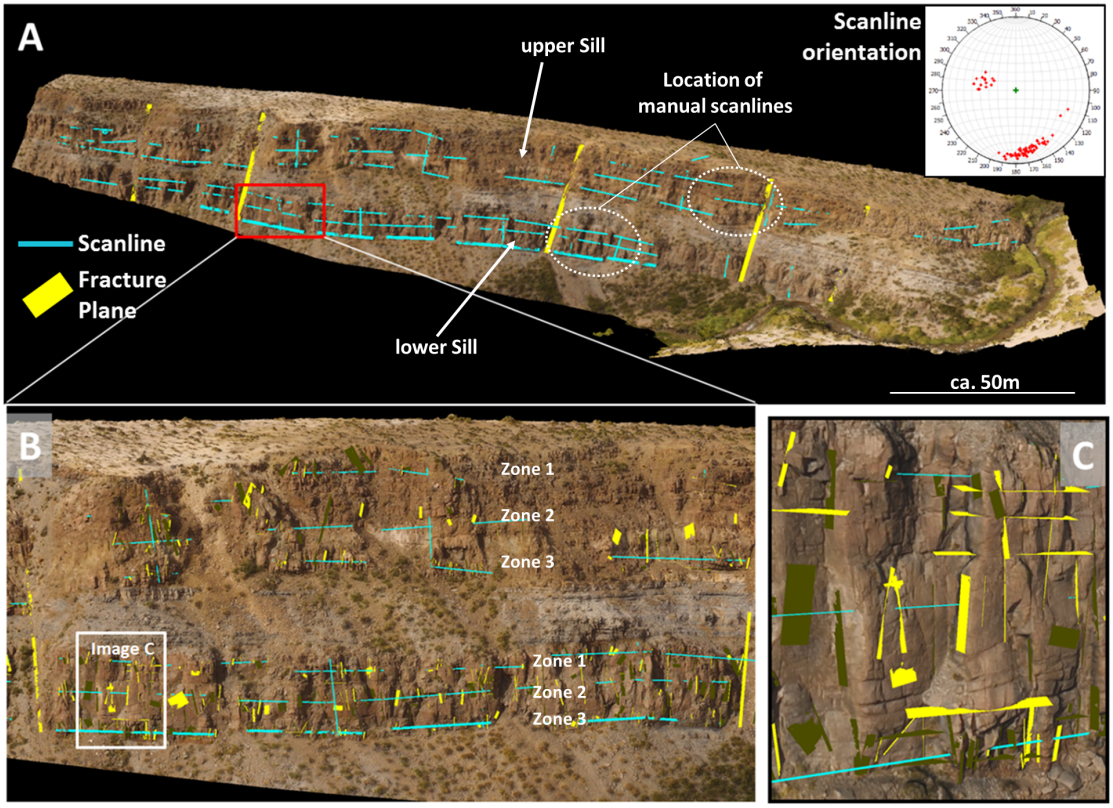

Figure 4.4: (a) Full view of the detailed virtual outcrop model of the southern part of the El Manzano outcrop, indicating intrusions defined as lower and upper sill, as well as locations of scanlines. The stereoplot indicates orientations of all scanlines. (b) Close-up view displaying the zonation chosen for virtual scanlines. (c) Close-up view demonstrating high level of details and examples of manually picked fracture planes.

Fracture Data Analysis

For each virtual scanline, an average P10 (1D fracture frequency) was then calculated regardless of fracture orientation. Stereoplots comprising (1) the entire dataset and (2) the individual sills were then used to identify fracture sets. P10 values for each identified fracture set were obtained as follows: The fracture count for the set (usually mean orientation ± 10-15 degrees) was divided by the total fracture count to calculate a number-percentage. This percentage was then multiplied with the average P10 value obtained of each scanline. Since fracture modelling in the later stage of the workflow requires a P32 (fracture density) input value, P10 average and standard deviation of each

set were calculated for the individual sills as well as the entire dataset. The resulting values were then corrected for scanline orientation by applying equation 2.3 using the average C_{P3} factor based on the scanline orientation distribution.
Measures for fracture length (or size) from the virtual planes have to be treated with care because the picked planes do not necessarily cover the entire fracture length. Therefore, and by taking into account mesh resolution and fieldwork observations, it was estimated that (1) the maximum fracture length was set to be equal to the sill thickness (10-15 m) and (2) the minimum fracture length resolved was estimated to be between 2-5 m. The data obtained from VOM based measurements then underwent quality control by comparing results to field data. A good justification for this is that P10 variation from virtual scanlines is often more strongly influenced by outcrop orientation and quality than actual changes in fracture frequency and must be treated with care (Senger et al., 2013; Casini et al., 2016).

The analysis procedure was also applied to scanline measurements obtained during fieldwork. This was done for two reasons: (1) Quality control of the virtual data, and (2) comparison of fracture patterns on different scales of fracture length (approximately 10 m vs 1 m from virtual and fieldwork scanlines, respectively). The scanline data from fieldwork was sorted by fracture length, and only fractures of 0.5-2 m length were included in the assessment of orientation patterns and the calculation of P10 and P32 values. However, due to the small number of fieldwork scanlines, orientation patterns were mainly considered for qualitative comparison to virtual scanline results. In order to obtain P10 and P32 per set, the percentage factors obtained from virtual scanlines were used. As long as the orientation distribution was approximately the same, this approach was deemed justifiable.

Discrete Fracture Network Modelling

In the next stage, a gridded geomodel was created in a similar fashion as described in section 4.1. The differences here were that the size of the grid was adapted to the part of the outcrop where the scanlines were taken, and the grid increments were set to 5x5 m laterally and 1 m vertically. For the model dimensions of 350 m x 100 m x 70 m, this yielded around 100,000 cells and ensured both sufficient grid resolution and acceptable calculation time. The grid was then used to set up two fracture modelling cases in the form of statistical discrete fracture network (DFN) models:

1. Fracture model 1 was based on the results from the virtual scanlines including fracture density, orientation distribution for each set of fractures. All fractures were given an estimated average length of 10 m based on the considerations regarding fracture size represented in the VOM data that were discussed in the subsection on fracture data analysis.

2. Fracture model 2 was based on the results from scanlines obtained during fieldwork in terms of 1D fracture frequency and estimated fracture length (1 m). However, the orientation distribution and associated correction factors to obtain fracture density (P32) were kept the same as in fracture model 1. This decision relies on the assumption that the results from virtual scanlines were more robust due to the much larger dataset.

DFN modelling calculates parameters such as fracture count and the associated fracture porosity for all fractures in a model. Since rock physics requires these parameters for each set of fractures, the sets were modelled individually - bearing in mind that this approach is probably not suited for other types of modelling such as fluid flow simulations. The results of the fracture analysis described in the previous step were used as input for each DFN modelling case. The fracture aperture, and accordingly the aspect ratio, was constrained from core measurements to be in the range of 0.5-3 mm. However, which aperture was associated with which fracture length could not be identified. Because of the comparatively large fracture lengths, it was decided to use the upper endmember of aperture, i.e. 3 mm. Note that this decision has no effect on seismic crack density, but does affect normal fracture compliances via aspect ratio and porosity (equation 2.9). Here, all fractures were realised explicitly, however this was only possible due to the decision to include exclusively one type of large fractures rather than a typical fractal length distribution. In the latter case, an upper boundary for length of explicitly calculated fractures must be defined in order to keep computation times within a reasonable limit.

Rock Physics Modelling

The final step of the workflow included rock physics modelling of elastic rock properties and P-wave velocities based on the methods explained in section 2.4. For the rock matix, a simple mineral composition of 80% plagioclase and 20% pyroxene was chosen. The results of the DFN modelling served as the input for the implementation of fractures. The calculation of fracture compliances requires a value for the seismic crack density e which can be obtained in two ways (see equation 2.4). The original definition of crack density by Budiansky and O'connell (1976) uses the number of fractures, their average radius and

reference volume. Instead, it is also possible to calculate the seismic crack density from the fracture porosity and aspect ratio associated with the fractures. Both approaches rest on the assumption of circular or penny-shaped cracks, which was approximated by the rectangular shaped fractures realised in the DFN modelling. Isotropic modelling using DEM theory requires the porosity-aspect ratio approach, while the combined Schoenberg-Hudson method does not. For the isotropic case, the porosities obtained from DFN modelling were used as input for DEM based calculations. In contrast, the original definition using fracture count was applied to all calculations based on linear slip theory applied in order to avoid additional bias by the poor constraint on aspect ratio (aperture/length). For all cases, interconnected, water saturated fractures and pores were assumed. Two base cases were considered, including (1) only one fracture set, or (2) all sets with preferred orientation. In both cases, a population of randomly oriented fractures was implemented to represent cooling joints. For each base case, four sub-models were calculated to explore different scenarios based on field and core observations. This yields a total of 8 modelling cases:

1. Model 1 corresponds to fracture sets with orientation, crack densities and porosities taken from VOM-based fracture modelling without further modification (related modelling cases referred to as 1,2).

2. Model 2 contains sets of the same orientation, but crack density and porosity are reduced by 75% to account for potentially filled or closed fractures at depth (related modelling cases referred to as 3,4).

3. Model 3 contains the same reduced fracture fracture population as model 2, but a cracks with higher aspect ratio are added based on results from field-based fracture measurements and applying the same reduction by a factor of 4. This model aims at investigating the effect of interacting fracture populations with slightly different geometries (related modelling cases referred to as 5,6).

4. Model 4 is also a modification of model 2. However, it does not change fracture parameters but instead introduces vuggy porosity into account by using a matrix containing 5% randomly oriented pores of aspect ratio 0.5 which are assumed to be interconnected with the fractures (related modelling cases referred to as 7,8).

The precise input parameters for all rock physics modelling are addressed in the results section, because they represent part of the results of the study.

The resulting elastic stiffness tensor provided the basis to quantify anisotropy by means of anisotropy parameters for up to orthorhombic symmetry (Tsvankin, 1997), which also lead to an estimation of P-wave velocities for all incident angles and azimuths. Figure 4.5 illustrates such a directional velocity plot, where velocity values are represented as a colour code. Note, that as the velocity field is rotationally symmetric, it is sufficient to plot azimuths from 0-180°.

Looking at velocities for incident angles from vertical to horizontal along different azimuthal directions in figure 4.5 can give a good impression of the degree of P-wave anisotropy: To follow wave velocities from vertical to horizontal incident angle (corresponding to 0-90°) at different azimuth, the reader must follow the dotted lines. These are associated with different azimuths as indicated by the models on the lefthand side of figure 4.5. Note that in the rock physics context, the term "azimuth" refers to the angle between the local x1-axis and the projection of the ray in the x1-x2-plane.

These azimuthal variations are is the basis for analysing azimuthal variations of reflection coefficients (AVAz). If successful, AVAz can be used to recover preferred fracture orientations and seismic crack densities (Lynn, 2004; Far et al., 2013). Note that the term "azimuth" refers here to the angle between the local x1-axis and the projection of the ray in the x1-x2-plane. Therefore, it may not coincide with the geological definition of "azimuth". The velocity maps can also be used in combination with well logs and well orientations to constrain potential rock models which could explain the measured parameters. Creating a reliable link between reservoir properties such as pore space and fracturing in the sills and seismic scale observations would be a valuable contribution to the characterisation of sill reservoirs.

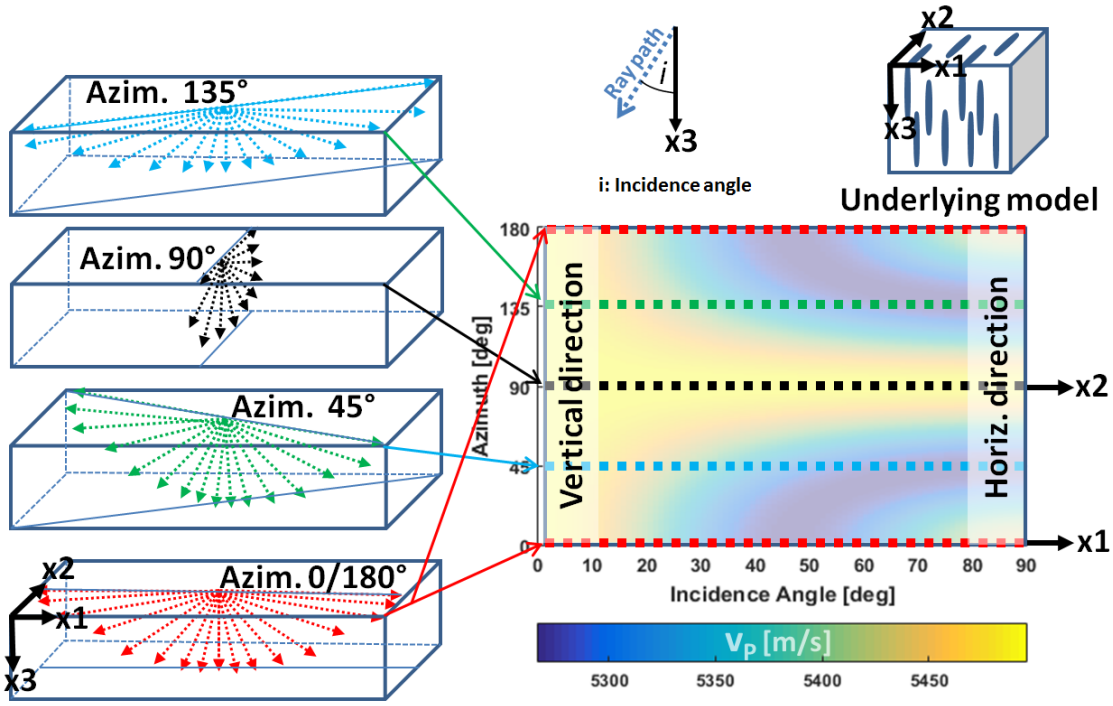

Figure 4.5: Example of a directional velocity plot obtained from rock physics modelling, with velocities displayed as a colour code. The diagrams on the lefthand side show various incidence angles for a given azimuth. The block diagram in the top right corner illustrates the underlying rock model.

5 Results

The presentation of the results follows the workflows A and B described in chapter 4.1 and 4.2, respectively. The large-scale virtual outcrop model (VOM) of the El Manzano outcrop is presented first, followed by the results of the seismic modelling that addresses the effects of signal frequency, angle of incidence, and elastic rock properties on the synthetic seismic images. Thereafter, the fracture orientation patterns and fracture density obtained from the fracture measurements are shown followed by a brief summary of the DFN modelling output. This finally leads to the corresponding results of the rock physics modelling, which represents the link to the observations on the seismic scale.

5.1 Virtual Outcrop Model of the El Manzano Sill Complex

The work described in workflow A (section 4.1) was completed in the course of approximately 3-4 weeks. The virtual outcrop model (VOM) of the southern part of the El Manzano sill complex extends over roughly 4 km and yields more than 30 individual sills and sill branches of individual thickness between approximately 1-30 m. Figure 5.1a presents the full-scale VOM in its uninterpreted form is shown along with the VOM including the geological interpretation and the resulting cellular geomodel 5.1b and c, respectively. Common observations include closely stacked sills, internal zonation on the metre-scale, sill terminations, branches and junctions, metre-scale offsets due to (1) primary stepping and (2) minor faulting, as well as lateral and vertical variations of visible fracture patterns. This illustrates the potentially high level of geometrical complexity within sill complexes. Examples showing these elements in the VOM are given in figure 5.2, also highlighting the high resolution of the model texture which allows interpretation on the metre-scale. Areas where field notes and photographs are used to support confident interpretation of small scale features like host rock lenses, sill terminations and ambiguous sill contacts are shown figure 5.3. However, the geomodel preserves the high level of detail seen in the VOM due to the small cell size. For the purpose of seismic modelling, each cell is populated with P-wave and S-wave velocity as well as density based on the results from well analysis (see section 5.2 below).

Figure 5.1: 3D view of the entire virtual outcrop model of El Manzano in raw form (a) and with interpreted sill complex (black lines, b). A section through the resulting model is shown in (c) with red and dark areas representing sills and host rock, respectively. The images are vertically exaggerated by a factor 2. Blue squares indicate locations of close-up views shown in figure 5.2.

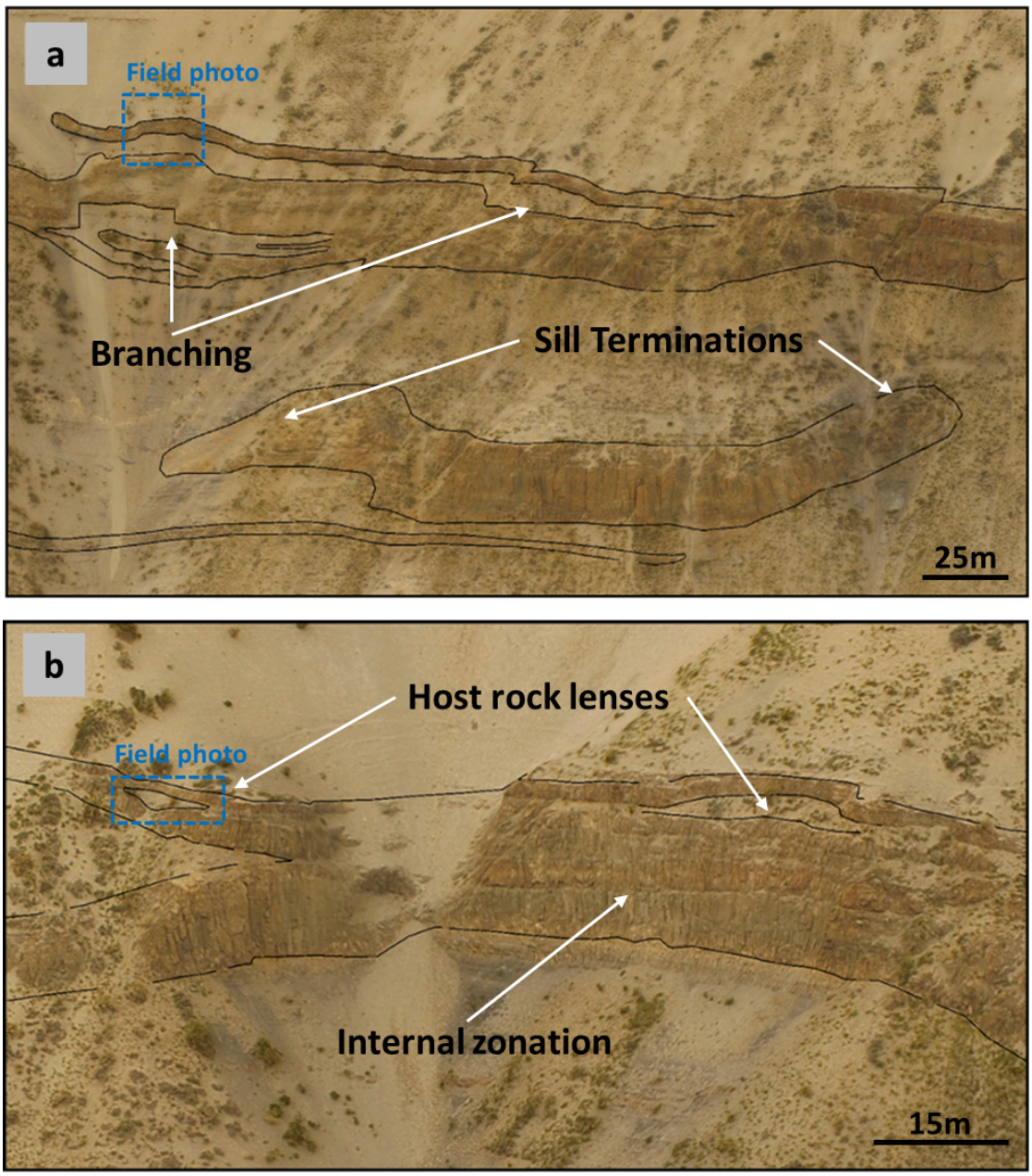

Figure 5.2: Detailed 3D view of the two areas indicated in figure 5.1, including complex sill geometries. Blue squares indicate locations of field photgraphs which support the interpretation. The photographs are shown in figure 5.3.

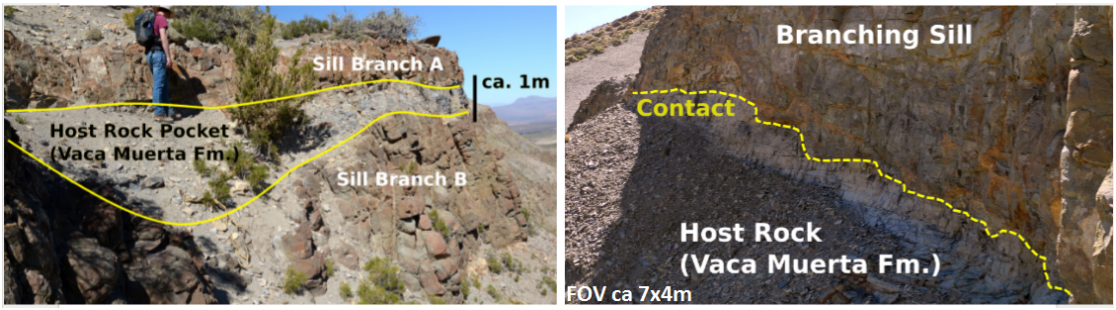

Figure 5.3: Field photographs of metre-scale geological details related to sills to support the interpretation of the virtual outcrop model, corresponding to areas highlighted in figure 5.2a (right) and 5.2b (left).

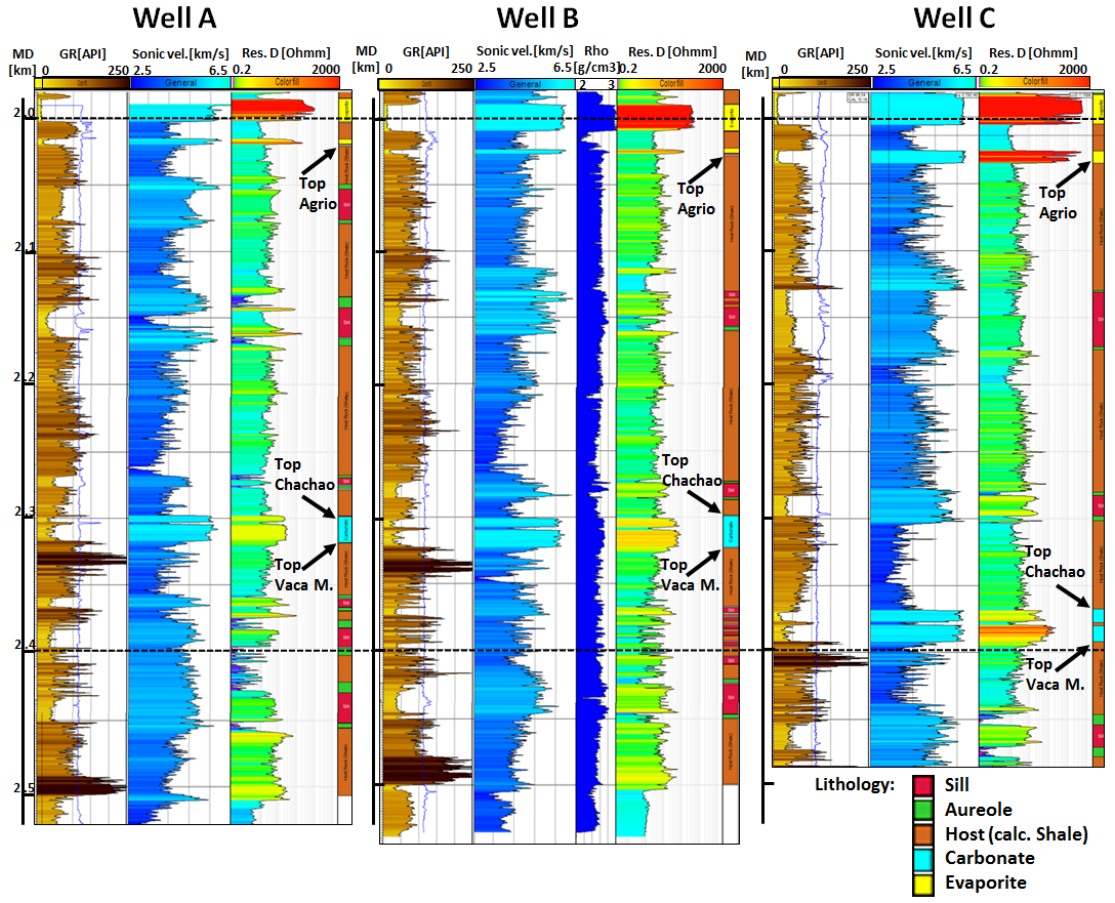

Figure 5.4: Three wells from the Los Cavaos oil field in Rio Grande Valley, including gamma ray (GR), sonic and restivity logs. Well B comprises a formation density log in addition. Important formation tops and lithology interpretation are indicated by colour code on the right side of each well. Data by courtesy of *YPF*.

5.2 Well Interpretation and Analysis

In the following, the results of well analysis from three wells, referred to as A, B, and C, will be presented. The wells are located in the Rio Grande Valley, just around 10 km east of El Manzano. Gamma ray (GR), caliper, sonic velocity, density and resistivity from the wells are shown in figure 5.4. A lithology interpretation based on pre-existing well tops and manual interpretation is given as a colour code on the right side of each well. Sedimentary units and rock types in the analysed depth intervals include Huitrin formation (evaporites), Agrio formation (organic rich shale), Chachao formation (micritic limestone) and Vaca Muerta formation (organic rich shale). Agrio and Vaca Muerta formations are marked as "host rock" in figure 5.4, as they are intruded by numerous andesitic sills. Within the target interval of $2000 - 2500m$ vertical depth, wells A, B and C intersect 6, 11 and 3 sills, respectively. The deepest intrusion of well B is a producing hydrocarbon reservoir. Sill thickness varies between 2-46 m with an average value of 15 m. In addition, there are several intervals dominated by stacked intrusives which have a cumulative thickness of 80-100 m. Only part of the log signatures of the sills comply with the typical characteristics of intrusives. Instead, they show a wide scatter of resistivity and sonic values, while GR is generally low. Some of the thicker sills show caliper anomalies which are often - but not always! - accompanied by a marked decrease in P-wave velocity and resistivity. While the host rock log signatures vary strongly in all properties, the localised limestone and evaportite layers are characterised by very high sonic and resistivity values, as well as very low GR. Note that this type of signature could be easily misinterpreted as intrusive rock.

Figure 5.5 gives a more quantitative view of the variations of the different log measurements for all lithologies. The displayed crossplots include P-wave velocity against reflectivity (figure 5.5a), GR (figure 5.5b), and depth (figure 5.5c). Resistivity values are very low in the contact aureole (largely <1 Ohm m) which is clearly separated from medium to high values of both host rock and sill(approx. 1-500 Ohm m). The limestone and evaporite intervals have very high resistivities of >1000 Ohm m. Host rock velocities are widely scattered for all resistivity values. A very broad trend towards higher velocities for increasing resistivity can be recognised. Sill velocities follow a similar, but much more clear trend, also increasing with larger resistivity values. Aureole velocities are generally in the same range as those of sills, but are evenly spread. Carbonates and evaporites do not indicate velocity change for changing resistivity. The velocity-GR crossplot indicates generally low GR values for sills (<75 API). Aureole and host rock mainly appear in a

different area of the crossplots than the sills, because they comprise larger GR values ranging between 50 and 200 API. Sill and aureole data do not seem to indicate any relation between GR and P-wave velocity. Host rock velocities, however, broadly trend towards lower velocities for increasing GR values. Carbonates and evaporites plot in a distinct field of very high velocity and very low GR. Plotting velocity versus depth yields the entire velocity range of each lithology for all depths. Therefore, the data do not seem to suggest depth dependency of velocity within the target interval.

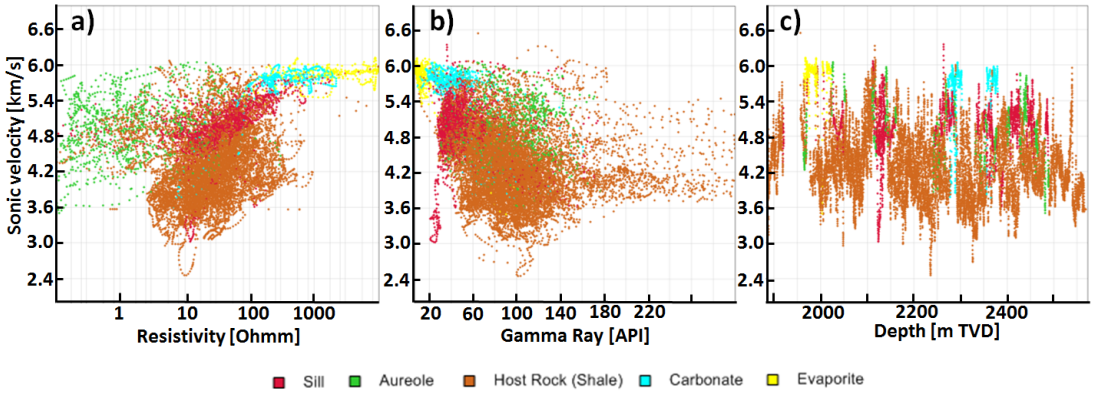

Figure 5.5: Crossplots of (a) sonic velocity against resistivity, (b) sonic velocity against gamma ray, and (c) sonic velocity against depth from the wells A,B and C shown in figure 5.4. The colours indicate lithology.

Figure 5.6 displays the frequency distribution of sonic velocities and density for all lithologies. Percentage values represent the relative percentage with respect the overall dataset (not within each lithology!). The shales (host rock) dominate the lithology compared to sills and localised carbonate and evaporite layers. Within the host rock measurements, approximately 85% of velocities lie between 3500-4900 m/s which is the interval that defines the P-wave velocity endmembers for later seismic modelling. The corresponding endmembers for sills define are defined by the interval of 4700-5500 m/s, which comprises around 80% of the measurements within the sills. The velocity distribution of the aureole is very similar to those measured in the sills. Carbonates and evaporites possess sonic velocities of 5500 m/s and above with only a small range. Density of shales, aureole and carbonates lie mostly between 2.4-2.6 g/cm^3, with an average of 2.55 g/cm^3. Sills show slightly higher values, yielding a range of mostly 2.5-2.8 g/cm^3 and an average of 2.7 g/cm^3. Evaporites show even higher density of 2.9-3.0 g/cm^3.

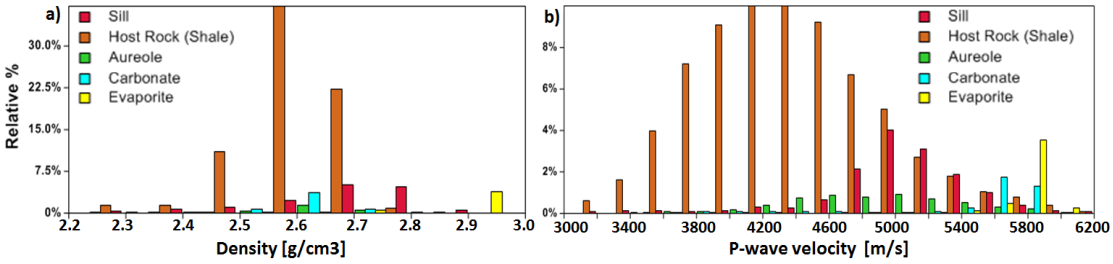

Figure 5.6: Histogram of (a) density and (b) sonic velocity from three wells in the Rio Grande Valley shown in figure 5.4. Note the overlap in velocity intervals for host rock and sills between approximately 4600-5000 m/s.

5.3 Seismic Modelling

The results of the seismic modelling study are best summarised by subdividing them into parameter sensitivity studies. Test parameters include signal frequency, seismic properties and angle of incidence. As the modelling was performed on real sill geometries, sill or layer thickness is not among the explicitly tested parameters, although the sills form wedge-like features in some cases. In combination with the point-spread function (PSF) plotted at scale, this allows assessment of the seismic resolution limit to a sufficient degree. For the seismic amplitudes in all synthetic seismic sections, note that the scaling is done automatically. The maximum of the absolute values is used to center the colour scale around zero, i.e. the colour scale reaches from 'minus maximum' to 'plus maximum'.

Effect of Signal Frequency on Resolution

Figure 5.7 displays full scale seismic images obtained by varying the dominant signal frequency. Tested frequencies were chosen to range from 20-40 Hz, which slightly exceeds 22-28 Hz obtained from 1D wavelet extraction of the real seismic cube. The choice of this frequency range allows assessment at which frequency significant improvement of the images can be expected. Following the same scheme, figure 5.8 presents two close-up views of imaged areas with sill stacks, branching and terminations. The images give an illustration of the geological detail which can be resolved in seismic data. To give an even better impression of resolution, the correctly scaled PSF corresponding to a point scatterer is plotted in each image. At 20 Hz (figure 5.7b), the extent of the correctly scaled PSF indicates that the resolution limit is than 50 m and consequently none of the single sills are resolved individually. Sill stacks are mostly merged into single reflectors of low amplitude compared to the higher frequency cases. The pattern for sill stacks is not consistent throughout the image. When few, relatively thick sill segments constitute

the sill stack, a single, continuous reflector results. Where several smaller sill branches and the sill geometry is irregular in the model (e.g. thickness variations, junctions or steps), the reflectors tend to be dimmer and more irregular. In some cases, sills that are unconnected in reality may appear as semi-connected reflectors with slight offset, somewhat similar to a fault structure. Examples for the observations described above are indicated by arrows in figure 5.7a. The close-up images in figure 5.8a further illustrates the relation between the seismic section together and the underlying sills and their reflectivity.

The intermediate case at 30 Hz (figure 5.7c) introduces more detail by reducing the resolution to approximately 35 m. The maximum thickness of individual sills in the model lies just below this value and these sills can be recognised by slight amplitude brightening. However they are still not resolved with a distinct top and bottom reflector. Stacks of few, thick sill branches are starting to split into individually detectable reflections. Stacks of several thinner sill branches are still appearing as single reflectors. However, their degree of irregularity increases, and top and base reflections are occasionally discontinuous, as indicated by an arrow in figure 5.7b and viewed in figure 5.8b. Where two unconnected branches converge or diverge, the associated reflections are dimming and may appear to join into, or spilt from a single stronger reflector.

The seismic image using a 40 Hz (figure 5.7d) wavelet restores the highest amount of detail from the input model. Sills of more than about 25 m are at tuning thickness and thus individually detectable or even resolved. Stacked sills are often distinguishable when the individual sills are sufficiently thick. Thin, stacked intrusives may not be directly detectable, but the resulting reflection pattern indicates a dense set of individual reflectors. A number of small scale details from the outcrop model like junctions, steps and intra-stack terminations are hinted by reflection geometries. This is illustrated well in figure 5.8c.

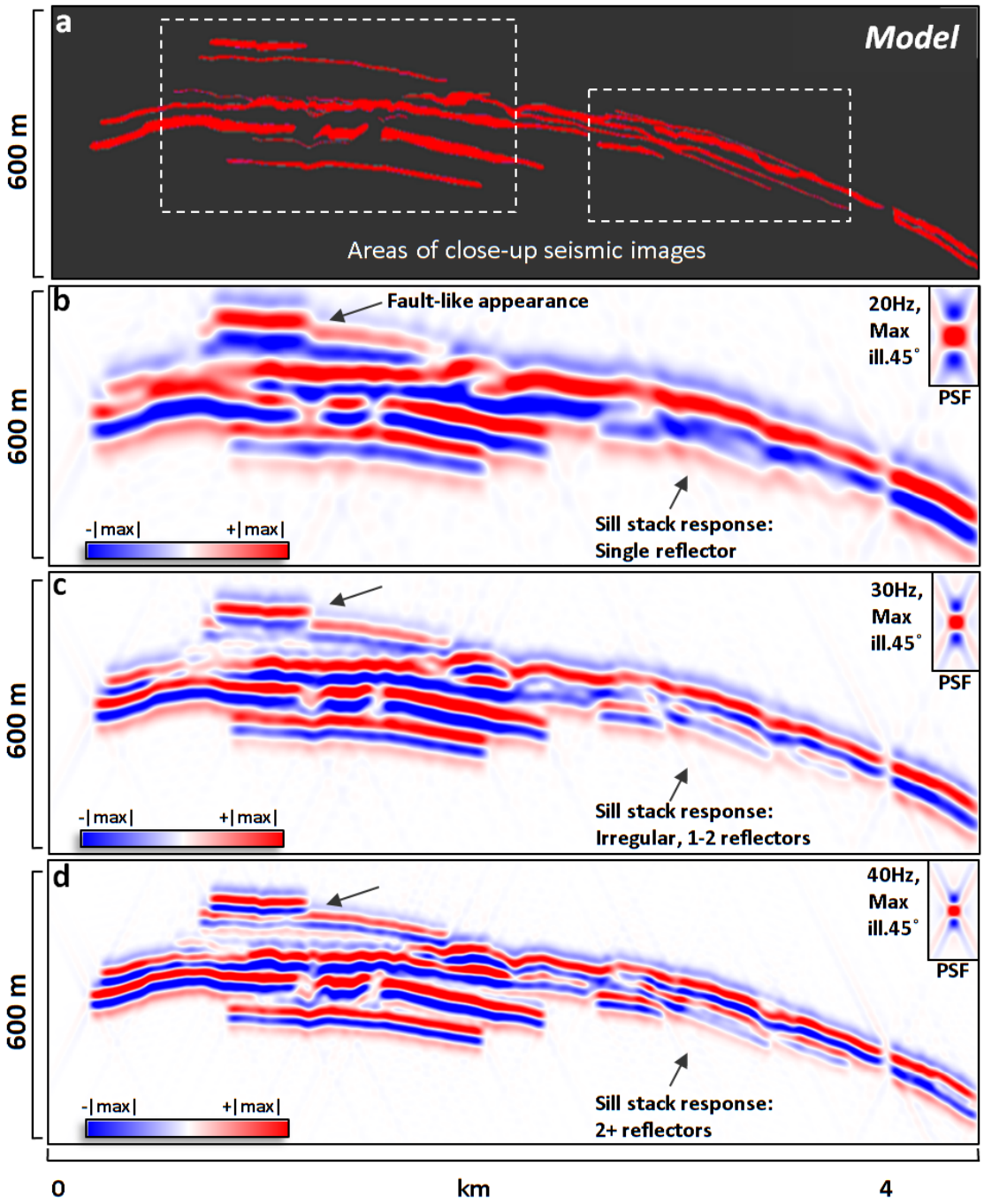

Figure 5.7: (a) Overview of the model of the El Manzano sill complex. (b-d) Zero-angle seismic images highlight the effect of signal frequency on seismic resolution. In the top right corner of each seismic image, the correctly scaled point-spread function (PSF) is plotted to provide a measure of seismic resolution. Close-ups of the seismic images containing the areas highlighted in (a) are shown in figure 5.8.

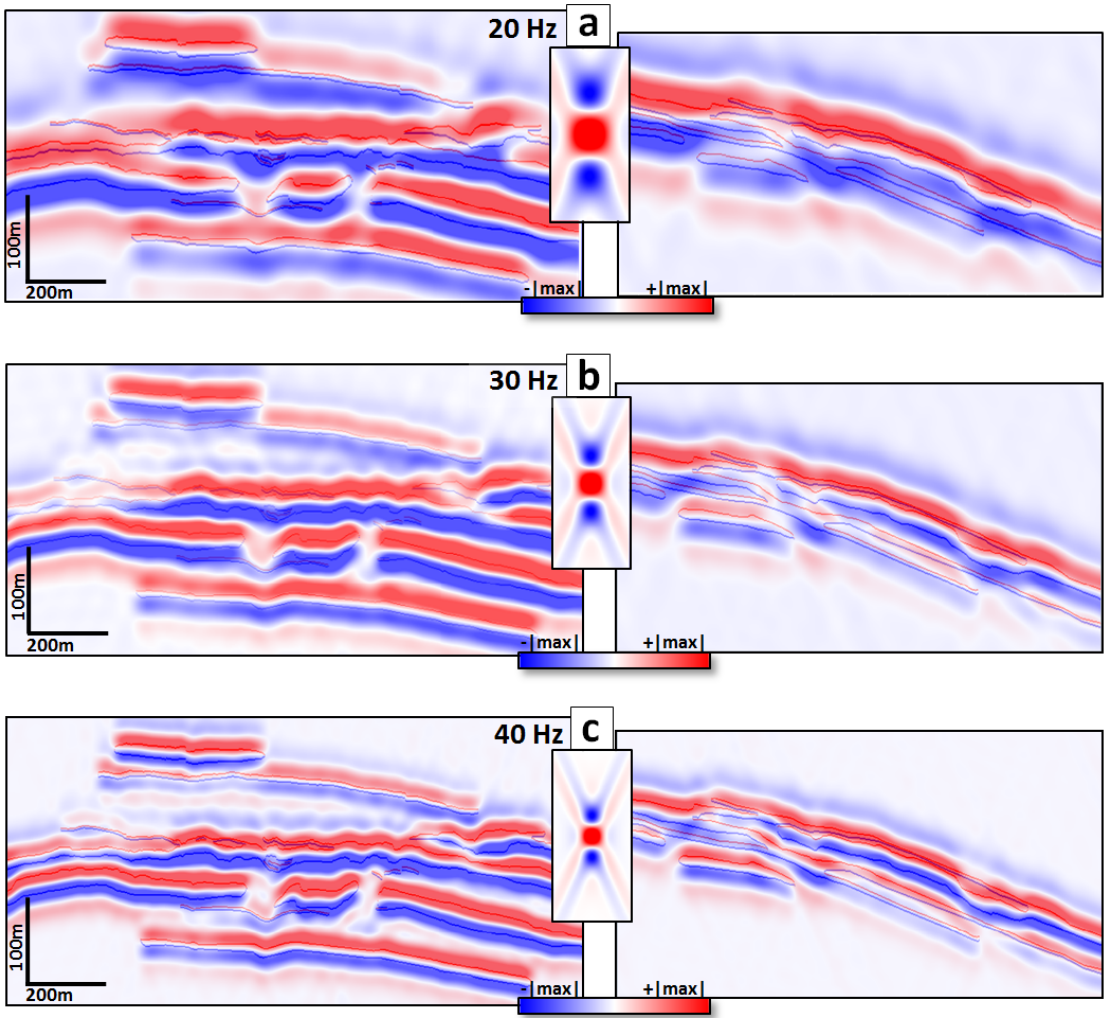

Figure 5.8: Close-up on the synthetic seismic section of two areas indicated in figure 5.7 with high level of geometrical complexity, imaged at 20-40 Hz (a-c). The scale is identical in left and right images, and the corresponding scaled point-spread function (PSF) is plotted in the center. Reflectivity is blended into the image, indicating increase or decrease in elastic impedance (red or blue, respectively).

Effect of Increasing Incident Angle and Seismic Property Variations

Another important factor which influences the reflection signature is the angle of incidence. The effect of varying incident angle can be examined if we know the illumination vector introduced in section 2.2, which comprises the information about the angle of incidence. Taking into account only source-receiver pairs with a certain angle of incidence and using the appropriate angle-dependent reflectivity allows us to examine the angle-dependency of the imaging. Figure 5.9 shows how the reflection geometry and amplitude is influenced by increasing the angle of incidence. Angles of 0°, 15° and 30° are considered for two different sets of acoustic impedance contrasts. In general, horizontal reflectors are more laterally smeared and vertical variations are smoothed at larger incident angles. However, the effect only becomes clear at 30° angle of incidence. The preservation of geological details is accordingly best for 0° angle of incidence and decreases in the images obtained at 15° and 30°. Some terminations and branches are merged at higher angles. Additionally the widening of horizontal partly merges thin horizontal reflectors into a single one. There are subtle differences in the PSF for each image in figure 5.9, but they are hard to catch when the PSF is plotted to scale. The size of the PSF slightly increases with increasing incident angle. The consequence is worse resolution, as can be seen when comparing figure 5.9a and e, or b and f, respectively.

Survey-dependent parameters such as angle of incidence and signal frequency have natural restrictions, but can be controlled within these constraints. A complex overburden may prevent certain subsurface areas to be illuminated for a given survey geometry, and attenuation of the seismic signal is dependent on the subsurface geology. On the other hand, detailed survey planning can be used to illuminate the subsurface target to the highest possible degree. In contrast, intrinsic elastic rock properties cannot be changed, but these properties also determine what seismic data can detect. Figure 5.9 presents the two elastic impedance endmembers defined by the results from well analysis (see section 5.2). For all angles, the low-contrast case on the left side produces amplitudes which are approximately 10 times lower in magnitude than those of the high-impedance case. The implies a detectability issue that will be discussed in chapter 6. It is important to note once more that the amplitude scales in all images are different due to automatic scaling to the absolute maximum for each image. This is unfortunate in this case, because if the scales for both endmembers were the same, the low impedance endmember would be extremely dim. The effect is emulated slightly by scaling amplitudes in figures 5.9a,c,e to 200% of the maximum value. Figures 5.9g and h indicate the significant difference in reflection amplitudes between the endmembers by displaying the amplitude variation

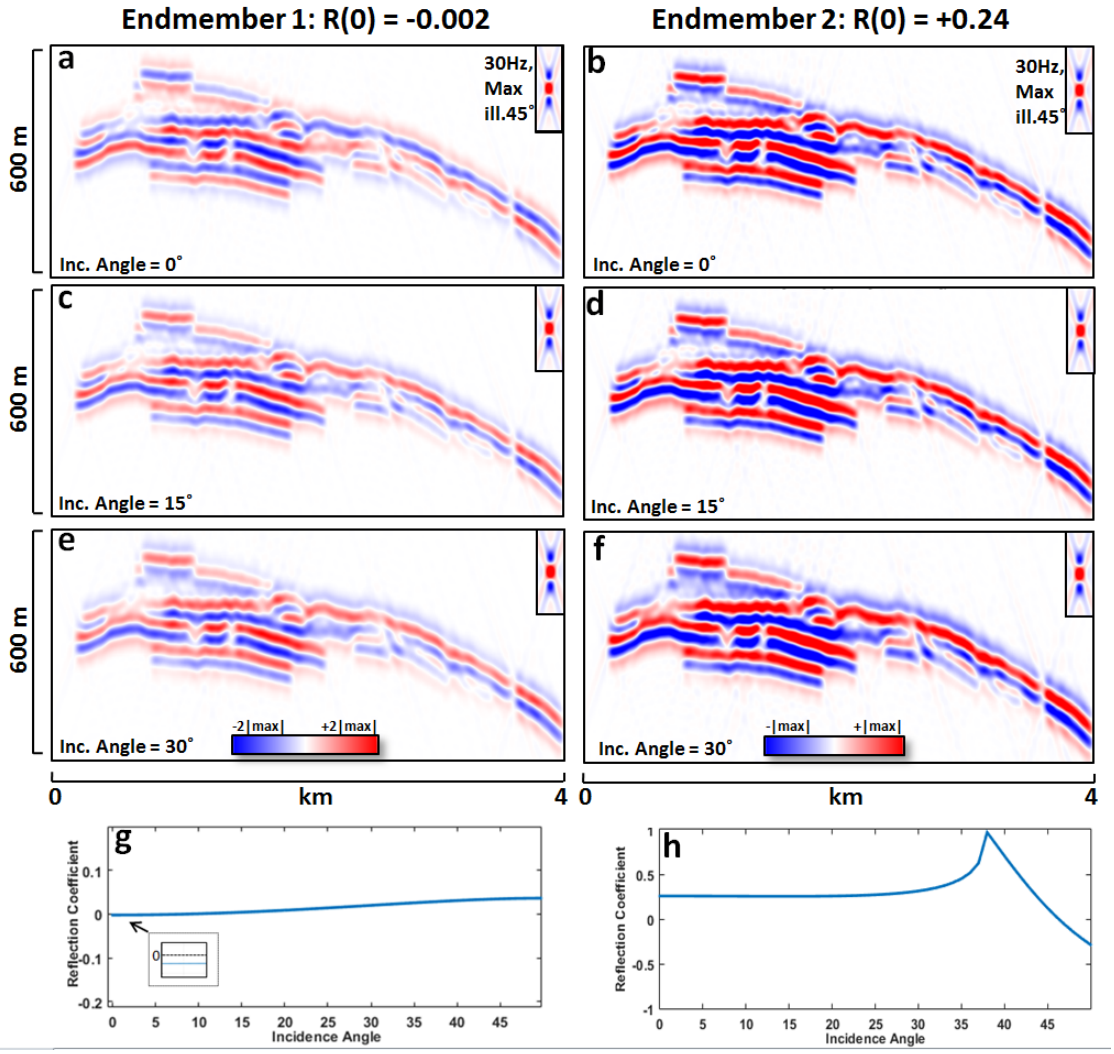

Figure 5.9: Influence of incident angle and impedance contrast on the synthetic seismic image. The images on the left (a,c,e) represent the endmember for low impedance contrast, the images on the right (b,d,f) represent the endmember for high impedance contrast. The first, second and third row correspond to an incident angle of 0°, 15° and 30°, respectively. Note that the amplitude scales are different, and amplitudes between the endmembers differ by a factor 10 or higher. The angle-dependent reflection coefficients for the low-contrast and high-contrast case are given in (g) and (h), respectively.

with angle (AVA). The angle-dependent behaviour differs markedly for the two cases. At vertical incidence (0°) the reflection coefficient of the low impedance contrast case is small and negative, giving a dim soft kick. At higher angles, we observe a phase change and subsequent increase in seismic amplitude in addition to the smoothing effects described above. On the other hand, reflection coefficients associated with the upper impedance

contrast endmember are generally positive, i.e. sill tops and bases appear as hard and soft responses, respectively. A minor increase of reflection amplitude is observed as incident angles increase. It is important to know that the critical angle in this case is reached at 38°, which poses restrictions on the angle range which can be used for seismic imaging of these structures. Note also that only illuminated reflectors can be imaged, regardless of the strength of the elastic impedance contrast.

5.4 Fracture Network Analysis

The results of fracture measurements and related fracture modelling following workflow B (chapter 4.2) provide the input for rock physics modelling. The presentation of these results is organised as follows: First, scanline line measurements obtained from digital models are shown (figure 5.10), followed by those obtained from fieldwork (figure 5.10). Each set of results is presented in the form of four plots: (1) A stereonet including all poles of fracture planes from all scanlines to get an overview of the main orientation pattern, (2) and (3) rose diagrams separated by scanlines taken in the upper and lower sill, respectively, as indicated in figure 4.4 in the description of workflow B. The rose plots are used to identify azimuth of preferentially oriented fracture sets. As the last step, (4) an azimuth histogram is shown which is the basis of defining relative percentage of each set with respect to the entire dataset. This histogram is subdivided into upper and lower sill to facilitate comparison with the rose diagrams, but the counting was done by using the entire dataset.

Following the structural data, results of fracture frequency (P10) and fracture density (P32) are given. Table 5.1 summarises the fracture sets with respect to mean orientation, P10, P32 and size. This table essentially yields the input parameters for the fracture modelling. In addition, figure 5.12 illustrates the variability of fracture frequency in each zone (top, center and base sill) as well as for vertical scanlines in the upper and lower sill, respectively (compare figure 4.4 in the workflow description). Note that there is no corresponding plot for scanlines from fieldwork because of the small number of scanlines taken during fieldwork. Table 5.2 summarises the results of fracture modelling, which in turn provide the input parameters for rock physics modelling.

Fractures from Virtual Scanlines

The results of fracture measurements obtained from virtual scanlines are summarised in figure 5.10. The stereoplot in figure 5.10a comprises the poles of all 1245 fracture planes.

Vertical and subvertical fractures clearly dominate, as indicated by a girdle of poles near the circumference. Although fracture planes for all strike directions are present, maximum fracture normal density occurs at dip and azimuth of 83° and 201°, respectively. This is also qualitatively visible and indicates a dominant set striking roughly E-W. In addition to the steeply dipping fracture planes, the data show a subhorizontal set of approximately 120° azimuth which is parallel to the sill top as well as local structural dip. Although the data have not been not dip corrected, it is obvious that such a correction would lead to nearly vertical fracture planes in all directions and one horizontal fracture set. Only a few oblique planes can be observed.

The rose plots (figure 5.10b) show fracture strike of all fractures within lower and upper sill, respectively, and indicate a very similar pattern. However, the fractures measured in the upper sill indicate a slight clockwise rotation. The E-W striking set ('set 1') which is visible in the stereoplot also dominates the strike statistic, confirming the observations made above. Furthermore, two areas of elevated strike counts stand out from the generally strong background 'noise' of random strike orientation: (1) A N-S striking set ('set 2') which is more prominent in the upper than in the lower sill, and (2) a NE-SW striking set which is also more pronounced in the upper sill. The situation is generally less clear than for set 1.

The fracture azimuth histogram (fig. 5.10c) highlights specific complementary observations made above. Notably, the subhorizontal fracture set now plots separately at around 120 degrees, and the subhorizontal fractures have a broader distribution in the upper sill compared to the lower sill. This histogram also forms the basis for quantification of all fracture sets in terms of fracture frequency.

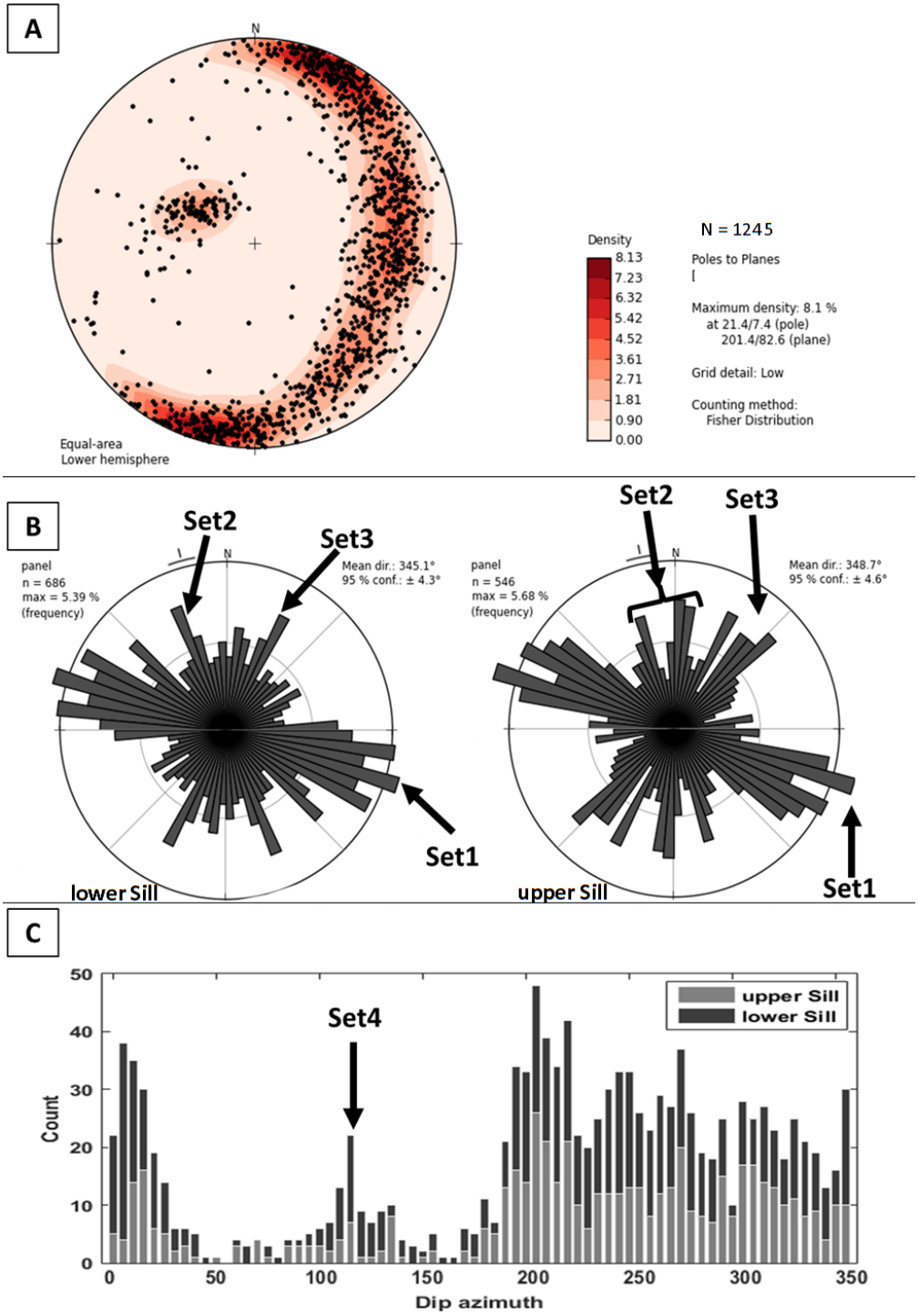

Figure 5.10: Results from analysis of structural measuments obtained from virtual scanlines. (a) Steoreoplot comprising poles of more than 1200 fracture planes, showing clear dominance of subvertical fractures as well as some subhorizontal fractures. (b) Rose histograms providing fracture strike for lower sill (left) and upper sill (right), with indicated fracture sets. (c) Stacked histogram of fracture azimuths from both sills to support identification and discrimination of sets.

Fractures from Field-based Scanlines

The results of fracture measurements obtained from scanline measurements in the field are illustrated in figure 5.11. Subvertical fractures clearly dominate the stereonet plot in figure 5.11a which comprises the poles of all 296 measured fracture planes. This is indicated by a girdle of poles near the circumference. However, a marked concentration of poles at around 0° and 180° is visible. Consequently, maximum fracture normal density occurs at dip and azimuth of 83° and 184°, respectively, indicating a dominant fracture set striking E-W. In addition to the steeply dipping fracture planes, a few poles suggest a subhorizontal set of approximately 100° azimuth which is parallel to the sill top as well as local structural dip. The data have not been not dip corrected, but it is obvious that such a correction would lead to nearly vertical fracture planes in all directions and potentially one horizontal fracture set. Only very few planes with intermediate dip angles are observed.

The rose plots (figure 5.11b) show fracture strike of all fractures measured during fieldwork divided into lower and upper sill, respectively. Although the overall pattern is roughly similar to the stereoplot, the sills exhibit some differences. The E-W striking set ('set 1m', 'm' for 'manual scanline') dominates the strike statistic in the both sills. There are two other strike directions with elevated strike counts, however, the intensity of their expression varies between the sills: (1) A roughly N-S striking set ('set 2m') which is much more prominent in the upper than in the lower sill, and (2) a NE-SW striking set ('set 3m') which is in fact much more pronounced in the upper sill (nearly as strong as set 1m). From the distribution of fracture strikes, the number of randomly oriented fractures seems to be small.

The fracture azimuth histogram (figure 5.11c) forms the basis for quantification of all fracture sets in terms of fracture frequency and highlights complements observations made above. The subhorizontal fracture set now plots separately, but somewhat scattered between 90-130° at around 120 degrees, and the subhorizontal fractures have a broader distribution in the upper sill compared to the lower sill.

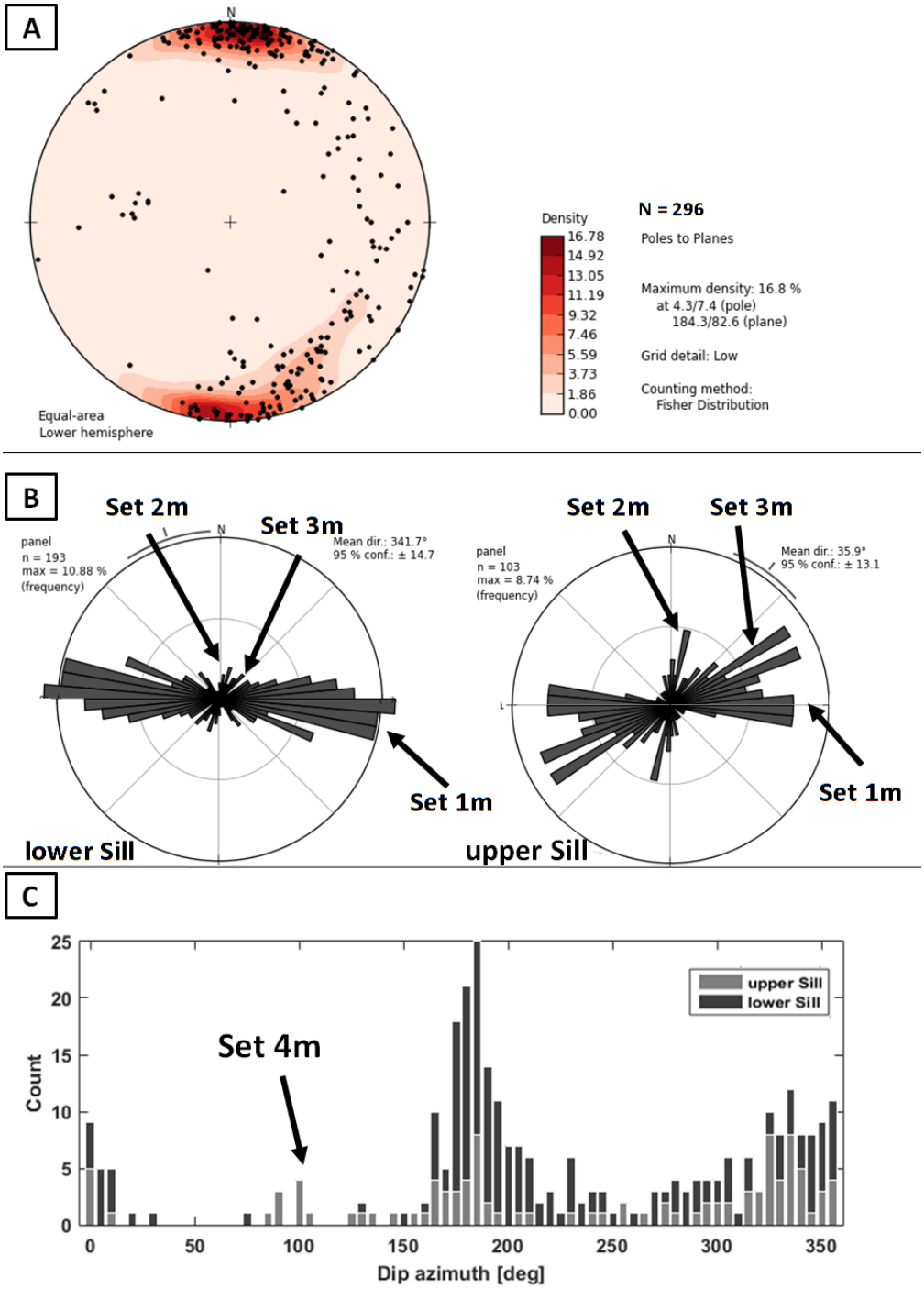

Figure 5.11: Results from analysis of structural measuments obtained from scanlines during fieldwork. (a) Steoreoplot comprising poles of 296 fracture planes, showing clear dominance of subvertical fractures as well as some subhorizontal fractures. (b) Rose histograms providing fracture strike for lower sill (left) and upper sill (right) with indicated fracture sets. (c) Stacked histogram of fracture azimuths from both sills to support identification and discrimination of sets.

Fracture frequency and DFN Modelling

Fracture frequency boxplots resulting from virtual scanlines are shown in figure 5.12 to illustrate variability of the measurements in the different zones of the sill that were defined during scanline measurements. Fracture frequency varies markedly within the sills and is generally higher in horizontal scanlines compared to vertical ones. The average value for all horizontal scanlines is 1.34 fractures per metre, while the values range between 0.8 and 2.5 fractures per metre. Fracture frequency in vertical scanlines is consistently below 0.6 and averages at 0.3 fractures per metre. Table 5.1 summarises relevant fracture statistics and displays input parameters for DFN modelling. It appears that P32 values have similar values for sets 1,2,4 and random fractures which range between 0.37-0.48 m^2/m^3. Set 3 is less dense (0.12 m^2/m^3). Additionally, table 5.1 provides analogous results extracted from analysis of field data.

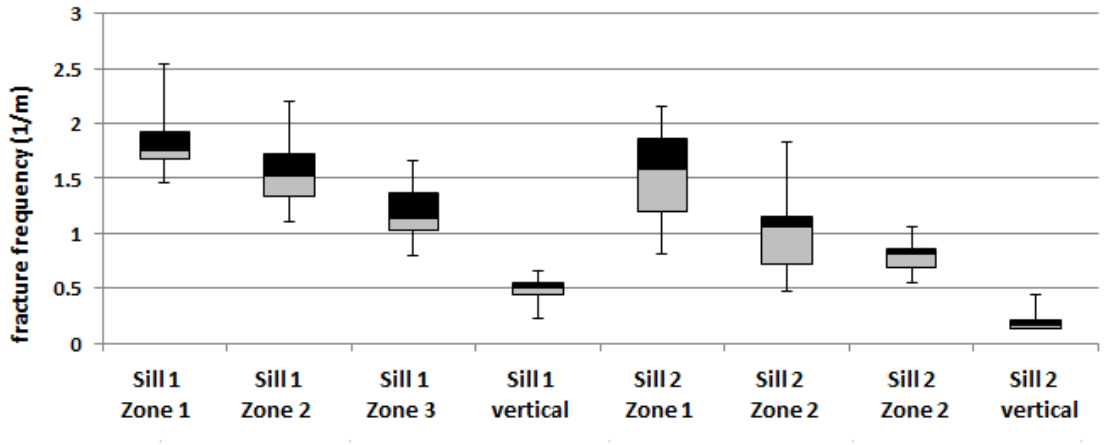

Figure 5.12: Box-whisker plot of fracture frequency (P10) based on virtual scanlines, for horizontal (zone 1-3) and vertical scanlines. The plots display variations of P10 by giving minimum, lower quartile (grey part of the box), upper quartile (black part), and maximum. Note that manual scanlines are not represented due to too small number of scanlines.

Results of subsequent fracture modelling using parameters presented above are listed in table 5.2. In VOM based modelling between 3452 and 7339 discrete fractures of 10 m length are created for each set, yielding a seismic crack density range of 0.2 and 0.63. Assuming input aperture of 3 mm, associated cumulative fracture porosity is calculated to be 0.6±0.5%. The field based modelling yields between roughly 2-6 million fractures per set. This results in seismic crack densities of 0.1-0.33 per set, and associated cumulative fracture porosity of 3.2±0.4%.

Table 5.1: Summary of fracture measurements, giving average orientation, frequency measures, length and aperture derived from VOM and core data (upper sets 1-5). Similar analysis from outcrop and core data are given as the lower sets 1 m-5 m.

from VOM	Set#	mean Az./Dip	P10[1/m]	Cp3	P32[m^2/m^3]	length[m]	aperture[mm]***
	1	201°/83°	0.45	1	0.45	10	3
	2	270°/70°	0.23	2	0.46	10	3
	3	319°/74°	0.12	1	0.12	10	3
	4*	118°/29°	0.37	1	0.37	10	3
	5	random	0.48	1	0.48	10	3
from Outcrop**	1m	201°/83°	2.48	1	2.48	1	3
	2m	270°/70°	1.28	2	2.56	1	3
	3m	319°/74°	0.68	1	0.68	1	3
	4m	118°/29°	0.45	4	1.8	1	3
	5m	random	2.7	1	2.7	1	3

* based on vertical fractures only
** manual scanlines, only fractures of approx. 1m length considered
*** maximum aperture value from core data

Table 5.2: Results of digital fracture network (DFN) modelling for fracture sets obtained from virtual outcrop model (left) and field-based fracture sets (right), including seismic crack density and fracture porosity.

length/aperture = 10m/3mm					length/aperture = 1m/3mm				
Set#	fracture count	e	ϕ avg	ϕ stddev	Set#	fracture count	e	ϕ avg	ϕ stddev
1	6531	0.57	0.001	0.001	1m	5686311	0.29	0.008	0.001
2	6956	0.60	0.002	0.001	2m	5989160	0.31	0.008	0.001
3	2437	0.20	0.001	0.001	3m	1963028	0.10	0.003	0.001
4	3452	0.49	0.001	0.002	4m	3341637	0.17	0.005	0.001
5	7339	-	0.002	0.001	5m	6400120	-	0.009	0.001
∑	26715	1.86	0.006	0.005	∑	23380256	0.88	0.032	0.004

5.5 Rock Physics Modelling

Exploratory Rock Physics Modelling was conducted to investigate and quantify the effect of fratures on elastic rock properties and seismic velocities. The modelling yields results for (1) an isotropic model with randomly oriented fractures, and (2) anisotropic models that contain fracture sets of preferred orientations superimposed on an isotropic background.

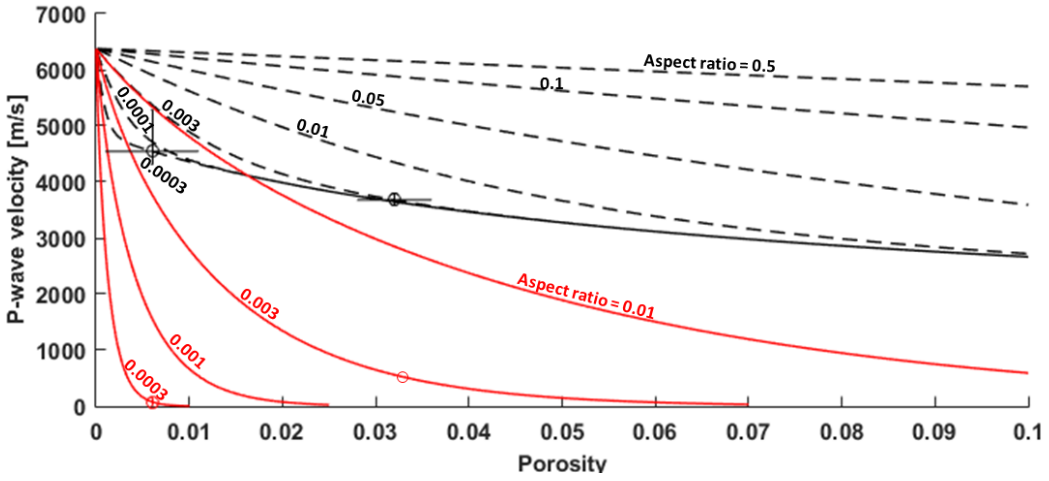

Figure 5.13: Isotropic P-wave velocities based on rock physics modelling using differential effective medium (DEM) theory. Curves show the velocity-porosity trend for a variety of aspect ratios for water-saturated (black) and dry/empty cracks (red). The data points represent results for porosity values that were calculated from fracture modelling for different scenarios (shown in table 5.2). Horizontal and vertical errorbars indicate standard deviations for porosity values and associated velocity variations.

Figure 5.13 illustrates the resulting P-wave velocity from isotropic modelling for a single population of dry or fluid filled fractures with varying aspect ratio. As a first notice, DEM theory remains computationally stable at all porosities. The black and red lines indicate the porosity-velocity trend for each aspect ratio (indicated by small numbers). In general, fractures with a smaller aspect ratio have a stronger effect on the P-wave velocity. The curves for the largest aspect ratios (> 0.1) show a nearly linear behaviour, while thin cracks with small aspect ratios follow an exponential curve. An interesting note is that predictions for aspect ratios of 0.003 and smaller, the velocity functions converge. This is related to the fact that the respective dry moduli (red curves) and, therefore, wave velocities are approaching zero at certain values. The dry moduli, in turn, are used to model the effect of fluid substitution according to Gassmann's theory.

For fully water saturated cracks with given crack porosity, choice of aspect ratio has a strong influence on the modelled velocities with a generally stronger velocity reduction for smaller aspect ratios.

The result for the 10 m long fractures considered in the DFN fracture modelling was a fracture porosity of 0.6% at an aspect ratio of 0.0003. Isotropic rock physic modelling predicts a velocity to of abount 4600 m/s. On the other hand, for cracks of 1 m length and 3 mm opening, we find a P-wave velocity of around 3900 m/s at 3.2% fracture porosity. However, the data points for the same porosity values of both cases are much smaller than 1000 m/s. This means that the underlying elastic moduli of the dry rock have nearly vanished. Therefore, it is already important to notice already at this point that these results are unlikely to represent the real behaviour of the rock.

The directional velocity patterns resulting from the four anisotropic rock physics models (8 cases) introduced in chapter 4.2 are illustrated in figures 5.14-5.17. A summary of the results in terms of quantitative anisotropy parameters in table 5.3. All cases with only one preferred fracture direction are fully described by three anisotropy parameters, while orthotropic media require seven of these parameters (Tsvankin, 1997). Since the available seismic field data are exclusively P-wave reflection seismic surveys, the focus in this study is on P-wave anisotropy effects. However, the S-wave parameters will be briefly presented for the sake of completeness. In figures 5.14-5.17, the simplest case including only one open set (set 1) is shown on the left side, while all sets are open in the figures displayed on the right side. Note that detailed guidance for how to read the direction velocity plots is given in section 4.2. Let us, for each model, first look at the corresponding figure to identify the general directional velocity pattern. Thereafter, turn to table 5.3 for a description of the resulting fracture compliances and anisotropy parameters. The theoretical background of these parameters is described in chapter 2.4.

In modelling case 1 (figure 5.14a), a pattern of fast direction in the fracture plane and slow direction across the plane is visible. However, the slowest direction is actually at 45° instead of expected 90° to the fracture plane. Note that is a known phenomenon when fluid pressure is not fully equilibrated due to isolation of pores with respect to fluid flow (Thomsen, 1995). Resulting velocities range between 5250 m/s in the slow horizontal direction (90° incident angle) and around 5500 m/s for both vertical and fastest horizontal direction. Velocities are high within 10° deviation from the fracture plane. However, they quickly drop and approach the slow velocities at more than 30°

Table 5.3: Results from rock physics modelling case 1-8, including maximum values for normal and tangential fracture compliance of a single set, as well as seismic anisotropy paramters for up to orthorhombic media. In addition, vertical P-wave velocity is given for comparison to sonic logs.

Case No.	$E_{t,max}$	$E_{n,max}$	$\varepsilon^{(1)}$	$\delta^{(1)}$	$\gamma^{(1)}$	$\varepsilon^{(2)}$	$\delta^{(2)}$	$\gamma^{(2)}$	$\delta^{(3)}$	vertical v_p[km/s]
1	1.123	0.042	-	-	-	-0.01	-0.16	-0.26	-	5.48
2	1.186	0.098	-0.01	-0.13	-0.17	-0.04	-0.06	-0.12	-0.07	4.77
3	0.306	0.013	-	-	-	0	-0.11	-0.12	-	6.18
4	0.322	0.021	-0.03	-0.04	-0.07	0	-0.11	-0.1	-0.14	5.88
5	0.302	0.126	-	-	-	-0.07	-0.18	-0.16	-	5.83
6	0.312	0.259	-0.12	-0.15	-0.1	-0.08	-0.19	-0.11	-0.17	5.03
7	0.321	0.387	-	-	-	-0.13	-0.19	-0.12	-	5.15
8	0.332	0.39	-0.14	0.15	-0.09	-0.1	-0.17	-0.09	-0.16	4.61

deviation from the fracture plane. With all fractures open in modelling case 2(figure 5.14b), the pattern becomes more complex. There are two fast horizontal directions (azimuth 0° and 90°) with unequal velocities of approximately 4650 m/s and 4800 m/s, respectively. There are also two slow horizontal directions. They exhibit the same wave velocity of approximately 4550 m/s. The highest velocity in this model case is 4850 m/s and applies to waves with normal incident angle (vertical). Additionally, for 90 ° azimuth, velocities show a local minimum of roughly 4650 at 45° incident angle.

Regarding the associated fracture compliances, the maximum tangential fracture compliances E_t for a single fracture set are 1.12 and 1.19, respectively. In contrast, normal fracture compliance E_n for models 1 and 2 are more than 10 times smaller. The anisotropy parameters for P-wave variations ($\varepsilon_{1,2}$) are small (1-4%). In contrast, the S-wave anisotropy ($\gamma_{1,2}$) reaches significantly larger values of up to 26%.

Reduction of fracture density in model cases 3 and 4 (figure 5.15) produces the same relative patterns for directional P-wave velocities as model 1. However, since the crack density is reduced by 75%, velocities are now much higher. In the case of one fracture set (figure 5.15a), the slowest horizontal velocity (90° incident angle) is now 5980 m/s, while the fastest velocity (in the crack plane, 90° azimuth) is 6150 m/s. When all fracture sets are included (case 4, figure 5.15b) two slow horizontal directions occur at 40° and 130°, respectively. The corresponding slow velocity is approximately 5600 m/s. In addition, two fast horizontal directions exist at 0° and 90° azimuth with around 5700 m/s and 5800 m/s, respectively. The fastest velocity of 5880 m/s is reached in the vertical direction.

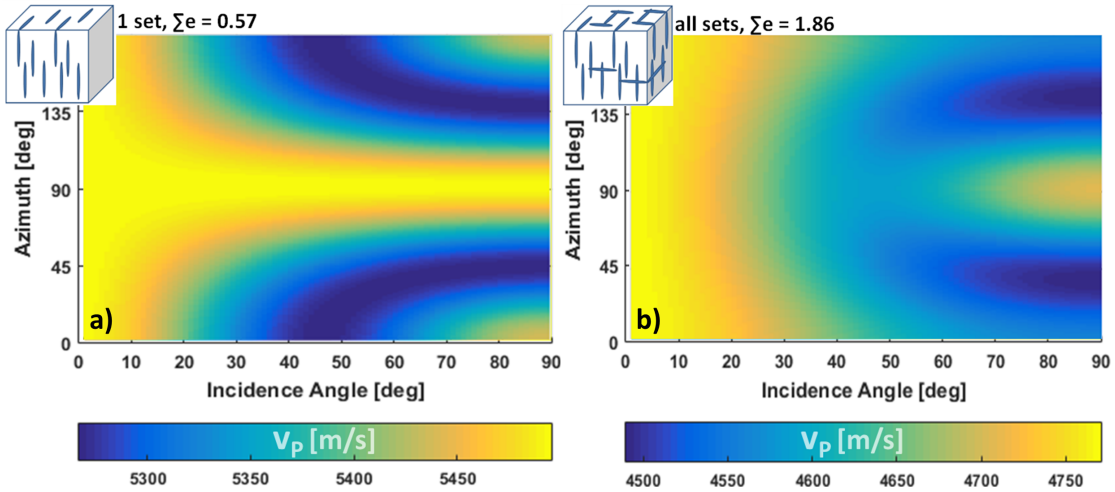

Figure 5.14: Anisotropic P-wave velocities for all azimuths and incident angles obtained from rock physics modelling cases 1,2 (full fracture density). A sketch of the underlying rock model is shown in the top left corner of each image. Results for case 1 (set 1 open) are displayed on the left side, results for case 2 (all sets open) are shown on the right side.

The quantitative parameters derived from the model also differ markedly in magnitude. The maximum tangential and normal fracture compliances are markedly reduced compared to cases 1 and 2. Here, the modelling yields values of 0.31 and 0.32 for E_t, and 0.01 and 0.02 for E_n for the modelling cases 3 and 4, respectively. P-wave anisotropy parameters $\varepsilon_{1,2}$ are vanishing or very small (0-3%). The other anisotropy parameters are reduced, but still show values between 4% and 14%.

In modelling cases 5 and 6, a second population of cracks with higher aspect ratio is added. This has a strong effect on the resulting velocity and the associated anisotropy. Including two aligned fracture sets of the same orientation (case 5, figure 5.16a) now gives a typical pattern of transverse isotropy with a horizontal symmetry axis (HTI). This means that slow and fast horizontal directions are arranged orthogonally normal and parallel to the fracture plane, respectively. The values for fast and slow directions now range between 5820 m/s and 5350 m/s, respectively. When all fracture sets are implemented (case 6, figure 5.16b), two slow horizontal directions at 45° and 135° azimuth are observed. Both comprise an identical P-wave velocity of around 4350 m/s. The two corresponding fast directions show P-wave velocities of 4700 m/s at 0/180° azimuth, and 4400 m/s at 90° azimuth. Such a pattern commonly results from an orthotropic medium. Note that the second of the fast directions exceeds the slow directions by only 50 m/s. In addition, there

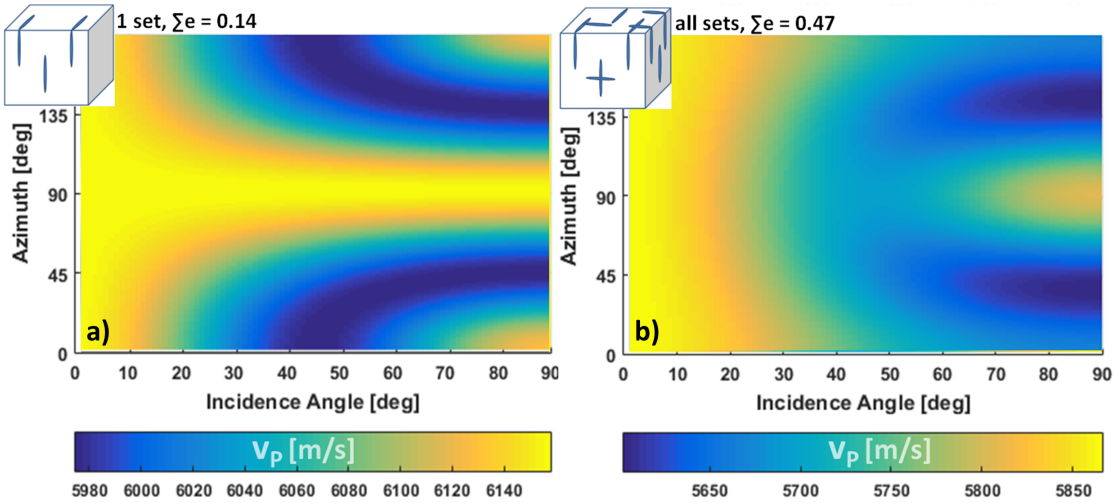

Figure 5.15: Anisotropic P-wave velocities for all azimuths and incident angles obtained from rock physics modelling cases 3,4 (reduced fracture density). A sketch of the underlying rock model is shown in the top left corner of each image. Results for case 3 (set 1 open) are displayed on the left side, results for case 4 (all sets open) are shown on the right side.

is a steady increase of P-wave velocity from horizontal to vertical propagation direction. The maximum velocity of approximately 5000 m/s is reached at vertical angle of incidence.

While tangential fracture compliances remain of similar magnitude compared to the previous models, table 5.3 indicates that the introduction of pore shape variety particularly affects normal fracture compliances. Compared to model 3 and 4, E_n has increased by around one magnitude to values of 0.13 and 0.26 in models 5 and 6, respectively. This has a profound effect on P-wave anisotropy which now reaches values of 7% and 7%-12% for $\varepsilon_{1,2}$ in cases 5 and 6, respectively. S-wave anisotropy parameters also generally increase to values between 7%-19%. However, noted that it is in particular $\delta_{1,2}$ that shows a major increase by a factor 2-4. The parameter $\delta_{1,2}$ is responsible for near-vertical P-wave variations, as well as SV-wave anisotropy.

Looking at modelling cases 7 and 8 shown in figure 5.17, adding a small amount of vuggy porosity leads to similar effects as in models 5 and 6. A single aligned fracture set (case 7, figure 5.17a) yields HTI behaviour, i.e. orthogonally arranged slow and fast horizontal directions normal and parallel to the fracture plane, respectively. Fast and slow directions show velocities of around 5150 m/s and 4500 m/s, respectively. Including all fracture sets (case 8, figure 5.17b) produces an orthotropic pattern. Two slow horizontal directions

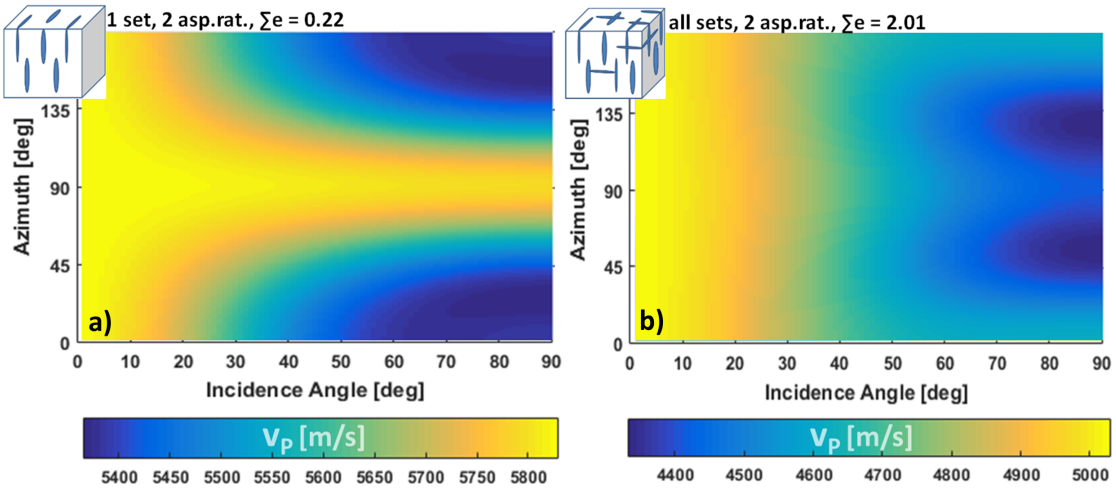

Figure 5.16: Anisotropic P-wave velocities for all azimuths and incident angles obtained from rock physics modelling cases 5,6 (reduced fracture density, varying crack aspect ratio). A sketch of the underlying rock model is shown in the top left corner of each image. Results for case 5 (set 1 open) are displayed on the left side, results for case 6 (all sets open) are shown on the right side.

are found at approximately 45° and 135° azimuth, with P-wave velocities of about 3900 m/s. In the corresponding two fast horizontal directions, P-waves travel at a velocity of 4250 m/s at 0/180° azimuth, and just above 3900 m/s at 90° azimuth. The slower of the fast directions has just around 20 m/s higher velocity than the slow direction, making it essentially impossible to distinguish them. The P-wave velocity is continuously increasing from horizontal to vertical propagation direction. The highest velocities of approximately 4600 m/s occur an incident angle of 0°.

Despite the qualitative similarity in directional velocity patterns between cases 5,6 and cases 7,8, the quantitative parameters in table 5.3 indicate some marked differences. Maximum tangential fracture compliances remain nearly unchanged at 0.32 and 0.33, but the maximum value for normal fracture compliance increases by a factor of 1.5-3. Note that cases 7 and 8 are the only ones where E_n exceeds E_n, and where maximum E_n is essentially equal for both fracture models. The effect of this rock model on anisotropy in comparison to cases 5 and 6 is a slight increase in P-wave anisotropy $\varepsilon_{1,2}$ to 13% in model 7, and 10-14% in model 8. Contrary to that, S-wave anisotropy parameters only show minor changes in comparison to model 5,6.

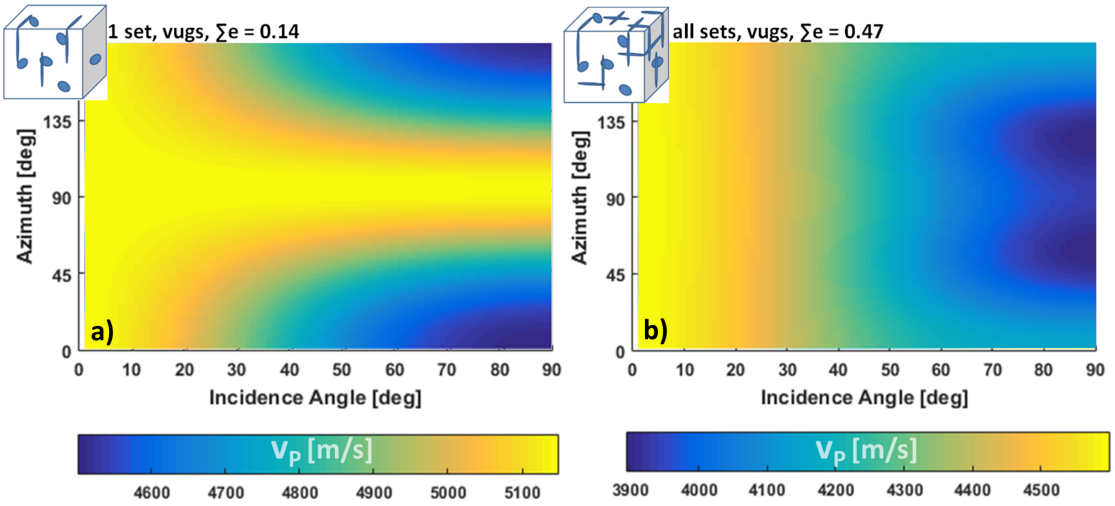

Figure 5.17: Anisotropic P-wave velocities for all azimuths and incident angles obtained from rock physics modelling cases 7,8 (reduced fracture density, 5% vuggy porosity). A sketch of the underlying rock model is shown in the top left corner of each image. Results for case 7 (set 1 open) are displayed on the left side, results for case 8 (all sets open) are shown on the right side.

6 Interpretation and Discussion

In the following interpretation and critical evaluation of the results, the key research goals of this study will be addressed individually. First, an interpretation and discussion of the modelled seismic response of the El Manzano sill complex will be given with focus on the sensitivity to investigated parameters such as signal frequency content and seismic parameters. Thereafter, the combined core and field-based approach to the characterisation of the fracture network will be discussed, including the effect of fractures on seismic wave propagation. Finally, the discussion will focus on the integration of seismic and subseismic scale observations. Well data play an important role for the interpretation of observations on both scales, as well as for linking the two. Therefore, the relevant well data will be included in the discussion of the individual parts rather than devoting a separate chapter to them. In addition, examples from Rio Grande Valley seismic exploration will be discussed to demonstrate the use of direct field analogues for the interpretation of subsurface data.

6.1 Seismic Modelling of the El Manzano Sill Complex

Model Building Workflow

Before interpreting the actual prestack depth-migrated (PSDM) seismic sections obtained from seismic modelling, it is necessary to briefly discuss the models obtained from the virtual outcrop model (VOM). Individual sill thicknesses between 1-30 m as well as sill stacks of cumulative thickness of up to 80-100 m are observed in the El Manzano VOM (figure 5.1). Metre-scale details like sill branching and terminations are common features and can be interpreted by combining high-resolution VOMs and field observations (figures 5.2, 5.3). Following workflow A presented in methods section 4.1, it is possible to include these features into gridded geomodels without significant loss of detail and within a viable time frame and budget. This demonstrates that the combination of modern 3D mapping techniques, such as structure-from-motion (SfM), with commonly used software packages can provide realistic models, including geological features far below the limit of seismic resolution. The ability to analyse the influence of these features on seismic

images facilitates an assessment of the limits of seismic interpretation beyond more common approaches using idealised layer shapes such as thinning wedges (e.g. Magee et al., 2015; Planke et al., 2014). In the context of volcanic sill complexes, this means that intrusions that are subseismic in scale may now be included in seismic modelling studies in a more realistic manner. The importance of this finding is highlighted by the fact that other authors have found that up to 88% of the intrusions found in wells within sill complexes might be below the vertical seismic resolution limit (Schofield et al., 2015). However, they used simplistic 1D convolution to predict the seismic response which cannot accommodate for lateral resolution effects or diffractions stemming from complex, small-scale sill geometries. 2D/3D convolution used in this work does include these effects and is therefore suitable to be applied to highly detailed geological models.

Seismic Property Variations from Well Data

In addition to the geometric detail, well data from Rio Grande Valley shows that seismic properties such as P-wave velocity and density vary significantly for both host rock and intrusions in the target intervals (figure 5.6). P-wave variations, in particular, are not only large in absolute terms (main intervals 4700-5500 m/s and 3500-4900 m/s for sill and host rock, respectively), but the velocity ranges also overlap. This creates the realistic possibility of cases where intrusions and host rock have very similar seismic properties. As a consequence, seismic impedance contrast variations that must be considered for seismic modelling range from high contrasts to almost none. This result highlights the necessity of assessing seismic properties with care when predicting the seismic response of sills. In the case of the andesitic intrusions in Rio Grande Valley, velocities lie in the lower range of typical sill velocities obtained by other authors (Skogly, 1998; Planke et al., 2005), but particularly host rock velocities are much more variable and potentially higher compared to other studies (Magee et al., 2015; Planke et al., 2014). The data presented here indicates that boundaries between host rock and sills can, but do not necessarily have to, exhibit high impedance contrasts, as it is often suggested in existing literature (Planke et al., 2005; Magee et al., 2015; Planke et al., 2014).

Seismic Modelling

Varying the seismic signal frequency and comparing the resulting seismic images demonstrates that the amount of geological detail resolved in seismics can vary significantly within only 20 Hz variations (figures 5.7, 5.8). The El Manzano sill complex comprises sill stacks and numerous sills with thicknesses at, or just below, the seismic resolution limit -

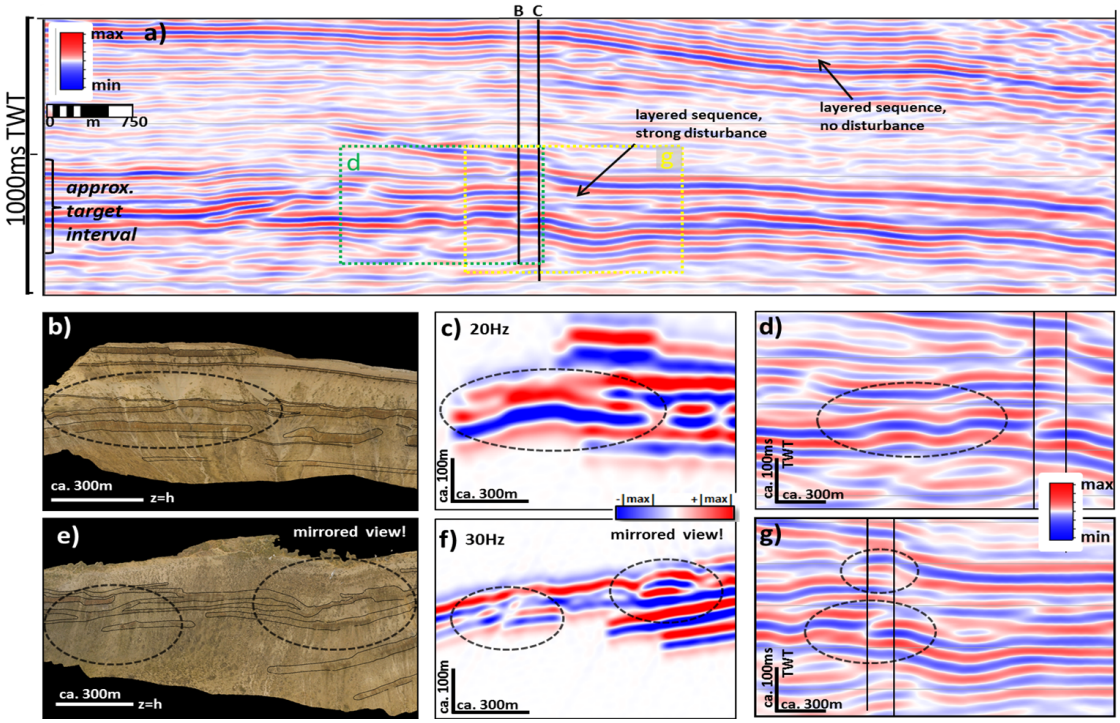

Figure 6.1: Comparison of 3D seismic line from Rio Grande Valley with virtual outcrop model and synthetic seismic. (a) Overview of prestack-time migrated (PSTM) seismic section including the target interval comprising hydrocarbon-brearing intrusions as well as parts of the overburden. Locations of wells B and C are indicated. (b) Example of a branching sill in the El Manzano VOM, (c) its modelled seismic expression (20 Hz), and (d) a similar looking reflection pattern from real seismics. (e) Example of a sill stack including sill terminations, (f) their modelled seismic expressions (30 Hz), and (g) similar looking reflection pattern from real seismics. Data by courtesy of *YPF*.

both in the classical sense of 1/4 wavelength and in the more comprehensive sense of 2D extent of the point-spread function (PSF). Although at the lowest frequency considered (20 Hz), none of the sills is clearly resolved. The tuned reflection packages that are visible result from interference of the individual sill responses. This interference pattern seems to be closely related to the underlying geometry of the sill complex, such as converging and diverging branches or spacing between stacked sills. Note the modelling also contains diffracted energy. This may contribute to a better representation of geological details in the images compared to what one would expect from classical 'rule-of-thumb' resolution analysis. In fact, existing data from Rio Grande Valley are currently re-evaluated using diffraction detection algorithms (*YPF*, pers.comm.). At higher frequencies, we observe that seismic reflections from sill stacks begin to capture individual sills and do react to small scale features of some metres thickness. The comparison of figures

5.7b-d suggests that already relatively small increases in signal frequency can lead to significant improvement in terms of geological detail that is represented in seismic sections. In addition, it may be possible to identify volcanic sill complexes and perhaps justify approximate interpretations of sill geometries below seismic resolution even without resolving individual sills. Note that when tuned reflections are interpreted as top and bottom of individual sills, and the peak is used to interpret the contact, the intrusions are likely to be overestimated in thickness (compare e.g. real intrusion thickness to resulting seismic reflections in figure 5.8).

Figure 6.1 illustrates the relation between the observations from outcrop and modelled seismic sections and 3D pre-stack time migrated (PSTM) seismic data of the target interval in the Los Cavaos oil field. Particular attention is given to comparison specific waveforms arising from the geometry of outcropping sills. One must exercise caution when comparing PSTM (time-domain) to PSDM (depth-domain) data, but since the overburden exhibits little structural complexity in this case, the changes from PSDM to PSTM are assumed to have minor impact. The target interval consists of a heavily intruded sequence of shale layers and localised carbonates and evaporites. Comparing this to a lithologically similar layered sequence without intrusions at a higher stratigraphic level gives a good impression of the strong disturbance caused by the sills. This can be generally described as a change in seismic facies. Similarities between the detailed reflection patterns of synthetic and real seismics are striking and can potentially be attributed to diverging sill branches ("x-shapes", figure 6.1b-d) or variations in sill spacing and termination within sill stacks ("steps" and "branches", figure 6.1e-g). Therefore, it can be concluded that, if high seismic data quality and a good knowledge of expected geological features are available, small scale seismic interpretations may be justifiable. This knowledge could, for instance, be provided by detailed studies of outcrop analogues. On the other hand, individual sills are unlikely to be fully resolved, inhibiting mapping of single intrusions. The lower threshold of features influencing the seismic waveforms is dependent on the signal frequency. The limit of detection, which is around 1/10 of the dominant wavelength (Planke et al., 2005), should be a good approximation that fits with most of the observations in this study. However, there are several sills that clearly influence the seismic model which are less than 10 m thick (e.g. figure 6.1b), corresponding to less than 1/15 of the dominant wavelength.

Another important factor in seismic exploration is related to the incident angle of the seismic waves on a reflecting surface, as well as the elastic (or seismic) impedance

contrast across that surface. Not only does resolution decrease for increasing angles of incidence, but also the amplitude of the reflected waves (expressed by reflection coefficients) changes with incident angles (see figure 5.9). The angle-dependent reflection coefficients are in turn controlled by the elastic properties of the rocks, and more specifically, the property contrasts at the reflecting surface.

Figure 5.9 shows that an increase of the incident angle may lead to loss of small scale details in the seismic image due to lateral smoothing. Thus, whenever possible, comparing images obtained at different angles of incidence may help to distinguish between smoothing effects and actual layer geometries. In other words, if small-angle images exhibit different seismic reflection patterns compared to high-angle images, it could be beneficial to pay particular attention to small-angle images. However, conducting detailed analysis of the underlying PSF based on survey parameters and overburden (where applicable) can help in making the correct choice. For instance, in the case of the El Manzano sill complex and the seismic line displayed in figure 6.1, dipping reflectors are unlikely to be an issue.

The elastic impedance contrasts between intrusions and host rock in the Rio Grande Valley vary significantly and may lead to very different seismic responses in each case. This is shown by the analysis of P-wave velocity and density obtained from well logs (figure 5.6) and the corresponding reflectivity endmembers shown in figure 5.9a,c,e (weak contrast) and 5.9b,d,f (strong contrast), respectively. In addition to the large difference in amplitude between the two endmembers (up to factor 100), sills may even represent a slight reduction in impedance contrast and thus appear as a soft kick at small angles. In this specific case (endmember 1), there would also be a phase shift at around 10° incident angle. This finding has several implications for the treatment of intrusions in seismic exploration: (1) A strong focus on strong reflection events when mapping intrusions is common (e.g. Planke et al., 2014; Schofield et al., 2015) but may lead to an underestimation of the number of intrusions and the associated volume. This could, for instance, occur when relatively high host rock velocities around an intrusion cause low amplitude reflections. Further complication regarding the amplitude is added because stacks of thin intrusions may be either dim due to destructive interference effects, or bright due to constructive interference effects ("tuning" in 1D terminology). (2) When there is potential host rock impedance reaching values that may be equal to those of sills, the intrusions show very weak reflections which could become nearly invisible, or masked in interference. However, the reflections may become stronger at larger offsets. In addition, phase shifts may occur

and thus stacking needs to be carried out with care. In a case similar to endmember 1 in figure 5.9, stacking would essentially eliminate the reflections due to destructive interference of the small and large angle responses. (3) If available, images obtained by using different angle ranges may provide insight about lateral variations of impedance contrasts. If, for instance, both impedance endmembers from figure 5.9 occur in the seismic dataset, the sills may cause similar reflection geometries, but have quite different seismic responses.

Despite the high level of geometrical detail with which the El Manzano sill complex could be modelled, there is still significant room for improvement. The host rock is modelled as a homogeneous background medium. Fieldwork observations and especially well logs (figure 5.4) indicate that this is not the case. Following the same procedures described in workflow A (section 4.1), VOMs could be used to add detailed host rock layer geometries to the model, potentially also including contact aureoles. Using simple 1D convolution, Magee et al. (2015) demonstrated that reflections from layered host rocks may interfere with reflections stemming from sills and thus affect the overall seismic response. Additionally, the localised carbonate and evaporite layers of the Huitrin and Cachao formations are not included in the model of the El Manzano sill complex. However, these layers are known to be present at the top and in the center of the target depth (figure 1.2) and represent layers of high seismic velocity and thus impedance (figure 5.6). Because they could be easily confused with intrusions, a model including these layers may be a helpful addition for interpreters. This could, for instance, be combined with combination of seismic sill facies analysis to relate the seismic response to the different lithologies, as discussed by Planke et al. (2005).

6.2 Rock Physics Modelling based on Fracture Network Characterisation

In this section of the discussion, an examination and discussion of the characterisation of the fracture network is provided. In addition, the rock physics modelling of the effect of fractures on elastic parameters and P-wave velocities will be discussed. Similar to the previous chapter, the section will begin with a short review of the underlying workflow B (described in section 4.2).

Workflow for Virtual Fracture Measurements

Compared to the more extensive large scale surveys of the entire El Manzano sill complex, the high-resolution SfM survey for fracture measurements could be conducted in only one day. The data processing requires also approximately one day. However, extensive manual picking and counting of fractures in the VOM along virtual scanlines is quite tedious and represents by far the most time consuming part of the work prior to modelling. Even the relatively localised scanline survey conducted during this investigation took more than a week. Compared to manual scanlines measured in the field, this is still a major improvement, because virtual scanlines yield significantly more measurements and therefore more robust statistics in a shorter period of time. Importantly, Casini et al. (2016) follow a similar workflow and demonstrate that manual scanlines are still essential for quality control. Further improvements regarding acquisition efficiency may be achieved by using automated fracture detection techniques in combination with fracture logs (Casini et al., 2016).

Characteristics of the Fracture Network

The results of manual and virtual fracture measurements along predefined scanlines are presented in figures 5.10 and 5.11. Both results suggest largely similar orientation distributions, including dominance of vertical and subvertical fractures and four identifiable fracture sets of similar orientation (three (sub)vertical, one subhorizontal). However, the data obtained from virtual scanlines indicates a much larger portion of subvertical fractures with random orientation, and stronger representation of the more N-S striking fracture sets 2 and 3. This may be a consequence of (1) the larger dataset (4-5 times more fracture measurements), (2) a wider spread of outcrop, and thus scanline trend orientations, (3) different fracture scales represented in the virtual and the field-based scanlines (approximately 10 m vs. 1 m, respectively), or a combination of those explanations. In particular, outcrop orientation has been shown to have a significant influence on measured fracture orientation patterns (Senger et al., 2015). Thus, minimising this outcrop bias by removing accessibility issues and instead using virtual outcrops is an important step towards more robust datasets.

A possible explanation for the observed orientation pattern of the fractures could be a combination of randomly oriented cooling joints and tectonic overprint. Although the underlying fracturing mechanisms have not been thoroughly investigated and are thus speculative, a tectonic origin of set 1 is strongly suggested, because it is oriented

with the main direction of Andean compression. The N-S and NE-SW striking sets present are more difficult to explain, since they are oriented roughly orthogonal to the the compression. However, they may be related to local tension, since the outcrop is part of the Sierra Azul anticline. The occurrence on fracture sets with various orientations is an important observation with respect to the oil fields in Rio Grande Valley. Here, the main direction of fluid flow is highly variable and may be related to changes of predominant fracture orientation (*YPF*, pers. comm.). Faulting and folding due to inversion of Mesozoic graben systems is commonly observed and may be used as an explanation (Manceda and Figueroa, 1995). Therefore, the fracture patterns from El Manzano may represent a realistic analogue to the fracture system of subsurface reservoirs.

The average fracture frequency (P10) indicate small variations between the two sills as well as the zones defined in figure 4.4. In particular, the subhorizontal, contact parallel scanlines (zones 1-3) are largely consistent. Vertical scanlines exhibit markedly smaller fracture frequencies compared to vertical ones. This implies less horizontal fractures. In addition, the upper sill yields slightly lower P10 values, implying less frequent fractures. However, this can probably be attributed to outcrop quality, since the upper sill shows a higher degree of erosion, making it more difficult to measure fracture planes from a VOM. This effect of outcrop quality on P10 values has also been described by Casini et al. (2016). Accordingly, we conclude that, given sufficient outcrop quality, virtual scanlines can provide a useful tool to obtain the input parameters needed for fracture modelling using discrete fracture networks (DFN). After orientation correction, another noteworthy observation is that fracture density (P32) is in fact of similar magnitude for the random fractures and sets 1 and 2 (table 5.1). Smaller values for P32 are obtained for the subvertical set 3 and subhorizontal set 4. Assuming all fracture sets might be present and at least partly open at depth in specific geological situations (near faults or folds), this finding should be kept in mind when performing fracture modelling or attempting fracture detection using seismics. The reason is that geophysical algorithms often assume a single set of aligned fractures. This question will be discussed below in more detail.

The results from DFN modelling (table 5.2) provide the number of discrete fractures within the model volume, resulting seismic crack density e (defined in equation 2.4, section 2.4), as well as fracture porosity associated with each fracture set. Around 27000 large fractures (squares of 10 m side length) are implemented in the model in order to create the fracture density (P32) required by the input parameters obtained from virtual scanlines. On the other hand, more than 2.3 million smaller fractures result from

field-based measurements of smaller (1 m) fractures. Yet, the resulting seismic crack density of the few long fractures is about twice the value of the many small fractures. This is a good example of the ambiguity of the seismic crack density parameter, which tells us nothing about the number or size of fractures (Barton, 2007). In addition, the definition of seismic crack density includes the average fracture radius (equation 2.4) - this may be problematic, because the fracture count often follows a power law behaviour which does not have an average. Therefore, a meaningful approach can be to combine geophysical and geological quantities (e.g. P32) to constrain fracture networks with respect to geometry and abundance of fractures. Such an integrated approach may help to investigate whether there is a fracture scale that dominates the seismic signature.
In contrast to the seismic crack density, the fracture porosity predicted using core-based fracture aperture of 3 mm is 5 times higher for the smaller fractures, yielding a cumulative value of 3.2%. However, the robustness of the obtained values needs to be discussed.

Fracture count is only sensitive to values of P32 and length, which can be controlled to a relatively high degree from combined field and virtual fracture measurements. Fracture porosity, on the other hand, is strongly influenced by choice of aperture, be it a constant value or a user-defined relationship between length and aperture. Since it is inherently difficult to relate fracture length to aperture, especially for fractures exceeding the size of cores, the choice of aperture introduces a high degree of uncertainty. In a test case (not shown here), the aperture of the 1 m long fractures was reduced to 0.5 mm, and porosity went down by a factor of 10. Therefore, estimated fracture porosity values should be treated with care. Since no fracture analysis on the micro-scale was conducted, the influence of smaller fractures is not included in the model. When interpreting and discussion fracture effects on seismic modelling, this must be taken into account. If the trend that smaller fractures yield smaller seismic crack densities continues at the micro-scale, one may assume that large joints will dominate the seismic response. However, although this would fit the observation of high initial oil production rates due to large joints, any comments on the influence of microfractures remain speculation. In any case, the crack density and porosity values obtained from DFN modelling represent the upper boundary, since all fractures are assumed to be open. This consideration is incorporated in the rock physics models presented below by strongly reducing the number of fractures in the model (compare section 4.2 for description of the models).

Rock Physics Modelling

For the interpretation and discussion of the rock physics modelling performed for this study, attention will first be directed towards the isotropic modelling using differential medium theory (DEM) based on fracture porosity from DFN modelling. Thereafter, the anisotropic modelling cases introduced in section 4.2 will be interpreted and discussed. The results will be compared to velocities obtained from well logs, results from azimuthal AVA studies (AVAz, compare sections 2.4 and 4.2) from Rio Grande Valley, as well as their geological justification. In addition, some technical issues are discussed and compared to the findings of other authors.

Figure 5.13 gives results of combined isotropic DEM and Gassmann modelling for varying porosity, assuming a variety of crack aspect ratios. Because of the very small aspect ratios, the predicted velocities drop quickly. The porosity-velocity pairs using fracture porosity and aspect ratios from DFN results are in the lower range (4000-4500 m/s) of the sonic velocities measured in the sills (compare figure 5.6). On first sight, this seems in reasonable agreement. However, there are a number of reasons why the approach of modelling the entire fracture network as a single set of identically shaped fractures is probably not only geologically unrealistic, but also unreliable. First, we need to remember that if Gassmann's theory is applied, the calculations are based on the dry modulus on the rock (corresponding velocities are red lines in figure 5.13). Although DEM does not collapse computationally, the velocity of the dry rock (and thus the bulk and shear moduli) are close to zero at the data points from fracture modelling. Bearing this in mind, one may question if the final results for the saturated rock have a good physical justification. Second, the control on length-aperture relationships, which is crucial for porosity determination, is poorly constrained by field and core measurements. Figure 5.13 displays that, especially for thin cracks, small porosity variations have a strong effect on the predicted P-wave velocities. Therefore, a much better control on the overall pore space geometry and associated porosity is needed.

Berge et al. (1992) demonstrate that DEM is capable of inverting for pore shapes of highly porous and fractured basalts and constraining expected porosity. However, they used 8 different aspect ratios between 0.001 and 0.5, illustrating that meaningful rock physics models for volcanic rocks require to take a high degree of complexity into account. This level of detail is difficult to provide and would require a thorough investigation of pore geometries on various scales. Xu and Payne (2009) also propose to rather use rock physics models comprising mixtures of round, stiff and thin, soft pores to characterise

rocks with complex pore space geometries. Even though isotropic rock physics modelling may be feasible if the rock model is sufficiently well known, it is not necessarily suitable for the fractured sills which are investigated here. Based on the results from fracture measurements and modelling (figures 5.10, 5.11, table 5.1), it appears reasonable to assume that the fracture orientation is not isotropic, i.e. randomly oriented. The data show a roughly orthogonal pattern of vertical sets striking E-W, N-S as well as a horizontal set. Set 5 is indeed characterised by random strike directions, however, dips are almost exclusively subvertical. This provides justification to perform anisotropic rock physics modelling to develop a better understanding of directional velocity variations due to preferentially oriented sets of fractures.

In the case of Rio Grande Valley, modelling anisotropic effects of fractures on seismic

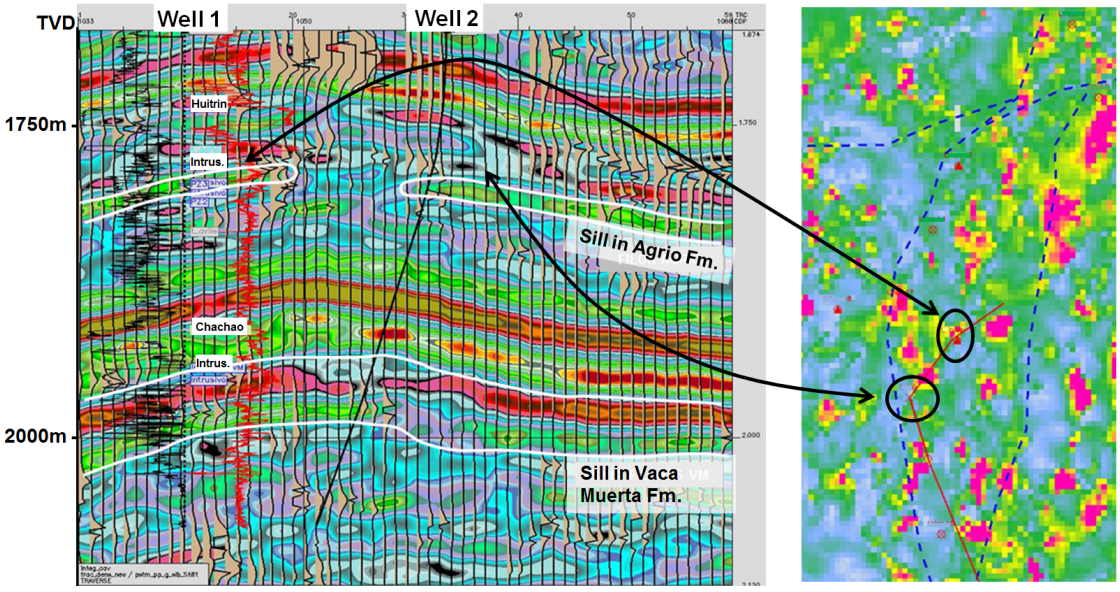

Figure 6.2: Examples of a section view (a) and map view (b) from an AVAz study targeted at volcanic reservoirs in Rio Grande Valley. Warm colours indicate AVAz anomalies which are interpreted as the result of high degree of fracturing. Colder colours represent areas of little azimuthal variations in their seismic response. Note that the colour scale is relative, and thus no quantitative statements on fracture intensity can be made. White lines indicate intrusives, blue dotted lines indicate faults, the logs shown in (a) are gamma ray (black) and resistivity (red). Image by courtesy of *YPF*.

wave propagation has a practical motivation: Fractures are assumed to provide porosity and very high permeability, and are thus critical to production and exploration efforts. Apart from field observations, the cross-plot analysis of well data also indicates that fractures may play a major role in providing fluid pathways. Figure 5.5 indicates a

narrow trend towards higher P-wave velocity for higher resistivity, while velocity-GR and velocity-depth crossplots do not show the same behaviour. Increased permeability allows for better conduction of electric currents, resistivity commonly drops if an interconnected, water saturated pore space is present. In this case, we can use this argument to advocate for fractures as the explanation, as an increase of fracturing would simultaneously cause a drop in sonic velocity. It is noteworthy that the carbonate beds show a nearly constant relation between velocity and resistivity, potentially indicating a lower degree of fracturing.

Recently, an azimuthal AVA (AVAz) study was carried out using 3D seismic data from one of the fields. The reason is that seismic velocity anisotropy due to fractures is assumed to be the main reason for azimuthal variations of reflection pattern. This is a major step towards a link of seismic scale exploration and the petrophysical properties of the rock at the mesoscale or microscale. This link will be discussed in more detail in the discussion of the integration of observation of various scales. Figure 6.2 shows a section as well as a map view of the AVAz anomaly attribute in a selected area of Rio Grande Valley. One can immediately recognise the high lateral and vertical variability of the AVAz response. The upper, thinner sills in Agrio formation 6.2a create mild anomalies (green colour), while the lower sill in Vaca Muerta formation indicates a stronger anomaly (red). However, the anomalies vary significantly within the intrusions, and there are other areas that also comprise anomalies. Bearing in mind these initial observations, let us turn to the anisotropic P-wave velocities obtained from rock physics models for sills presented in figures 5.14-5.17 in order to interpret and discuss potential links between models, sonic well logs, and AVAz anomalies.

All rock physics modelling cases include random fracture porosity (using values of set 5) plus either one or all of the other fracture sets. All fractures are water saturated and communicate with respect to fluid flow to allow Gassmann-type fluid effects. Cases 1 and 2 (figure 5.14) include the fracture densities directly obtained from DFN modelling. Vertical velocities range between 4750- 5500 m/s, which is comparable to values from sonic logs from vertical wells. However, given the extremely high degree of fracturing, P-wave anisotropy represented by $\varepsilon_{1,2}$ are surprisingly low (1-4%), and high velocities are observed in the horizontal direction normal to the fracture plane for case 1. This is a known phenomenon for fluid filled fractures, if pore pressure equilibration is absent or very limited (Thomsen, 1995) and usually deemed unrealistic for seismic waves. In addition, tangential fracture compliances exhibit values larger than 1. This is in conflict with laboratory measurements which show that this parameter hardly

exceeds in-situ values of 0.2, or 0.7 in dry or partially liquid-saturated rocks under laboratory conditions (Hsu and Schoenberg, 1993; Rasolofosaon et al., 2000). Another critique of these cases is that all fractures from the field would be open at depth, which is highly unlikely because of pressure-related closure of fractures as well frequent occurrence sealed fracture, for instance with calcite (Witte et al. (2012), *YPF*, pers. comm.).

Cases 3 and 4 are taking some of the remarks made above into account by reducing the seismic crack density by 75%. Note that this value is an estimate and rather meant to illustrate the consequences than provide perfectly accurate results. Qualitatively, the resulting patterns do not change (figure 5.15), but P-wave anisotropy drops essentially to zero. Fracture compliances, which are linearly related to seismic crack density (see equations 2.8, 2.9), drop to values of around 0.3 which are in better agreement with laboratory values mentioned above. However, vertical velocities predicted by the model are now much higher (around 6000 m/s even if all sets are included) and thus do no longer match with sonic logs.

In order to provide more realistic models, a second population of fractures with parameters from field-based fracture measurements and modelling was used to modify the model (cases 5,6, see figure 5.15). Seismic crack density of the new fractures was also reduced by 75% to maintain reasonable fracture compliances. Bearing in mind that this is still unlikely to be a correct representation of the entire fracture network, the change of the resulting velocity field is still remarkable. Since the newly introduced fractures have a larger aspect ratio and thus comprise more porosity, pore pressure equilibration can be accomplished. As a technical note, it should be kept in mind that this model violates some of the assumptions in the underlying equation 2.9. These include that the porosity with which fractures are allowed to communicate, is originally assumed to be implemented by pores of large aspect ratios (approximately round). On the other hand Thomsen (1995) notes that similar effects should be observed when fluid flow between fractures occurs. The consequence of pore pressure equillibration is that the slow direction in the simpler case 5 is now normal to the fracture plane, as expected and shown by other authors (Thomsen, 1995; Lynn et al., 1996; Lynn, 2004). This behaviour is reflected in a marked increase in P-wave anisotropy to values of around 10% (table 5.3). The type of anisotropy is transverse isotropy with a horizontal axis of symmetry (HTI) for one open set of fractures and orthotropy if all fracture sets are included. The vertical P-wave velocities lie between 5800 m/s and 5000 m/s for cases 5 and 6, respectively. This corresponds to the upper range of velocities seen in sonic logs. Fracture compliances lie

between approximately 0.1 and 0.3 and are thus in acceptable agreement with measured values (Rasolofosaon et al., 2000). With respect to potential AVAz anomalies, one might infer that a situation corresponding to case 5 could potentially be detected if a full azimuth survey and large enough incident angles (≥30-40°) are available. The anisotropy obtained from model 6, on the other hand, shows less pronounced azimuthal variations and would require larger incident angles to be detected. At the same angle of incidence, case 5 would cause a larger anomaly than case 6, despite being much less fractured.

Cases 7 and 8 (figure 5.17) also incorporates more porosity and thus allows for pressure equilibration. However, instead of introducing more fractures, a small volume portion of vugs (5% porosity, aspect ratio 0.5) is introduced using DEM theory. Vuggy porosity is observed in the sills and may be an important contributor to porosity of the volcanic reservoirs (Witte et al. (2012); *YPF*, pers. comm.). Figure 5.13 implies that the vugs' effect on P-wave velocity is almost negligible. Thereby, we conclude that it is again the introduction of Gassmann-type pore pressure equilibration which makes the porous rock compliant. In this case, assumptions are met, because fractures communicate mostly with nearly round pores, making the result more reliable. The vertical P-wave velocity ranges between approximately 5150 m/s and 4600 for cases 7 and 8, respectively. This is in good agreement with the lower range of sonic velocities from the well logs. In case 7, one open fracture set causes HTI of 13% P-wave anisotropy between the slow and fast directions. The orthotropic behaviour in case 8 is characterised by 10-14%. As a consequence, horizontal P-wave velocities show stronger variations in case 7 compared to case 8. Due to the presence of vugs, the near-vertical P-wave velocity variations are smaller compared to the models with only fractures. This means that higher incident angles would be needed to detect anisotropic behaviour than in the models with only fractures. Qualitatively, significant azimuthal velocity variations are seen for incident angles ≥40° and ≥60-70° for case 7 and 8, respectively.

Main conclusions of this rock physics modelling are that (1) a realistic model needs to take sealing and closure of cracks due to mineral fill and subsurface pressure into account, (2) pore pressure equilibration is a key ingredient to produce strong P-wave anisotropy, if fractures are assumed to be fluid-saturated, (3) models containing exclusively vertical fractures fail to explain low velocities within sills obtained from sonic well logs. If these low velocity zones are mainly caused by intense fracturing, we propose that a significant amount of fractures has to be non-vertical. In this context, including more realistic fracture orientation distributions could give additional insight. Another geologically

justifiable explanation could be the presence of vuggy porosity, which has been observed in cores and thin sections from volcanic reservoirs in Rio Grande Valley and the Neuquén Basin (Sruoga and Rubinstein, 2007; Witte et al., 2012). Considering the porosity needed within the sills to host the significant volumes of up to 25 Million barrels per field (Senger et al., submitted), a combination of fractures and vugs may be a plausible explanation which would also fit well with geophysical models and measurements.

6.3 Integration of Datasets

In the last section of the discussion, the focus will be on the third research goal of integrating the different datasets and results. Some of the data integration has been touched upon during the previous discussion parts, and thus this section will be aimed at providing more detail on the interrelation of seismic and rock physics modelling with respect to the sills, and outlining further potential and pitfalls related to such integrated reservoir characterisation efforts.

The outcrop-based large scale seismic modelling study showed clearly that volcanic sill complexes create distinct seismic waveforms which are directly related to the complex geometrical features of the interconnected intrusive bodies. The observed waveforms observed can be described using the seismic facies scheme given by Planke et al. (2005). Figure 6.1 shows also that the modelled seismic response has direct analogues in 3D seismic data. However, depending on signal frequency, some of the details seen in the outcrops at El Manzano are masked in interference patterns. Additionally, well data indicates that seismic impedance varies strongly in both sills and host rock, and that impedance contrasts are by no means exclusively strong. Although on one hand this may complicate seismic interpretation, it also provides potential for more in-depth characterisation of the sill complex. If both interference patterns and variations of impedance contrasts can be reliably related to geological features and changes of the petrophysical properties within the intrusives, this would be a useful addition to the characterisation of this type of reservoir. While high-resolution outcrop observations as presented in figures 5.1 and 5.2 provide guidance for geometrical interpretation, rock physics models may provide the link between seismic response and petrophysical rock properties such as pore-space geometry, fracturing, and saturating fluids. The rock physics models presented in this study are by no means complete. However, by giving a range of possible rock models based on sound geological investigations, they do contribute to the understanding of P-wave velocity variations in sonic logs and P-wave anisotropy related to fracturing and

pore space geometry. This, in turn, can support both qualitative seismic interpretation of layer geometries, as well as quantitative seismic interpretation such as azimuthal AVA studies. Ultimately, the aim of seismic exploration is to link the seismic response to the underlying geology as accurately and comprehensively as possible. To accomplish this goal, integration of different geological and geophysical datasets is of major importance.

In addition to the large potential discussed above, there are certain pitfalls that must be addressed. As mentioned above, seismic modelling reveals that interference effects play an important role for the seismic response of volcanic sill complexes with many thin intrusions. When performing quantitative seismic analysis such as AVAz in such an area, and the target reflection will be a fucntion of interference with neighbouring events. Therefore, it is likely that the surrounding geology outside of the target strongly affects quantitative interpretation results. This highlights the need to assess the level of disturbance in the seismic that arises in volcanic sill complexes. Detailed 2D/3D seismic modelling can be an important component for this task. One should also bear in mind that strong variations of impedance contrasts wihtin the model may influence the applicable angle range for amplitude vs. angle investigations. The high impedance contrast endmember for seismic modelling in the study has a critical angle of around 37°, while the low contrast endmember does not even have a critical angle, and thus no limitations for AVAz studies. Additionally, rock physics modelling demonstrates that the angle range needed to detect anomalies is strongly dependent on the fracture network. If HTI-type anisotropy applies and the conditions are optimal, 30° angle of incidence can be sufficient to measure the anomaly. Orthotropic behaviour requires incident angles of at least 60-70°. As a consequence, a case comprising many fractures of different orientations could also appear as a weak anomaly, despite being favourable from a permeability standpoint. In such a situation, geological models are be needed to compliment the interpretation of AVAz anomalies. Here, it is also important to keep in mind that the velocities do not necessarily reflect the behaviour of the reflection coefficients. If the overlying layers are also azimuthally anisotropic, the situation gets even more complex. In addition, Planke et al. (2014) points out that offset-dependent interference of the top and bottom reflections of a sill is expected for thin intrusions. However, the AVAz anomalies illustrated in figure 6.2 were detected using incident angles of up to 70° (*YPF*, pers. comm.). They were drilled and very high permeability were found in and around the targeted intrusions, proving that AVAz studies can be successful despite unfavourable conditions.

Another implication of the observed interference for both seismic and rock physics modelling is that lithological variations around the intrusions should be included in the models. Magee et al. (2015) note the importance of the host rock style for seismic imaging of intrusions, however, they restrict their conclusions to the effects on image quality and qualitative seismic interpretation. In addition to that, it is likely that seismic interference will also influence the results of quantitative interpretation methods applied to intrusions. As a consequence, all lithologies in the modelled target interval should be implemented with comparable detail, as they may exhibit similar complexity. For instance, clastic rocks such as shales may show lateral thickness variations and exhibit strong velocity anisotropy due to layering and fracturing, and carbonates and evaporites may behave very similar to sills. The approach presented in this thesis is suitable for all lithologies and may therefore be used to create geological models of enormous detail. Especially in complex geological environments like the one presented in this study, such a high level of detail is require to develop a comprehensive geological and geophysical understanding.

7 Conclusions and Future Work

This thesis presents an integrated modelling study for the seismic characterisation of hydrocarbon producing sills in the Rio Grande Valley. Data from fieldwork, 3D virtual outcrop models, wells, and seismic surveys are combined to achieve three key research goals. (1) Assessment of the expression of the sills in seismic data using a seismic forward modelling study to reduce interpretation risk. (2) Investigation of the effects of fractures on elastic rock properties by means of rock physics modelling. (3) Integration of seismic and rock physics modelling with seismic data in order to link observations on different scales. The main results of the study are summarised below.

Seismic Modelling

- Workflows are established to perform digital interpretation and measurements on high resolution digital 3D models of outcrops obtained from Structure from Motion. The resulting models take details into account that would usually be considered far below the seismic resolution limit. This enables the implementation of such details in seismic modelling campaigns.

- Outcrop-based seismic modelling using an advanced 2D/3D convolution technique gives new insight regarding the resolution of seismic images in volcanic sill complexes. The interplay of intrusion thickness and geometry, seismic signal frequency and illumination strongly affects the expression of a volcanic sill complex in seismic data. The sills at El Manzano are not fully resolved and create complex interference patterns. However, characteristic waveforms arise that can be used to interpret the underlying intrusion geometries, for instance branching and steps of reflections. These waveforms show high similarity to observed seismic field data.

- The properties used for seismic modelling are based on well data and reveal a significant overlap of the values ranges for elastic impedance between the intrusions and their host rock. As a consequence, sills may cause both strong and very weak seismic amplitudes. In some cases, low-impedance intrusions may even result in weak soft kicks and produce phase changes at larger offsets.

Rock Physics Modelling

- A rock physics model for carbonates is adapted for hydrocarbon-bearing volcanic sills. The model is capable of representing various typical elements of the pore space of volcanic rocks, including vugs and fractures. The most realistic results are produced when (1) crack density obtained from outcrops is strongly reduced to account for sealing and closure of fractures at depth, and (2) when either fractures of varying shapes or vugs are included in the model.

- Regarding the outcropping sills at El Manzano, fracture analysis shows that the majority of fractures are arranged in sets of preferred orientation (approximately N-S, E-W, and horizontal). The corresponding rock physics modelling predicts that seismic velocity can drop significantly to values comparable to those from sonic log measurements. If anisotropy is considered, it reflects either HTI or orthotropy, depending on the fracture sets that are considered. The magnitude of P-wave anisotropy is expected to reach values of up to 14%. In order to detect azimuthal anisotropy from AVAz analysis, incidence angles of $> 30°$(HTI) and $> 60°$(orthotropy) are required. In fact, this indicates that subsurface areas where high permeability is caused by complex fracture networks are challenging to detect.

Data Integration and Link between the Scales

- The presented study demonstrates how integration of datasets and modelling at different scales can improve the understanding of observations from wells and seismic data. Outcrop observations and digital 3D mapping can establish a link between the geometry of the sill complex and seismic waveforms, while rock physics modelling can provide a link between petrophysical rock properties (fractures, pores, etc.) and elastic rock properties. These property variations are expressed as amplitude variations in the seismic response or velocity variations well logs.

- An integration of fieldwork, 3D outcrop models and well data can result in realistic scenarios to constrain observations from seismic fracture detection techniques (AVAz). This novel approach contributes to a better understanding of the variations seen in the related seismic attributes.

Recommendations for Future Work

The results of this study can be seen as starting points for future work to further improve our understanding of sill complexes and volcanic sill reservoirs. The following topics could complement existing knowledge in various disciplines.

- Detailed representations of host rock and contact aureoles should be included in both seismic forward modelling and rock physics modelling studies, since they comprise strong property variations and intense fracturing.
- A major factor of uncertainty in rock physics modelling is the pore space geometry, including vugs and fractures. To reduce this uncertainty, micro-scale pore space characterisation could provide additional input for the rock physics models. This may facilitate interpretation of seismic and well data and could reveal the influence of features on different scales on seismic expressions.
- The controls on the evolution of the fracture network in sills should be investigated, including the influence of tectonic stresses and cooling joints on post-emplacement fracture evolution. This could be achieved by performing numerical studies and provide insights into the conditions needed to create interconnected fracture systems in sills.
- A feasibility study for including shear wave logs and multi-component seismic surveys could be highly beneficial, because fractures the affect v_p/v_s ratio. Although this was not part of the discussion, the results for S-wave anisotropy indicate strong effects, even at small incidence angles. This may produce detectable anomalies. In fact, the existing rock physics models could also be used to link results of such studies to the microstructure of the rock, as shown by Xu and Payne (2009).
- Conducting a seismic survey on top of the El Manzano outcrop is highly recommended. Such a study is feasible and could provide a showcase for linking outcrop and seismics, measuring anisotropy parameters, and testing rock physics models.

This list of proposed studies is by no means claimed to be complete. Volcanic rocks and associated reservoirs comprise tremendous complexity, and therefore require ongoing attention from the geoscientific research community.

References

Anell, I., I. Lecomte, A. Braathen, and S. J. Buckley (2016). "Synthetic seismic illumination of small-scale growth faults, paralic deposits and low-angle clinoforms: A case study of the Triassic successions on Edgeøya, NW Barents Shelf". *Marine and Petroleum Geology* 77, pp. 625–639. ISSN: 02648172. DOI: 10.1016/j.marpetgeo.2016.07.005.

Badessich, M. F., D. E. Hryb, M. Suarez, L. Mosse, N. Palermo, S. Pichon, and L. Reynolds (2016). "Vaca Muerta Shale—Taming a Giant". *Oilfield Review* 28.1.

Balgord, E. A. and B. Carrapa (2016). "Basin evolution of Upper Cretaceous–Lower Cenozoic strata in the Malargüe fold-and-thrust belt: northern Neuquén Basin, Argentina". *Basin Research* 28.2, pp. 183–206.

Barton, N. (2007). *Rock quality, seismic velocity, attenuation and anisotropy*. CRC press, pp. 411–504.

Berge, P. A., G. J. Fryer, and R. H. Wilkens (1992). "Velocity-porosity relationships in the upper oceanic crust: Theoretical considerations". *Journal of Geophysical Research* 97.B11, p. 15239. ISSN: 0148-0227. DOI: 10.1029/92JB01464.

Botter, C. D. (2016). "Seismic Imaging of Fault Zones: A synthetic workflow to study the impact of faults on seismic images".

Budiansky, B. and R. J. O'connell (1976). "Elastic moduli of a cracked solid". *International Journal of Solids and Structures* 12.2, pp. 81–97. ISSN: 00207683. DOI: 10.1016/0020-7683(76)90044-5.

Casini, G., D. W. Hunt, E. Monsen, and A. Bounaim (2016). "Fracture characterization and modeling from virtual outcrops". *AAPG Bulletin* 100.01, pp. 41–61. ISSN: 0149-1423. DOI: 10.1306/09141514228.

Eide, C. H., N. Schofield, D. A. Jerram, and J. A. Howell (2016). "Basin-scale architecture of deeply emplaced sill complexes: Jameson Land, East Greenland". *Journal of the Geological Society*, jgs2016–018.

Enge, H. D, S. J. Buckley, A. Rotevatn, and J. A. Howell (2007). "From outcrop to reservoir simulation model: Workflow and procedures". *Geosphere* 3.6, pp. 469–490.

Eshelby, J. D. (1957). "The determination of the elastic field of an ellipsoidal inclusion, and related problems". *Proceedings of the Royal Society of London A: Mathematical, Physical and Engineering Sciences*. Vol. 241. 1226. The Royal Society, pp. 376–396.

Far, M. E., C. M. Sayers, L. Thomsen, D. Han, and J. P. Castagna (2013). "Seismic characterization of naturally fractured reservoirs using amplitude versus offset and azmuth analysis". *Geophysical Prospecting* 61.2, pp. 427–447. ISSN: 00168025. DOI: 10.1111/1365-2478.12011.

Farooqui, M. Y., H. Hou, G. Li, N. Machin, T. Neville, A. Pal, C. Shrivastva, Y. Wang, F. Yang, C. Yin, et al. (2009). "Evaluating volcanic reservoirs". *Oilfield Review* 21.1, pp. 36–47.

Fernandez-Concheso, J. E. (2015). "Characterizing an unconventional reservoir with conventional seismic data. A case study using seismic inversion for the Vaca Muerta formation, Neuquen Basin, Argentina". PhD thesis. Colorado: Colorado School of Mines. URL: https://dspace.library.colostate.edu/bitstream/handle/11124/170010/FernandezConcheso_mines_0052N_10912.pdf?sequence=1.

Grechka, Vladimir and Mark Kachanov (2006). "Effective elasticity of fractured rocks: A snapshot of the work in progress". *Geophysics* 71.6, W45–W58. ISSN: 0016-8033. DOI: 10.1190/1.2360212.

Howell, J. A., E. Schwarz, L. A. Spalletti, and G. D. Veiga (2005). "The Neuquén basin: an overview". *Geological Society, London, Special Publications* 252.1, pp. 1–14. ISSN: 0305-8719.

Hsu, Chaur-Jian and Michael Schoenberg (1993). "Elastic waves through a simulated fractured medium". *Geophysics* 58.7, pp. 964–977.

Hudson, J. A. (1980). "Overall properties of a cracked solid". *Mathematical Proceedings of the Cambridge Philosophical Society* 88.02, p. 371. ISSN: 0305-0041. DOI: 10.1017/S0305004100057674.

Kay, S. M., W. M. Burns, P. Copeland, and O. Mancilla (2006). "Upper Cretaceous to Holocene magmatism and evidence for transient Miocene shallowing of the Andean subduction zone under the northern Neuquén Basin". *Geological Society of America Special Papers* 407, pp. 19–60.

Klarner, S. and O. Klarner (2012). *Identification of paleo-volcanic rocks on seismic data*. URL: http://cdn.intechweb.org/pdfs/25987.pdf.

Landrø, M. (2010). "4D Seismic". *Petroleum Geoscience*. Ed. by Knut Bjorlykke. Berlin and Heidelberg: Springer Berlin Heidelberg, pp. 427–444. ISBN: 978-3-642-02331-6. DOI: 10.1007/978-3-642-02332-3_19.

Leanza, H. (2009). "Las principales discordancias del Mesozoico de la Cuenca Neuquina según observaciones de superficie". *Revista del Museo Argentino de Ciencias Naturales nueva serie* 11.2, pp. 145–184.

Lecomte, I. (2008). "Resolution and illumination analyses in PSDM: A ray-based approach". *The Leading Edge* 27.5, pp. 650–663. ISSN: 1070-485X. DOI: 10.1190/1.2919584.

Lecomte, I., H. Gjøystdal, Å. Drottning, et al. (2003). "Simulated Prestack Local Imaging: a robust and efficient interpretation tool to control illumination, resolution, and time-lapse properties of reservoirs." *2003 SEG Annual Meeting*. Society of Exploration Geophysicists.

Lecomte, I., P. Lavadera, I. Anell, S. J. Buckley, D. W. Schmid, and M. Heeremans (2015). "Ray-based seismic modeling of geologic models: Understanding and analyzing seismic images efficiently". *Interpretation* 3.4, SAC71–SAC89. ISSN: 2324-8858. DOI: 10.1190/INT-2015-0061.1.

Lecomte, I., P. Lavadera, C. Botter, S.J. Buckley, and S Kjoberg (2016). "2 (3) D convolution modelling of complex geological targets - beyond 1D convolution". *First Break* 34.5, pp. 99–107.

LIME (2016). *Lidar Interpretation and Manipulation Environment*. Bergen and Norway. URL: http://virtualoutcrop.com/lime/download.

Lynn, H. B. (2004). "The Winds of Change: Anisotropic Rocks – Their Preferred Direction of Fluid Flow and Their Associated Seismic Signatures". *The Leading Edge* 23.12, pp. 1258–1268. ISSN: 1070-485X. DOI: 10.1190/leedff.23.1258_1.

Lynn, H. B., K. M. Simon, and C. R. Bates (1996). "Correlation between P -wave AVOA and S -wave traveltime anisotropy in a naturally fractured gas reservoir". *The Leading Edge* 15.8, pp. 931–935. ISSN: 1070-485X. DOI: 10.1190/1.1437394.

Magee, C., C. A.-L. Jackson, and N. Schofield (2014). "Diachronous sub-volcanic intrusion along deep-water margins: insights from the Irish Rockall Basin". *Basin Research* 26.1, pp. 85–105. ISSN: 0950091X. DOI: 10.1111/bre.12044.

Magee, C., S. M. Maharaj, T. Wrona, and C. A.-L. Jackson (2015). "Controls on the expression of igneous intrusions in seismic reflection data". *Geosphere* 11.4, pp. 1024–1041. ISSN: 1553-040X. DOI: 10.1130/GES01150.1.

Manceda, R. and D. Figueroa (1995). "Inversion of the Mesozoic Neuquén rift in the Malargüe fold and thrust belt, Mendoza, Argentina".

Mavko, G., T. Mukerji, and J. Dvorkin (2009). *The rock physics handbook: Tools for seismic analysis in porous media*. 2nd ed. Cambridge: Cambridge University Press. ISBN: 978-0-521-86136-6.

Planke, S., T. Rasmussen, S. S. Rey, and R. Myklebust (2005). "Seismic characteristics and distribution of volcanic intrusions and hydrothermal vent complexes in the Vøring and Møre basins". *Petroleum Geology: North-West Europe and Global Perspectives – Proceedings of the 6th Petroleum Geology Conference*. Geological Society of London, pp. 833–844. ISBN: 1-86239-164-5. DOI: 10.1144/0060833.

Planke, S., H. Svensen, R. Myklebust, S. Bannister, B. Manton, and L. Lorenz (2014). "Geophysics and Remote Sensing". Advances in Volcanology. Berlin and Heidelberg: Springer Berlin Heidelberg. DOI: 10.1007/11157_2014_6.

Polteau, S., A. Mazzini, O. Galland, S. Planke, and A. Malthe-Sørenssen (2008). "Saucer-shaped intrusions: Occurrences, emplacement and implications". *Earth and Planetary Science Letters* 266.1-2, pp. 195–204. ISSN: 0012821X. DOI: 10.1016/j.epsl.2007.11.015.

Rasolofosaon, P. N. J., W. Rabbel, S. Siegesmund, and A. Vollbrecht (2000). "Characterization of crack distribution: fabric analysis versus ultrasonic inversion". *Geophysical Journal International* 141.2, pp. 413–424. ISSN: 0956540X. DOI: 10.1046/j.1365-246x.2000.00093.x.

Rodriguez Monreal, F., H. J. Villar, R. Baudino, D. Delpino, and S. Zencich (2009). "Modeling an atypical petroleum system: A case study of hydrocarbon generation, migration and accumulation related to igneous intrusions in the Neuquen Basin, Argentina". *Marine and Petroleum Geology* 26.4, pp. 590–605. ISSN: 02648172. DOI: 10.1016/j.marpetgeo.2009.01.005.

Rohrman, M. (2007). "Prospectivity of volcanic basins: Trap delineation and acreage de-risking". *AAPG bulletin* 91.6, pp. 915–939.

Rüger, A. and I. Tsvankin (1997). "Using AVO for fracture detection: Analytic basis and practical solutions". *The Leading Edge* 16.10, pp. 1429–1434. ISSN: 1070-485X. DOI: 10.1190/1.1437466.

Saunders, G. (2014). "The development and application of a workflow for photogrammetric analysis of landslides". PhD thesis. Oslo: University of Oslo. URL: https://www.duo.uio.no/handle/10852/42338.

Sayers, C. and S. Chopra (2009). "Introduction to this special section—Rock physics". *The Leading Edge* 28.1, pp. 15–16. ISSN: 1070-485X. DOI: 10.1190/1.3064140.

Schoenberg, M. and J. Douma (1988). "Elastic wave propagation in media with parallel fractures and aligned cracks". *Geophysical Prospecting* 36.6, pp. 571–590. ISSN: 0016-8025. DOI: 10.1111/j.1365-2478.1988.tb02181.x.

Schofield, N., L. Heaton, S. P. Holford, S. G. Archer, C. A. L. Jackson, and D. W. Jolley (2012). "Seismic imaging of 'broken bridges': linking seismic to outcrop-scale

investigations of intrusive magma lobes". *Journal of the Geological Society* 169.4, pp. 421–426. ISSN: 0016-7649. DOI: 10.1144/0016-76492011-150.

Schofield, N., S. Holford, J. Millett, D. Brown, D. Jolley, S. Passey, D. Muirhead, C. Grove, C. Magee, J. Murray, M. Hole, C. Jackson, and C. Stevenson (2015). "Regional Magma Plumbing and emplacement mechanisms of the Faroe-Shetland Sill Complex: Implications for magma transport and petroleum systems within sedimentary basins". *Basin Research*, n/a. ISSN: 0950091X. DOI: 10.1111/bre.12164.

Senger, K., J. Tveranger, K. Ogata, A. Braathen, and S. Olaussen (2013). "Reservoir characterization and modelling of a naturally fractured siliciclastic CO 2 sequestration site". *Svalbard, Arctic Norway* 2013, p. 2.

Senger, K., S. J. Buckley, L. Chevallier, Å. Fagereng, O. Galland, T. H. Kurz, K. Ogata, S. Planke, and J. Tveranger (2015). "Fracturing of doleritic intrusions and associated contact zones: Implications for fluid flow in volcanic basins". *Journal of African Earth Sciences* 102, pp. 70–85.

Senger, K., J. Millett, Planke S., K. Ogata, C. Eide, M. Festøy, O. Galland, and D. Jerram (submitted). "Effects of igneous intrusions on the petroleum system: a review".

Skogly, O.P. (1998). "Seismic characterization and emplacement of intrusives in the Vøring Basin". *Cand Scient thesis, Department of Geology, University of Oslo*.

Sruoga, P. and N. Rubinstein (2007). "Processes controlling porosity and permeability in volcanic reservoirs from the Austral and Neuquén basins, Argentina". *AAPG Bulletin* 91.1, pp. 115–129. ISSN: 0149-1423. DOI: 10.1306/08290605173.

Thomsen, L. (1986). "Weak elastic anisotropy". *Geophysics* 51.10, pp. 1954–1966. ISSN: 0016-8033. DOI: 10.1190/1.1442051.

– (1995). "Elastic anisotropy due to aligned cracks in porous rock1". *Geophysical Prospecting* 43.6, pp. 805–829. ISSN: 0016-8025. DOI: 10.1111/j.1365-2478.1995.tb00282.x.

Tsvankin, I. (1997). "Anisotropic parameters and P –wave velocity for orthorhombic media". *Geophysics* 62.4, pp. 1292–1309. ISSN: 0016-8033. DOI: 10.1190/1.1444231.

Tsvankin, I., J. Gaiser, V. Grechka, van der Baan, M., and L. Thomsen (2010). "Seismic anisotropy in exploration and reservoir characterization: An overview". *Geophysics* 75.5, 75A15–75A29. ISSN: 0016-8033. DOI: 10.1190/1.3481775.

Westoby, M. J., J. Brasington, N. F. Glasser, M. J. Hambrey, and J. M. Reynolds (2012). "'Structure-from-Motion' photogrammetry: A low-cost, effective tool for geoscience applications". *Geomorphology* 179, pp. 300–314. ISSN: 0169555X. DOI: 10.1016/j.geomorph.2012.08.021.

Witte, J., M. Bonora, C. Carbone, and O. Oncken (2012). "Fracture evolution in oil-producing sills of the Rio Grande Valley, northern Neuquén Basin, Argentina". *AAPG Bulletin* 96.7, pp. 1253–1277. ISSN: 0149-1423. DOI: 10.1306/10181110152.

Xu, S. and M. A. Payne (2009). "Modeling elastic properties in carbonate rocks". *The Leading Edge* 28.1, pp. 66–74. ISSN: 1070-485X. DOI: 10.1190/1.3064148.

Zeeb, C., E. Gomez-Rivas, P. D. Bons, and P. Blum (2013). "Evaluation of sampling methods for fracture network characterization using outcrops". *AAPG Bulletin* 97.9, pp. 1545–1566. ISSN: 0149-1423. DOI: 10.1306/02131312042.

A Appendix

A.1 Illustration of Fieldwork activities

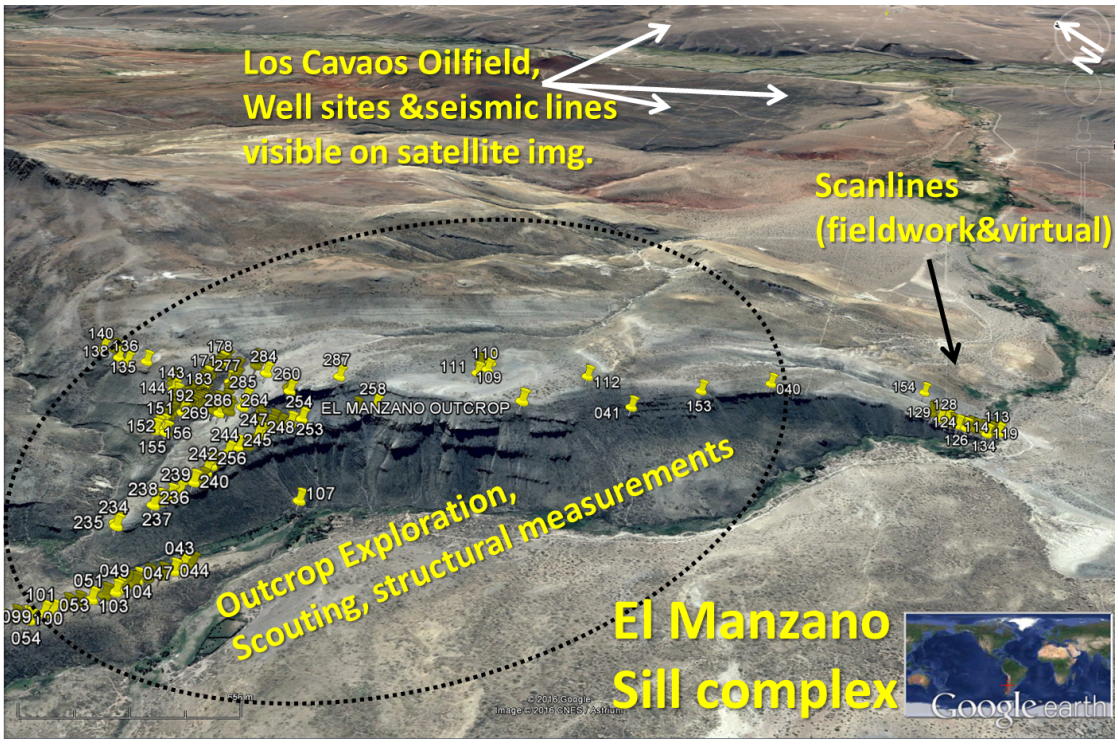

Figure A.1: Illustration of fieldwork activities at the El Manzano outcrop Rio Grande Valley. Flags indicate GPS locations of field notes or measurements.

A.2 Scanline Data for Scanlines from Fieldwork

ID	Location	Scanline type	Scanline orientation (bearing)	Length (m)	Number of fractures	Fracture intensity F	Average spacing S	Lithology	Formation
2	El Manzano S, lower Sill	linear	160	6	90	15	0.0666667	Andesite	VacaMuerta
3	El Manzano S, lower Sill	Linear		3.2	35	10.9375	0.0914286	Andesite	VacaMuerta
4	El Manzano S, lower Sill	linear		1.46	25	17.12329	0.0584	Andesite	VacaMuerta
5	El Manzano S, lower Sill	linear		3.2	72	22.5	0.0444444	Andesite	VacaMuerta
8	El Manzano S, upper Sill	linear	340	5	54	10.8	0.0925926	Andesite	VacaMuerta
9	El Manzano S, upper Sill	linear	320	5	49	9.8	0.1020408	Andesite	VacaMuerta

Scanlines taken by Juan Spacapan, Federico Gonzales, Ole Rabbel, Karen Mair

Figure A.2: Summary of field-based scanlines.

A.3 Scanline Data Summary for Virtual Scanlines

lower sill

Scanline	length(m)	N fracs	Sf (avg. spacing in m)	1/Sf (frequency in 1/m)	Comment	Level of erosion (qualitative)
l1	10.75	18	0.60	1.67	next to big vein	medium
l2	22.6	47	0.48	2.08	next to big vein	low
l3	17.7	45	0.39	2.54		medium
l4	15	28	0.54	1.87		medium
l5	14.5	25	0.58	1.72		low
l6	11.9	20	0.60	1.68	next to big vein	low-medium
l7	15.7	28	0.56	1.78	next to big vein	low
l8	15.7	23	0.68	1.46		low-medium
AVG	**15.48**	**29.25**	**0.55**	**1.85**		
STD	**3.39**	**10.22**	**0.08**	**0.31**		
m1	13.6	30	0.45	2.21	next to big vein	low
m2	17.7	21	0.84	1.19	next to big vein	low-medium
m3	10.7	17	0.63	1.59	next to big vein	medium
m4	21.4	39	0.55	1.82	next to big vein	low
m5	13.3	18	0.74	1.35		medium
m6	8.5	15	0.57	1.76		medium
m7	15.8	24	0.66	1.52		low-medium
m8	14.4	24	0.60	1.67		low-medium
m9	14.5	19	0.76	1.31	next to big vein	low-medium
m10	13.5	20	0.68	1.48	next to big vein	low-medium
m11	18.2	20	0.91	1.10		low
AVG	**14.69**	**22.45**	**0.65**	**1.59**		
STD	**3.39**	**6.51**	**0.13**	**0.30**		
u1	16.8	28	0.60	1.67	next to big vein	medium
u2	9	10	0.90	1.11	next to big vein	medium-high
u3	13.9	19	0.73	1.37	next to big vein	low-medium
u4	15.2	15	1.01	0.99		low-medium
u5	13.6	16	0.85	1.18		medium
u6	14.7	21	0.70	1.43		medium
u7	14.6	15	0.97	1.03		low-medium
u8	15.2	16	0.95	1.05	next to big vein	medium-high
u9	13.2	18	0.73	1.36	next to big vein	medium
u10	13.8	11	1.25	0.80		low
AVG	**14**	**16.9**	**0.87**	**1.20**		
STD	**1.93**	**4.87**	**0.18**	**0.24**		
v1	11.3	5	2.26	0.44		
v2	8.4	5	1.68	0.60		
v3	9.4	5	1.88	0.53		
v4	10.7	7	1.53	0.65		
v5	11.3	6	1.88	0.53		
v6	9.1	2	4.55	0.22		
v7	11.1	5	2.22	0.45		
v8	12.3	6	2.05	0.49		
AVG	**10.45**	**5.13**	**2.26**	**0.49**		
STD	**3.08**	**3.75**	**1.07**	**0.26**		

Figure A.3: Fracture frequency measurements from virtual scanlines in the lower Sill

upper sill

Scanline	length	N fracs	average spacing	average frequency	Comment	Level of erosion (qualitative)
l1	13.00	28	0.46	2.15		low
l2	14.9	17	0.88	1.14	next to big vein	high
l3	14.1	21	0.67	1.49	next to big vein	medium-high
l4	10	9	1.11	0.90		medium
l5	8.7	16	0.54	1.84	next to big vein	medium
l6	8.8	19	0.46	2.16	next to big vein	high
l7	14.2	24	0.59	1.69		medium
l8	8.7	17	0.51	1.95		high
l9	19.4	22	0.88	1.13	next to big vein	high
l10	18.4	15	1.23	0.82	next to big vein	medium-high
l11	17.4	24	0.73	1.38		medium
l12	9.8	14	0.70	1.43	next to big vein	medium
l13	15.5	29	0.53	1.87		medium-high
l14	15.8	28	0.56	1.77		medium-high
AVG	**13.48**	**20.21**	**0.73**	**1.53**		
STD	**3.59**	**5.75**	**0.23**	**0.42**		
m1	12.9	16	0.81	1.24		low-medium
m2	11.2	11	1.02	0.98	next to big vein	high
m3	21.2	24	0.88	1.13	next to big vein	medium
m4	13.3	14	0.95	1.05	next to big vein	high
m5	13.9	8	1.74	0.58		high
m6	20.8	11	1.89	0.53		high
m7	21.5	10	2.15	0.47		medium-high
m8	15	13	1.15	0.87	next to big vein	high
m9	16.1	18	0.89	1.12	next to big vein	high
m10	12.6	23	0.55	1.83		high
m11	11.2	13	0.86	1.16		high
AVG	**15.43**	**14.64**	**1.28**	**0.88**		
STD	**3.77**	**4.94**	**0.49**	**0.37**		
u1	13.3	14	0.95	1.05		medium
u2	11.6	10	1.16	0.86	next to big vein	high
u3	9.5	7	1.36	0.74		high
u4	13.5	11	1.23	0.81		high
u5	11	6	1.83	0.55		high
u6	18.5	16	1.16	0.86		medium
u7	18.5	12	1.54	0.65		high
AVG	**13.7**	**10.86**	**1.32**	**0.79**		
STD	**3.29**	**3.31**	**0.27**	**0.15**		
v1	15.6	3	5.20	0.19		
v2	13.8	6	2.30	0.43		
v3	14.9	2	7.45	0.13		
v4	14.3	3	4.77	0.21		
v5	14.7	2	7.35	0.14		
v6	14.5	2	7.25	0.14		
AVG	**14.63**	**3**	**5.72**	**0.21**		
STD	**0.55**	**1.41**	**1.86**	**0.11**		

Figure A.4: Fracture frequency measurements from virtual scanlines in the upper Sill